

**FAST LOCAL APPROXIMATION TO GLOBAL
ILLUMINATION**

by

Christopher R. Wyman

A dissertation submitted to the faculty of
The University of Utah
in partial fulfillment of the requirements for the degree of

Doctor of Philosophy

in

Computer Science

School of Computing

The University of Utah

August 2004

Copyright © Christopher R. Wyman 2004

All Rights Reserved

THE UNIVERSITY OF UTAH GRADUATE SCHOOL

SUPERVISORY COMMITTEE APPROVAL

of a dissertation submitted by

Christopher R. Wyman

This dissertation has been read by each member of the following supervisory committee and by majority vote has been found to be satisfactory.

Chair: Charles Hansen

Elaine Cohen

Victoria Interrante

Steven Parker

Peter Shirley

THE UNIVERSITY OF UTAH GRADUATE SCHOOL

FINAL READING APPROVAL

To the Graduate Council of the University of Utah:

I have read the dissertation of Christopher R. Wyman in its final form and have found that (1) its format, citations, and bibliographic style are consistent and acceptable; (2) its illustrative materials including figures, tables, and charts are in place; and (3) the final manuscript is satisfactory to the Supervisory Committee and is ready for submission to The Graduate School.

Date

Charles Hansen
Chair, Supervisory Committee

Approved for the Major Department

Christopher R. Johnson
Director

Approved for the Graduate Council

David S. Chapman
Dean of The Graduate School

ABSTRACT

Interactive global illumination remains an elusive goal in rendering, as energy from every portion of the scene contributes to the final image. Integrating over a complex scene, with a polygon count in the millions or more, proves difficult even for static techniques. Interacting with such complex environments while maintaining high quality rendering generally requires recomputing the paths of countless photons using a small number of CPUs. This dissertation examines a simplified approach to interactive global illumination. Observing that local illumination computations can be performed interactively even on fairly simple graphics accelerators, a reduction of global illumination problems to local problems would allow interactive rendering. A number of techniques are suggested that simplify global illumination to specific global illumination effects (e.g., diffuse interreflection, soft shadows, and caustics), which can individually be sampled at a local level. Rendering these simplified global illumination effects reduces to a few lookups, which can easily be done at interactive rates. While some tradeoffs exist between rendering speed, rendering quality, and memory consumption, these techniques show that approximating global illumination locally allows interactivity while still maintaining significant realism.

CONTENTS

ABSTRACT	iv
LIST OF FIGURES	vii
LIST OF TABLES	x
ACKNOWLEDGMENTS	xi
CHAPTERS	
1. INTRODUCTION	1
1.1 Local Illumination	2
1.2 Global Illumination	5
1.2.1 Radiometry	5
1.2.2 Reflectance of Light	7
1.2.3 The Rendering Equation	8
1.3 Motivation for Global Illumination	8
1.4 Overview of this Work	13
2. PREVIOUS WORK	15
2.1 Radiosity Approaches	16
2.2 Ray-based Approaches	17
2.3 Hybrid Radiosity-Raytraced Approaches	20
2.3.1 Interactive Hybrid Approaches	21
2.4 Soft Shadow Techniques	22
2.5 Caustic Techniques	26
2.6 Other Interactive Global Illumination Approaches	27
3. INTERACTIVE SOFT SHADOWS USING <i>PENUMBRA MAPS</i> ..	31
3.1 Shadow Plateaus	32
3.2 Penumbra Maps	34
3.3 Implementation	39
3.3.1 Discussion of Limitations	40
3.4 Results	41
4. INTERACTIVE RENDERING OF CAUSTICS	45
4.1 Caustics	47
4.1.1 Caustic Behavior	47
4.1.2 Simplifying the Problem	48
4.2 Caustic Sampling	49
4.2.1 Sampling the Light	49
4.2.2 Sampling Space	50

4.2.3	Data Representation	51
4.3	Caustic Rendering	53
4.3.1	Rendering Algorithm	53
4.3.2	Issues Rendering Caustic Data	54
4.4	Results	57
4.5	Discussion	61
5.	INTERACTIVE RENDERING OF ISOSURFACES WITH GLOBAL ILLUMINATION	63
5.1	Background	65
5.2	Overview	66
5.3	Algorithm	70
5.3.1	Illumination Computation	70
5.3.2	Interactive Rendering	73
5.4	Results	74
6.	CONCLUSIONS AND FUTURE WORK	85
 APPENDICES		
A.	SHADER CODE FOR PENUMBRA MAPS	88
B.	SPHERICAL HARMONICS	93
REFERENCES	110

LIST OF FIGURES

1.1	Examples of local illumination models	3
1.2	The Phong illumination model uses four vectors to determine lighting for each point	4
1.3	Radiance is the energy per unit area per unit time per unit solid angle $d\vec{\omega}$	6
1.4	Renderings using local, direct, and global illumination	10
1.5	An object's shadow affects the perception of object location	11
1.6	Refraction of light through the cup and water introduces apparent bends, discontinuities, and other artifacts to a typical wooden pencil	12
1.7	Common caustics from everyday life	13
3.1	The shadow umbra includes regions where the light is completely occluded, and the penumbra occurs in regions where objects only partially occlude the light	32
3.2	Penumbra maps in a scene with multiple lights	33
3.3	Approximate soft shadows using shadow plateaus	34
3.4	Rendering using penumbra maps	36
3.5	Explanation of penumbral sheets and cones	37
3.6	Computing per-fragment intensity from cone or sheet geometry	37
3.7	Pseudocode for penumbra map fragment program	38
3.8	These pathtraced images show three different types of interactions between overlapping penumbra	40
3.9	Penumbra map results for the Stanford bunny	42
3.10	Penumbra map results for the dragon model	43
4.1	A scene with caustics from a glass bunny	46
4.2	The eight dimensions of a caustic	48
4.3	Popping between adjacent light samples	50
4.4	Sampling space on either a uniform grid or a set of concentric shells	51
4.5	Sharper caustics come at the expense of denser sampling	52
4.6	\hat{L} intersects the spherical triangle formed by \hat{L}_i , \hat{L}_j , and \hat{L}_k	55
4.7	Ghosting happens when the caustic changes significantly between neighboring light samples \hat{L}_i , \hat{L}_j , and \hat{L}_k	55

4.8	Alternative approach to caustic lookups	56
4.9	Caustic rendering techniques on a metal ring and glass cube	58
4.10	Caustic rendering techniques on a glass prism	59
4.11	Casting caustics on complex objects	60
4.12	The caustic of a prism in St. Peter’s cathedral using fifth order spherical harmonics	60
5.1	Comparison of globally illuminated and Phong shaded isosurfaces	64
5.2	Computing the irradiance at point \mathbf{p} involves sending a shadow ray and multiple reflection rays	67
5.3	The global illumination at each texel t is computed using standard techniques based on the isosurface $I(\rho(\mathbf{x}_t))$ through the sample	68
5.4	The Visible Female’s skull globally illuminated using the new technique . . .	69
5.5	Pseudocode to compute irradiance at samples in the illumination lattice. . .	71
5.6	An isosurface from the Visible Female’s head extracted using analytical intersection of the trilinear surface	72
5.7	Approaches to interpolating between illumination samples	74
5.8	The engine block illuminated by the Grace cathedral lightprobe	76
5.9	An enlarged portion of the Richtmyer-Meshkov dataset shown in Figure 5.11	78
5.10	A Richtmyer-Meshkov instability simulation under various illumination . . .	79
5.11	Another view of a Richtmyer-Meshkov instability simulation	80
5.12	Comparison with vicinity shading	81
5.13	The new technique versus Monte Carlo pathtracing with 10000 samples per pixel	82
5.14	Effect of different illumination volume resolutions	83
A.1	Vertex program for rendering a penumbra map.	88
A.2	Fragment program for rendering a penumbra map.	89
A.3	Vertex program for rendering using a penumbra map.	91
A.4	Fragment program for rendering using a penumbra map.	92
B.1	Header file describing the SHRotationMatrix C++ class.	104
B.2	Function definition for SHRotationMatrix::u_i_st().	105
B.3	Function definition for SHRotationMatrix::v_i_st().	105
B.4	Function definition for SHRotationMatrix::w_i_st().	105
B.5	Function definition for SHRotationMatrix::U_i_st().	105
B.6	Function definition for SHRotationMatrix::V_i_st().	106
B.7	Function definition for SHRotationMatrix::W_i_st().	106

B.8	Function definition for SHRotationMatrix::P_r_i_st().	106
B.9	Function definition for SHRotationMatrix::R().	106
B.10	Function definition for SHRotationMatrix::M().	107
B.11	Function definition for SHRotationMatrix::matIndex().	107
B.12	Definition of constructor SHRotationMatrix::SHRotationMatrix().	107
B.13	Function definition for SHRotationMatrix::computeMatrix().	108
B.14	Function definition for SHRotationMatrix::applyMatrix().	109

LIST OF TABLES

1.1	Units of radiometric properties	7
3.1	Framerate comparison using shadow and penumbra maps	41
4.1	Caustic rendering and precomputation times	57
5.1	Illumination computation timings for images from Figure 5.8	75
5.2	Comparison of framerates and memory consumption for Figure 5.8	77
B.1	Definitions of numerical coefficients $u_{s,t}^i$, $v_{s,t}^i$, and $w_{s,t}^i$	102
B.2	Definitions of the functions $U_{s,t}^i$, $V_{s,t}^i$, and $W_{s,t}^i$	102
B.3	Definitions of the function $rP_{s,t}^i$	102

ACKNOWLEDGMENTS

I would like to thank everyone who helped and supported me during my graduate work. In particular, my advisor Chuck Hansen deserves thanks for funding and enabling my research as well as his helpful comments and discussion along the way. Pete Shirley also provided immense help and guidance during my tenure in Utah; I would particularly like to thank him for sharing his vast rendering knowledge and keeping the lab amused with his unique sense of humor.

I would also like to thank my other committee members, Steve Parker, Elaine Cohen, and Vicki Interrante, for interesting discussions, scheduling flexibility, and useful feedback on my work.

My colleagues in the Graphics and SCI labs helped keep me sane during long nights in the lab, provided insightful feedback on my work, and entertained me outside the lab. In no particular order, I would like to thank Shaun Ramsey, Dave DeMarle, Charles Schmidt, Rahul Jain, Aaron Lefohn, Milan Ikits, Joe Kniss, Mike Stark, Bill Martin, Erik Reinhard, Simon Premoze, Helen Hu, Rose Mills, Margarita Bratkova, Justin Polchlopek, Kristi Potter, Bruce Gooch, Amy Gooch, Dylan Lacewell, Dave Edwards, and Joel Daniels.

Outside of the department, I met many people in Utah who kept me from becoming too focused on work. Particularly, all the people I met through various band organizations in the Music Department helped keep my musical abilities alive. I would also like to thank them for all the opportunities they afforded me, including the chance to participate in the 2002 Winter Olympic Games.

Finally, I would like to acknowledge my family, and particularly my parents, for the support they have given throughout my educational career. They had unwavering confidence in my abilities, even when I had doubts.

This work was supported by the National Science Foundation under Grants 9977218 and 9978099 as well as the College of Engineering's Wayne Brown Fellowship. Additionally, portions of Chapter 3, including figures and tables, are reprinted with permission from my 2003 paper [152] from the Eurographics Symposium on Rendering, copyright the Eurographics Association for Computer Graphics.

CHAPTER 1

INTRODUCTION

Computer graphics involves creating, or *rendering*, images of synthetic environments. Often the goal is to render images of these environments as realistically as possible. Achieving images indistinguishable from photographs, called *photorealistic* images, requires accurate physical models of light transport, complex materials, and geometry. Although object geometry is relatively easy to simulate given the right primitives, modeling light transport and complex material properties are areas of active research. This dissertation examines ways to simplify complex illumination so interactive applications can benefit from improved realism.

In part due to the complex illumination present in real world environments, photorealistic renderings of environments remain difficult to generate using computer graphics techniques. This difficulty arises because illumination requires global information. Light bounces off virtually all objects, so computing the color at some point in a scene involves integrating over all the incident illumination. Obviously, such an operation can prove extremely time consuming. Even after 30 years of research, code optimization, and dramatically improved computer processors, such illumination computations still prove expensive. Because of this expense, realistic renderings are usually generated by batch processes and interactive applications continue to use lower quality lighting approximations.

Over the past 30 years, assorted models have been proposed for simulating illumination for computer graphics. Initially, objects were drawn in wire-frame [4, 80]. Later models like flat, Gouraud [40], and Phong [102] shading use local information at every point on the object to determine illumination. These models provide only *local illumination*. Raytracing techniques [149] and rasterization techniques like shadow mapping [25] extended illumination models to allow direct illumination, which includes shadows when objects occlude the light. Illumination arriving directly from a light, without bouncing off intermediate objects, is called *direct illumination*.

More recent illumination models approximate the rendering equation [67], allowing inclusion of *indirect illumination*—light reflected off other objects in the environment. The *rendering equation* models the physical transport of light through a scene, and was borrowed from the study of radiative heat transfer. Because solutions to the rendering equation require global knowledge of the scene, such as geometry and material properties, the resulting illumination is called *global illumination*.

Often the terms local and direct illumination are used interchangeably. However, local lighting relies on local information such as position, surface normal, viewing direction, and direction to the light. Hence, purely local models cannot achieve shadowing effects, which require knowledge about global visibility. Direct illumination, on the other hand, includes all the light directly hitting a surface. In cases where the light is hidden by an occluder, a surface will not be illuminated. Similarly, global and indirect illumination are often interchanged. Indirect illumination is a subset of global illumination, but the shadowing effects of direct illumination models also require global visibility information.

Computing local lighting is easy because it requires only local information. Thus, interactive applications such as simulators, architectural walkthroughs, computer-aided design programs, and computer games usually rely on local illumination models. While current techniques are vastly better than the interactive methods of a decade ago, due to the improved computation power available on graphics hardware, most interactive techniques still lack complex global lighting effects seen in the real world. Thus, only applications that can afford slow computations, such as special-effects and computer generated movies, enjoy the fruits of decades of global illumination research.

1.1 Local Illumination

Early computer graphics researchers focused their efforts on the most important problems of the time, namely techniques to render geometry quickly. Generally, they used simple empirical illumination models such as the flat, Gouraud, and Phong shading techniques shown in Figure 1.1. These techniques are composed of three parts: an ambient term which approximates indirect illumination, a diffuse term that approximates matte materials, and a specular term which adds a specular, or glossy, appearance. Because these local models ignore indirect illumination, the user-defined ambient term helps brighten surfaces not directly illuminated. This gives renderings a more realistic appearance.

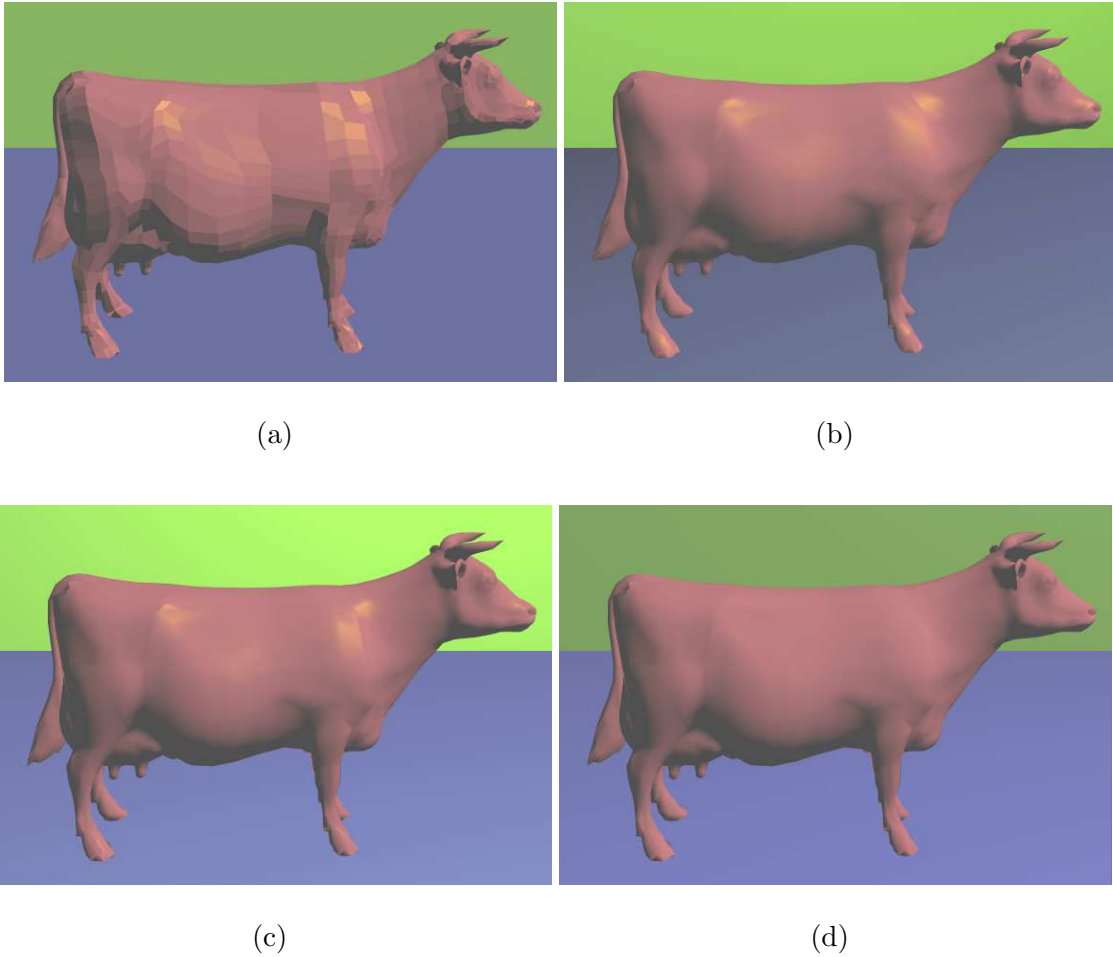


Figure 1.1. Examples of local illumination models. (a) Flat shading. (b) Gouraud shading. (c) Phong shading. (d) Phong shading with no specular component.

Materials that scatter light roughly uniformly are called *diffuse* or *Lambertian* surfaces. Few surfaces are truly diffuse, but Lambertian materials reasonably approximate matte surfaces like paper and painted walls. Equation 1.1 shows a local model for Lambertian materials:

$$I = I_a k_a O_d + f_{att} I_p k_d O_d (\vec{N} \cdot \vec{L}). \quad (1.1)$$

Here \vec{N} is the surface normal at the illuminated point, \vec{L} is the direction to the light, O_d the object's diffuse color, k_d is the material albedo, and I_p is the light intensity. I_a and k_a are the global ambient constant and the material's ambient coefficient. Note the first term in Equation 1.1 represents the ad hoc approach to approximating indirect illumination discussed above. Figure 1.1(d) shows an example of a Lambertian surface.

Since few completely diffuse materials exist, Phong introduced an illumination model that approximates glossy highlights using cosine terms [102]. Perfect reflectors, like mirrors, reflect incoming light around the surface normal (see Figure 1.2). Most other objects reflect light imperfectly, so highlighted regions appear near the reflection direction. Phong presented an empirical model that approximates these highlights using the following equation:

$$I = I_a k_a O_d + f_{att} I_p \left[k_d O_d (\vec{N} \cdot \vec{L}) + k_s (\vec{R} \cdot \vec{V})^n \right]. \quad (1.2)$$

Using the Phong model, when the viewing direction \vec{V} aligns with the reflection direction \vec{R} , the highlight is brightest. This highlight fades as the angle between \vec{V} and \vec{R} increases. Varying the material's shininess n modifies the size of the highlight. The material's specular reflection coefficient, k_s , affects the brightness of the specular highlight. However, this model only renders whitish specular highlights, which leads to plastic-like object appearance. To reduce this problem a new property O_s , the specular color of the object, is often introduced. The modified equation is then:

$$I = I_a k_a O_d + f_{att} I_p \left[k_d O_d (\vec{N} \cdot \vec{L}) + k_s O_s (\vec{R} \cdot \vec{V})^n \right]. \quad (1.3)$$

Flat, Gouraud, and Phong shading typically use the Phong illumination model (Equation 1.2). The difference between these shading techniques is how frequently illumination is sampled. Flat shading uses the same illumination over an entire polygon, whereas

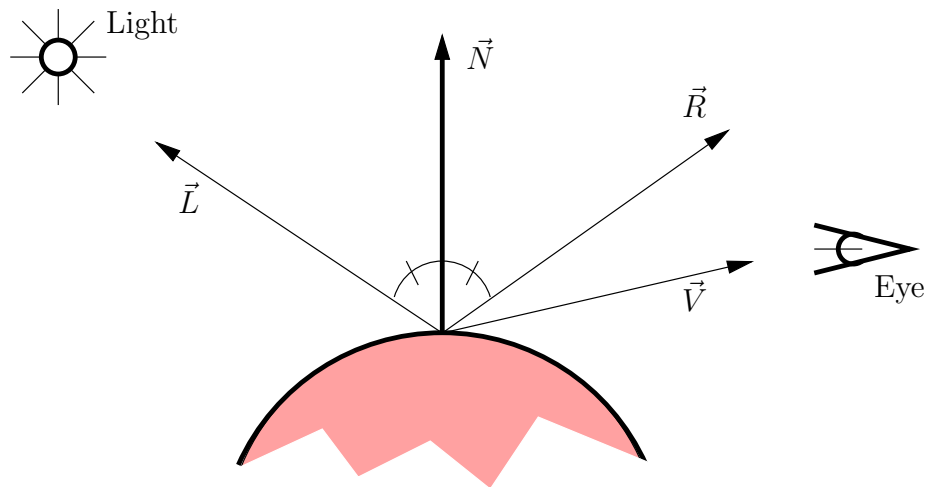


Figure 1.2. The Phong illumination model uses four vectors to determine lighting for each point. \vec{V} is the direction to the eye, \vec{L} is the direction to the light, \vec{N} is the surface normal, and \vec{R} is the reflection vector, which is \vec{L} reflected about the surface normal.

Gouraud samples the illumination at all polygon vertices and linearly interpolates the results for a smoother effect. Phong shading interpolates the normals over the polygon and performs lighting computations on a per-pixel basis. As seen in Figure 1.1, Phong shading allows highlights to span less than a single triangle, whereas Gouraud shading often spreads highlights over multiple triangles or misses them completely.

The models presented in this section run interactively and are easy to implement, but they cannot represent many of the complex effects seen in everyday environments. Shadows, reflections, interreflections, and caustics all require global information. Technically, area lights can be handled using local illumination models, but the approaches used in interactive applications typically handle only point lights.

1.2 Global Illumination

Global illumination provides much of the visual richness in typical real-world environments. For instance, indoor environments and star-lit night renderings are often almost exclusively lit by indirect illumination. Unfortunately, incorporating global information about all objects in an environment proves quite costly. In fact, generating photorealistic images requires solving the rendering equation [67] introduced by Kajiya, which models the physical transport of light. Solving this equation proves costly because it involves integrating incoming illumination recursively at every point in a scene. In fact, computation of exact solutions are feasible only in the simplest environments. Renderers generally use a numerical approximation technique to solve this integral.

Kajiya’s formulation of the rendering equation computes the intensity arriving at some point \mathbf{x} from some other point \mathbf{x}' in the environment via the following equation:

$$I(\mathbf{x}, \mathbf{x}') = g(\mathbf{x}, \mathbf{x}') \left(\varepsilon(\mathbf{x}, \mathbf{x}') + \int_{\mathbf{x}'' \in S} \rho(\mathbf{x}, \mathbf{x}', \mathbf{x}'') I(\mathbf{x}', \mathbf{x}'') d\mathbf{x}'' \right). \quad (1.4)$$

The illumination arriving at point \mathbf{x} from point \mathbf{x}' depends on the visibility, $g(\mathbf{x}, \mathbf{x}')$, between \mathbf{x} and \mathbf{x}' , the light emitted, $\varepsilon(\mathbf{x}, \mathbf{x}')$, from \mathbf{x}' to \mathbf{x} , and a sum of the illumination incident at \mathbf{x}' reflected towards \mathbf{x} . Here $\rho(\mathbf{x}, \mathbf{x}', \mathbf{x}'')$ describes how much light from \mathbf{x}'' is reflected towards \mathbf{x} at point \mathbf{x}' .

1.2.1 Radiometry

Kajiya’s rendering equation provides a framework to compute global illumination, but rendering photorealistic images also requires accurate knowledge about an environment’s lighting. The most pragmatic approaches to obtain physically accurate data are to either

measure light intensities in a real environment or allow users to input intensities in common, human-understandable units. In either case *radiometry*, the measurement of real-world radiation, proves useful. By rewriting the rendering equation in terms of radiometric properties, physical measurements can easily be incorporated into simulated environments.

The most basic radiometric property, *radiant energy*, has units of joules. *Radiant flux*, Φ describes the radiant energy Q per unit time t , or $\Phi = \frac{dQ}{dt}$. The commonly used unit for radiant flux is the watt. *Radiant flux area density* represents the radiant flux per unit area. Radiant flux area density is called *irradiance*, represented as E , when discussing power arriving at a surface and is called *radiosity*, represented as B , when referring to power leaving a surface. More explicitly:

$$E(\mathbf{x}) = \frac{d\Phi_{in}}{dA}, \quad (1.5)$$

$$B(\mathbf{x}) = \frac{d\Phi_{out}}{dA}. \quad (1.6)$$

The *radiance*, L , is defined as the energy per unit area per unit time per unit solid angle, or the radiant flux area density per unit solid angle. Given the radiant flux at point \mathbf{x} in area dA from some direction $d\vec{\omega}$ (see Figure 1.3), the radiance can be computed as

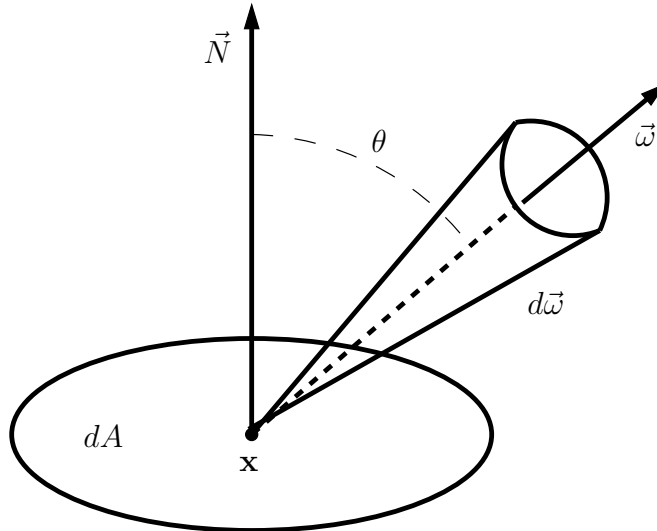


Figure 1.3. Radiance is the energy per unit area per unit time per unit solid angle $d\vec{\omega}$. If the area dA lies along a surface at point \mathbf{x} with surface normal \vec{N} , the radiance is computed using the projected area $\cos\theta dA$.

follows:

$$L(\mathbf{x}, \vec{\omega}) = \frac{d^2\Phi}{\cos\theta dA d\vec{\omega}}, \quad (1.7)$$

where $\cos\theta dA$ is the projected area of dA to the plane perpendicular to the direction $\vec{\omega}$. As an example, the energy radiated in the angle $d\vec{\omega}$ from the region dA during time dt in Figure 1.3 can be computed:

$$Q = L(\mathbf{x}, \vec{\omega}) \cos\theta dA d\vec{\omega} dt.$$

Table 1.1 summarizes the physical units of the radiometric properties introduced in this section.

1.2.2 Reflectance of Light

Another important property to consider when rendering photorealistic images is how light interacts with materials in a scene. Every material reflects light in a slightly different manner, depending on composition, age, translucency, and the microscopic surface geometry. Until the introduction of the rendering equation, however, most materials used in computer graphics were approximated by purely Lambertian models, purely specular models (i.e., perfect reflectors or refractors), or the Phong model, which gives a plastic appearance with varying specular highlights.

As more complex rendering techniques became widespread, a better representation for material properties was needed. A more realistic approximation for reflected light is the *bidirectional reflectance-distribution function*, or BRDF, introduced by Nicodemus et al. [91]. The BRDF represents the portion of light from an incoming direction $\vec{\omega}_{in}$ that reflects in a particular outgoing direction $\vec{\omega}_{out}$, hence it can represent surfaces with arbitrary reflectances. Cook and Torrance [24] and Immel et al. [57] first discussed the bidirectional reflectance in the computer graphics literature, and Cabral et al. [14] introduced the standardized notation of Nicodemus et al. Formally, the BRDF, f_r , is

Table 1.1. Units of radiometric properties.

Symbol	Property	Units
Q	Radiant energy	J
Φ	Radiant flux	W
E	Irradiance	Wm^{-2}
B	Radiosity	Wm^{-2}
L	Radiance	$Wm^{-2}sr^{-1}$

defined as the ratio of outgoing radiance to the irradiance from the incident direction $\vec{\omega}_{in}$:

$$f_r(\mathbf{x}, \vec{\omega}_{out}, \vec{\omega}_{in}) = \frac{dL(\mathbf{x}, \vec{\omega}_{out})}{dE(\mathbf{x}, \vec{\omega}_{in})} = \frac{dL(\mathbf{x}, \vec{\omega}_{out})}{L(\mathbf{x}, \vec{\omega}_{in}) \cos \theta_{in} d\vec{\omega}_{in}}. \quad (1.8)$$

The BRDF approximates the reflectance of a material, but as a function independent of surface location it cannot represent effects such as subsurface scattering and translucency. Nicodemus et al. also introduced the *bidirectional scattering-surface reflectance-distribution function*, or BSSRDF, a more general function than the BRDF which allows such effects. While the BSSRDF still only encompasses a subset of all radiative transfer [17], it allows transfer from all *geometrical optics* effects. Jensen et al. [66] recently introduced a subsurface scattering model based on the BSSRDF.

1.2.3 The Rendering Equation

Using the radiometric properties from Section 1.2.1 and the reflectance discussed in Section 1.2.2, the rendering equation can be rewritten to allow use of physically based measurements. More explicitly, the rendering equation computes an outgoing radiance from a surface based on the light emitted by the surface, the incident radiance, and the surface's material properties. Mathematically, this can be written [57]:

$$L_{out}(\mathbf{x}, \vec{\omega}_{out}) = L_{emit}(\mathbf{x}, \vec{\omega}_{out}) + \int_{\Omega} f_r(\mathbf{x}, \vec{\omega}_{out}, \vec{\omega}_{in}) L_{in}(\mathbf{x}, \vec{\omega}_{in}) \cos \theta_{in} d\vec{\omega}_{in}, \quad (1.9)$$

where L_{emit} is the radiance emitted from \mathbf{x} in direction $\vec{\omega}_{out}$, Ω is the visible hemisphere at \mathbf{x} , f_r is the BRDF, and θ_{in} is the angle between $\vec{\omega}_{in}$ and the surface normal \vec{N} at \mathbf{x} .

An interesting property of radiance is that it remains constant along a line in space, assuming no intervening surfaces. So, assuming no surface exists between \mathbf{x} and $\mathbf{x} + \alpha\vec{\omega}$,

$$L(\mathbf{x}, \vec{\omega}) = L(\mathbf{x} + \alpha\vec{\omega}, \vec{\omega}), \forall \alpha \in \mathbb{R}.$$

Because of this property, the outgoing radiance at \mathbf{x} , $L_{out}(\mathbf{x}, \vec{\omega})$, is equal to the incoming radiance at \mathbf{x}' , $L_{in}(\mathbf{x}', -\vec{\omega})$, if \mathbf{x}' is the closest surface along the line $\mathbf{x} + \alpha\vec{\omega}$. Utilizing this property, the rendering equation (Equation 1.9) becomes a recursive equation that can be solved to compute a full global illumination solution.

1.3 Motivation for Global Illumination

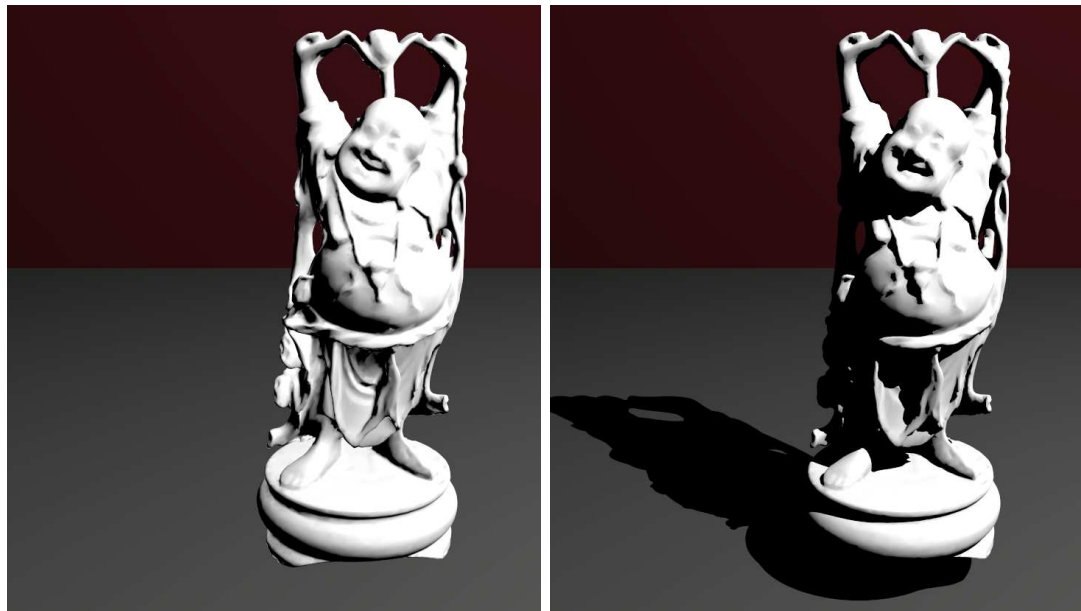
Comparing the complexity of models described in Sections 1.1 and 1.2, global illumination obviously requires significantly more computation than the commonly used

local illumination models. Considering the extra resources needed for global illumination, several important questions need to be considered. What effects does global illumination allow that local illumination does not? How important are the effects that global illumination captures? And can these global illumination computations be simplified and still capture the same important effects?

Local illumination models assume light interacts with every surface facing the source and restrict light to interact with a single surface. Thus, local illumination renders images without shadows, reflections, color bleeding, refractions, or the focusing of light. Moreover, local models typically assume light originates from point sources, so rendering outdoor scenes illuminated by the entire sky is impossible. Such effects are all common in real environments, hence for applications placing a high priority on realism the extra computation time for global illumination is worthwhile. Figure 1.4 shows the importance of a few of these global effects.

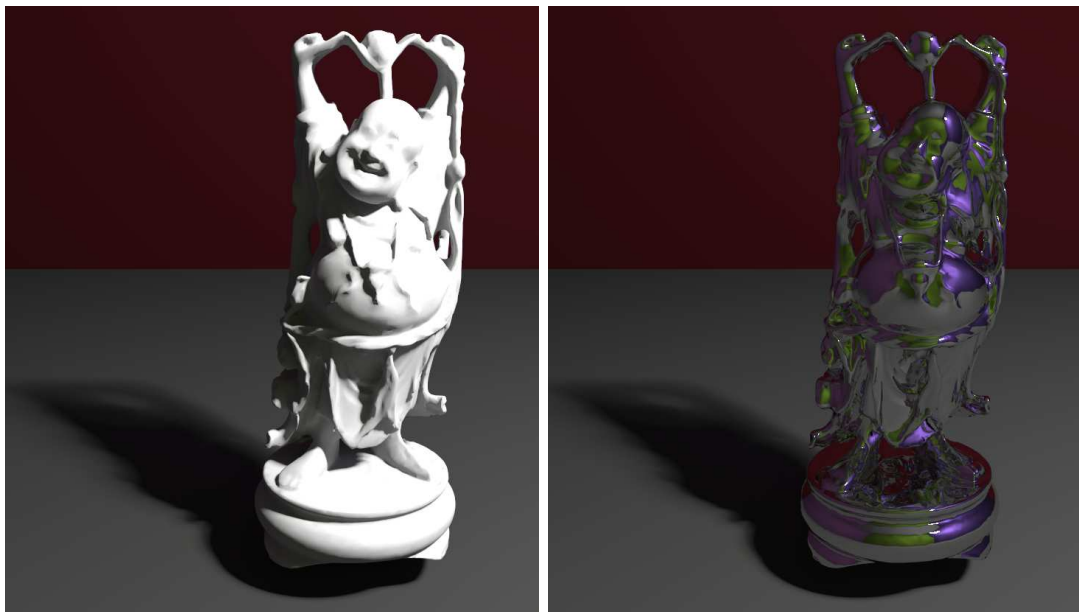
Experiments have shown shadows play an important role in human perception. Kersten et al. [71] showed that fake shadows can cause illusory motion in stationary objects. Further work by Kersten et al. [72] found an object moving along a set trajectory can appear at different depths depending on shadow location. People attach an object to its apparent shadow when determining relative locations, as shown in Figure 1.5. Accurate spatial perception may not rely on accurate shadows [144], but adding them to a synthetic scene improves both the spatial cues and the realism. For instance, changing shadow size, position, or orientation in an image can cause occluders to change apparent size or location [145]. A number of experiments have shown shadows provide important contact cues in virtual environments [56, 81].

Reflections provide other useful information in real environments. Interior designers commonly use mirrors to make rooms appear larger than their actual size [103, 104]. Diffuse reflections, also called *color bleeding* or *interreflections*, can be used for a similar effect. Painting the walls of a room white, which increases the light reflected between adjacent walls, also makes a room seem larger [103, 104]. Besides allowing similar perceptions in synthetic environments, reflections also play important roles in the appearance of many materials, especially those with significant specular coefficients. Some research suggests interreflections may provide spatial cues similar to those provided by shadows [81]. Ad hoc planar mirrored reflections are straightforward to add to locally illuminated scenes; however, reflections off curved objects are difficult [94] and lead to major artifacts without



(a)

(b)



(c)

(d)

Figure 1.4. Renderings using local, direct, and global illumination. (a) Local lighting only. (b) Direct lighting using a point light source. (c) Globally illuminated scene. (d) Globally illuminated scene with metallic (instead of Lambertian) buddha. Notice the other walls of the room have green and purple tints, which can be seen in the diffuse interreflections on the model in (c).

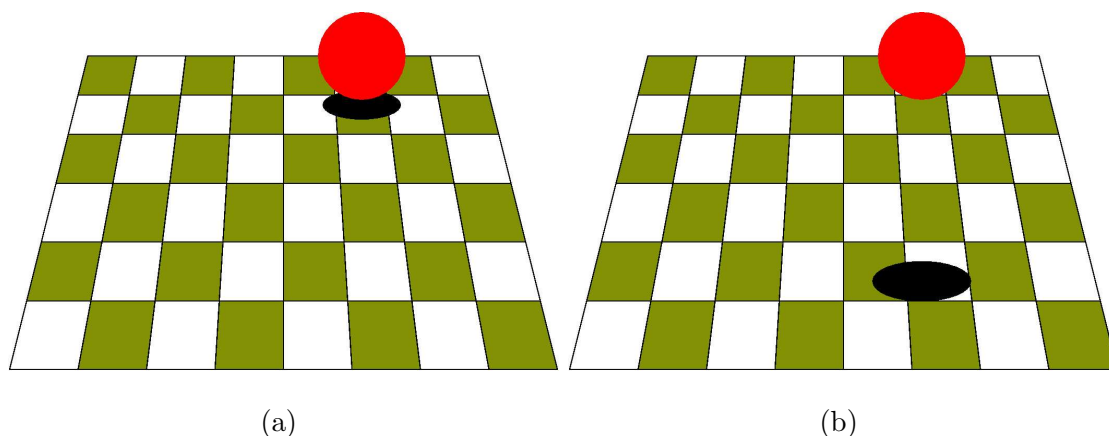


Figure 1.5. An object’s shadow affects the perception of object location. These two images are identical, except for shadow size and location.

utilizing global illumination techniques.

No studies have examined the effect of refractions on human perceptions in computer generated renderings, yet they do add significantly to the realism of a scene. Objects seen through refractive objects like magnifying glasses, textured windows, or bodies of water can appear dramatically different from the same object seen without the refraction (see Figure 1.6). The focusing of light by reflective or refractive surfaces, called a *caustic*, provides similar realism. For instance, the caustic at the bottom of a coffee cup or caused by a magnifying glass (see Figure 1.7) may or may not provide important perceptual information, but images without such caustics lack realism. Similarly, light focused by the water in a swimming pool forms caustics on the pool floor. As a common effect, renderings without underwater caustics look distinctly odd, hence films and video games frequently approximate such caustics using texture maps to help enhance realism [60, 127, 128].

In the real world, only objects with finite extent emit light. However, many interactive computer graphics applications model light sources as infinitesimal points. Using point light sources leads to illumination inaccurate in many ways. For instance, shadows have hard, crisp edges as visibility between two points is a binary function. Real light sources can be partially occluded, resulting in smoother *soft shadows*. Area light sources result in quite complex illumination as direct light arrives from a variety of directions. In addition, representing lights as spherical environment maps allows the use of lighting captured from real environments [26]. This use of natural lighting conditions has been found to improve the perceived realism of an image in certain circumstances [100, 110], though this topic

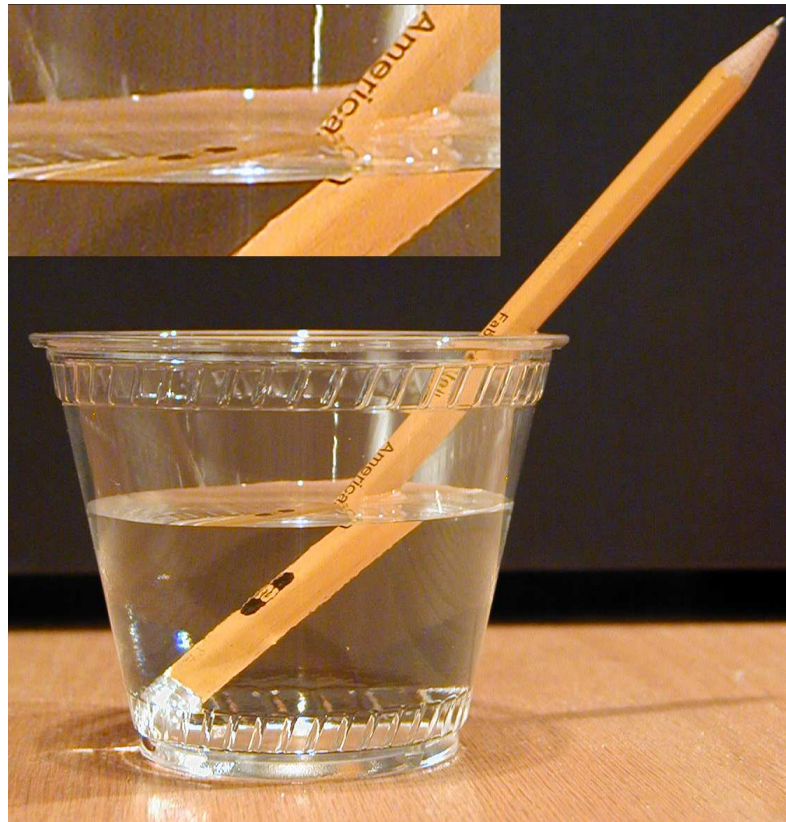


Figure 1.6. Refraction of light through the cup and water introduces apparent bends, discontinuities, and other artifacts to a typical wooden pencil. Also note the wooden table top visible in refractions where it would otherwise not appear.

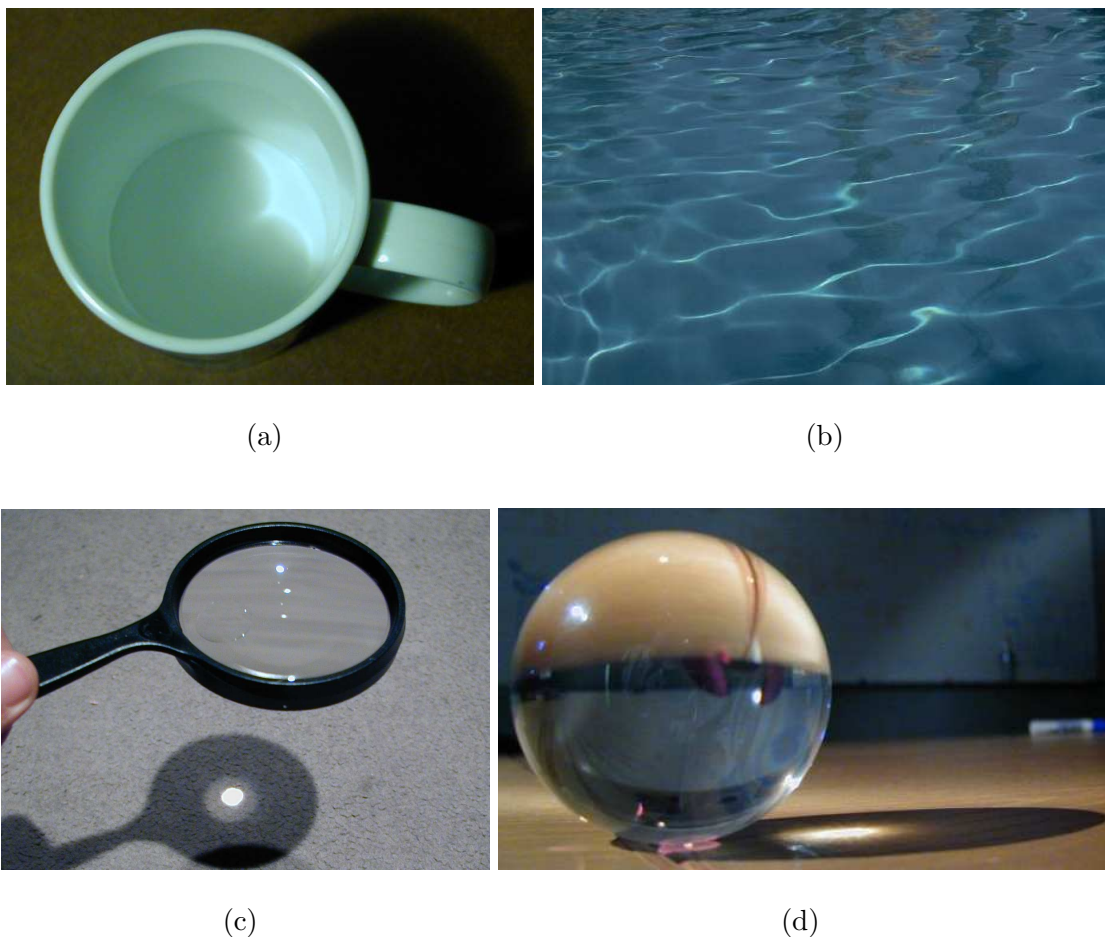


Figure 1.7. Common caustics from everyday life. (a) A cardioid at the bottom of a coffee cup. (b) Light focused on the bottom of a pool by the surface. And light focused through (c) a magnifying glass and (d) an acrylic juggling ball.

remains the subject of active research.

These global illumination effects all provide significant amounts of realism to computer generated scenes, but studies have shown that accuracy does not matter in all cases [144]. Furthermore, it may be unnecessary to accurately portray interreflections, refractions, or caustics as long as the results appear plausible.

1.4 Overview of this Work

The major obstacle to using global illumination in interactive applications is the significant computational resources required for accurate results. Many studies have shown that global illumination effects provide important perceptual cues, yet they find

that perfect illumination is usually unnecessary and in some cases even physically implausible illumination may be acceptable. This suggests techniques which simplify global illumination via approximation could render images most users accept as real.

As current interactive applications extensively utilize local illumination techniques, the approach suggested in this dissertation is to store global illumination approximations locally. With global information stored at a local level, global illumination computations simplify to lookups followed by simple computations (such as interpolation) over these local values. Such an approach easily extends current interactive techniques to add more complex lighting. This dissertation examines local ways to independently approximate three different global effects: soft shadows, caustics, and diffuse interreflections. The approaches for soft shadows and caustics rely on commonly used polygonal datasets, whereas the work on diffuse interreflection focuses on volumetric datasets used in visualization applications.

Chapter 2 discusses the goals and drawbacks of previous work in global illumination and interactive techniques. Chapter 3 examines a technique for rendering plausible approximations to soft shadows using *penumbra maps* [152], Chapter 4 describes an approach for generating interactive caustics dynamically [153], and Chapter 5 introduces a method for globally illuminating isosurfaces dynamically extracted from volumetric datasets. Finally, conclusions and future work are discussed in Chapter 6.

CHAPTER 2

PREVIOUS WORK

Researchers have long examined techniques to render more realistic illumination. Early empirical models such as Phong [102], Blinn [11], and Whitted [149] illumination were augmented by more realistic techniques such as the Cook-Torrance model [24]. The Cook-Torrance model incorporates additional information, such as the solid angle the light subtends, the slope distribution of microscopic surface facets, and the *Fresnel term*, which describes how surface reflectance varies based upon illumination angle, extinction coefficient, and index of refraction. The Cook-Torrance model renders objects more realistically than earlier empirical models, but it still relies only on local information, and thus misses many important illumination effects.

Two basic approaches emerged for computing global lighting: radiosity and raytracing. Radiosity [38] builds on ideas from radiative heat transfer [17] to model diffuse interactions between Lambertian surfaces. This allows color-bleeding to occur between nearby objects and easily incorporates the effects of uniform area lights. An additional benefit is that computed radiosities are viewpoint independent, so viewers can interactively move about a static scene without recomputing the solution. Unfortunately, radiosity is based upon energy transfer between discrete regions, so solutions are constant over these finite regions. This leads to aliasing and interpolation artifacts unless a scene is highly tessellated, in which case computation times can become prohibitive.

Raytracing shoots rays from the camera into the scene. These rays intersect scene objects to determine which surfaces are visible in a given direction. Whitted [149] extended the basic idea to a *recursive raytracer*, where rays need not terminate once they hit a surface. Instead, should a ray intersect a specular surface, it continues on in the reflected or refracted direction.

The remainder of this chapter discusses numerous categories of related work in rendering. Sections 2.1, 2.2, and 2.3 respectively discuss research related to radiosity, raytracing,

and hybrid radiosity-raytracing techniques. Sections 2.4 and 2.5 introduce research on interactively rendering two specific global illumination effects: soft shadows and caustics.

2.1 Radiosity Approaches

The basic radiosity approach [8], introduced to computer graphics by Goral et al. [38], associates a *form factor* with each pair of patches in a scene. The form factor specifies what percentage of the outgoing energy from the first patch hits the second. Using these form factors, a large linear system can be solved to compute the radiosity at each patch. Cohen and Greenberg [22] introduced the hemi-cube method for computing form factors between patches in a complex scene. By projecting scene geometry onto an imaginary cube centered on a patch, visibility information is stored in the form factor, allowing one patch to occlude portions of the light traveling between other patches.

Further work on radiosity techniques has focused on three areas: easing the restriction to exclusively diffuse materials, increasing accuracy, and speeding up the computations, either for the original solution or for dynamic scenes.

Immel et al. [57] extended standard radiosity to allow specular materials. Instead of storing a single radiance, each patch stores a directional radiance for a variety of incoming and outgoing directions. This allows surfaces with specular properties to be precomputed. Just like in diffuse radiosity, the solution is view-independent, even though view-dependent specular effects are captured. Unfortunately, with specular surfaces interpolation artifacts over patches become much more noticeable, particularly as the eyepoint moves. Additionally, since all patches are planar, curved surfaces are handled poorly.

Until Cohen et al. [21] introduced progressive radiosity, solutions were completely computed before display could begin. Progressive radiosity shoots energy progressively, one patch at a time, instead of solving the entire system of linear equations defined by a scene's form factors. This allows incremental display of the scene as computation progresses, albeit with initially coarse estimates.

Chen [19] described a method called incremental radiosity, which extends progressive radiosity to allow changes to scene properties between iterations. Thus, increasing or decreasing a light's brightness shoots incremental positive or negative light into the scene. Changing geometry involves removing energy (or shooting negative energy) contributed by the object in its former location, and adding energy contributed from the new loca-

tion. Hence, scenes can dynamically change during computations without necessitating a complete recomputation. Unfortunately, such changes can noticeably affect the scene, and propagating the changes through the radiosity solution often requires significant time, especially for dramatic changes in light intensity. In most interactive applications, where scenes continuously change, incremental radiosity never converges and can lead to objectionable lighting artifacts.

As interpolation across patches causes significant artifacts in radiosity-based renderings, a number of researchers have proposed techniques for reducing these artifacts. Hanrahan et al. [46] used a hierarchical quad-tree approach to adaptively subdivide patches as needed. Accordingly, areas where radiance changes quickly become finely subdivided. Hanrahan et al. also used this hierarchy to estimate form factors based on interactions between large patches. This reduces the standard $O(n^2)$ radiosity technique, which computes interactions between all n patches in the scene, to $O(n)$.

Interpolation artifacts still occur in hierarchical radiosity, as patches do not coincide with discontinuities in the illumination. Lischinski et al. [78] combined hierarchical radiosity with discontinuity meshing [50, 51, 77] to create patches which coincide with illumination discontinuities, such as shadow boundaries. Gortler et al. [39] generalized the idea of hierarchical radiosity by introducing wavelet radiosity, and work by Zatz [154] and Troutman and Max [134] explored the idea of representing radiosity by non-constant, higher order functions to reduce interpolation artifacts.

Radiosity techniques poorly capture specular effects and converge slowly, particularly in dynamic environments. However, when combined with the ray-based approaches described in Section 2.2, these techniques provide much of the basis for more recent interactive global illumination techniques.

2.2 Ray-based Approaches

The recursive raytracing technique introduced by Whitted [149] is an easily implementable, elegant approach to shading objects. *Distributed raytracing* [23] extends the idea to allow reflecting or refracting in a variety of directions, based on material properties. In effect, this allows a Monte Carlo sampling [89] of the material BRDF at intersection points. As most surfaces do not reflect or refract perfectly (like a mirror or window pane), distributed ray tracing allows much more realistic material properties. Additionally, by distributing rays over time, an area light, or a camera lens, effects such as motion blur,

soft shadows, and depth-of-field can be rendered. Kajiya and Von Herzen [68] extended raytracing to handle volumes such as smoke, dust, or clouds via multiple sampling of scattering functions over the volumes.

Kajiya [67] showed that all these raytracing techniques solved a subset of a more general illumination problem posed by the rendering equation (discussed in Section 1.2.3). He proposed a new approach, called *pathtracing*, which solved Equation 1.9 by Monte Carlo integration. A path describes the motion of a photon through reflections, refractions, and scattering from the light to the eye. Sampling numerous paths at every pixel in an image thus computes a full global illumination solution, with bounded error for each pixel. The results are quite compelling; however, large numbers of paths are required before images converge. Using fewer samples results in noisy images, particularly in regions containing complex paths to luminaires, like caustics.

One approach to accelerate pathtracing involves reducing path variance so that fewer samples per pixel are necessary for good results. Arvo and Kirk [7] discuss the tradeoffs between terminating rays early via *Russian roulette* and splitting rays at intersections. Spawning new rays can reduce variance by concentrating work in regions most sensitive to noise, but it can also focus more work at leaves of the ray tree, where contributions are minimal. Russian roulette stochastically terminates rays early, as if a surface absorbed the photon. This reduces the total number of rays, at the cost of slightly higher variance.

One reason for high variance in pathtraced images is the varying number of bounces before a light is hit. By combining rays cast from the eye with photons emitted from the light, *bidirectional pathtracing* [74] reduces variance by using each intersection on the light path as an emitter for points on the eye path. Considering the importance of particular paths [31, 32, 101, 123], both from the eye and the light, allows reduced numbers of paths in regions less important to the rendering, which allows higher sampling rates and reduced variance in important regions.

Observing that illumination frequently changes slowly and gradually over space, with occasional discontinuities, also suggests that caching illumination values and interpolating over relatively constant regions could significantly reduce the frequency at which expensive illumination computations must be performed. Ward et al. [146] demonstrated that such caching techniques provide significant savings for pathtracers.

The areas in a pathtraced image with greatest variance result from specular interactions. For instance, caustics are formed when light from specular objects focuses in one

small area. The paths of light causing these effects are often convoluted and difficult to sample tracing only rays from the eye. Arvo [6] suggested emanating photons from the light and storing them in *illumination maps* located on Lambertian surfaces. Using this technique, paths need not randomly bounce around numerous times before accidentally reaching a light source. Instead, at each diffuse surface, a simple lookup provides the incident illumination. Heckbert [49] proposed adaptively subdividing these illumination maps based on photon density and regions of importance, such as shadow boundaries. The bidirectional pathtracing of Lafortune and Willems [74] also extended this approach.

Jensen [64] introduced the concept of a *photon map*. Instead of storing a texture of irradiance values, as in an illumination map, the photons themselves are stored, usually in a kd-tree. When computing incident illumination at a point, contributions from the n -nearest photons are averaged. Since photon mapping does not use discrete texels, fewer photons are necessary to eliminate noise. Extensions to the photon map use importance to determine where to shoot photons [61], allow more efficient soft shadow rendering [63], eliminate the requirement for diffuse receivers [62], and allow interaction with participating media [65].

Photon mapping reduces the number of paths and photons to render complex specular effects, such as caustics, yet large numbers of photons are still required. In the case of dynamic scenes, recomputation must occur after every object movement or change of material property. Purcell et al. [105] implemented a basic photon mapping scheme on graphics hardware in an attempt for quicker rendering. Due to limitations of graphics cards, their implementation uses a simple grid-based storage scheme for photons instead of a kd-tree, reducing caustic reconstruction quality. Additionally, their approach requires a number of seconds per frame, even for simple scenes.

Bala et al. [10] stored sampled radiance in a *linetree*, which is the four-dimensional equivalent of an octree. By interpolating and reprojecting these sampled radiances when encountering similar rays, the costs of raytracing are significantly reduced. In addition, they provided bounds on the resulting errors so image fidelity can be maintained at any desired level. Radiance interpolants can provide a significant speedup over standard raytracing approaches; however, in areas where radiance varies quickly, such as in caustics, artifacts may be difficult to eliminate.

A number of approaches utilize coherency to speed up rendering times. Beam tracing [52] traces beams instead of individual rays. As adjacent rays typically hit nearby

surfaces, a single intersection can save significant computation. Veach and Guibas [136] mutated existing paths in a Monte Carlo pathtracer. Once an important path is found, mutated paths generally significantly contribute to the image as well. Recently, Chen and Arvo [18] examined perturbations of specular paths to accelerate computation of specular reflections.

2.3 Hybrid Radiosity-Raytraced Approaches

Both radiosity and ray-based approaches have advantages. Pathtracing captures any global illumination effect, albeit at great cost, whereas radiosity progressively computes view-independent diffuse solutions. Numerous researchers have examined techniques of combining these approaches to get the benefits of each while reducing variance and computation time.

Wallace et al. [140] proposed a two-pass approach. In the first pass, a radiosity solution is computed that stores diffuse to diffuse surface interactions and specular to diffuse interactions. The second pass uses a distributed raytracing approach to compute specular to specular and diffuse to specular interactions. Sillion and Puech [118] extended this two-pass approach to allow multiple specular interactions along a light path and eliminate the restriction limiting specular objects to planar patches.

Malley [82] and Maxwell et al. [85] proposed using raytracing to compute form factors between patches. By casting rays out from a patch, accurate form factors to other patches can be computed, even with complex occluding geometry. Wallace et al. [141] turned this around and gathered light at patch vertices via ray casting, which allowed smoother interpolation over patches.

Shirley [114] proposed a three-pass process that first shoots photons from luminaires via illumination mapping, then computes diffuse interreflections using a modified radiosity approach (which ignores direct lighting), and finally traces rays from the eye and performs direct lighting computations. This approach easily captures complex effects like caustics, unlike most earlier methods.

Chen et al. [20] extended hybrid approaches to provide user feedback during rendering, and allow elimination of most interpolation artifacts from the radiosity steps. Using an initial progressive radiosity pass with nondiffuse form factors computed using ray tracing, the most important effects are seen quickly. A second pass using pathtracing computes shadows and caustics, although computations focus only on bright objects that cause

such effects. A final pass uses per-pixel pathtracing to remove interpolation artifacts from the initial radiosity solution. This final pathtracing pass uses the radiosity solution for secondary reflections, so path lengths are kept short.

Keller [70] introduced a quasi-Monte Carlo approach that sends out particles from the light. Where these particles hit scene geometry, virtual lights are placed which also illuminate the scene. Accumulating direct lighting results from the virtual point lights and samples on area lights allows approximate global illumination to be computed on hardware graphics accelerators relatively quickly. Extensions allow simple specular effects, but they also increase the number of hardware passes needed for convergence. The complexity of Keller’s approach is linear in both light samples and scene complexity. Unfortunately, for high quality renderings, these values are not independent. As scene complexity increases, more samples may be required for accurate illumination reconstruction.

2.3.1 Interactive Hybrid Approaches

The hybrid approaches discussed so far attempted to reduce rendering time of photo-realistic results, but a number of hybrid approaches took the opposite approach: keeping interactive rendering speeds while still achieving as much realism as possible.

George et al. [37] provided a mechanism to update an existing progressive radiosity solution as changes occur in a dynamic environment. Before an object moves, negative energy is emitted from its patches, to counteract the energy it contributed to the current solution. After movement, positive energy is directed at it from important patches in the scene to relight the object in its new location. A similar approach can handle changing material properties.

Forsyth et al. [36] suggested a link hierarchy building on the hierarchical radiosity algorithm [46]. Links between patches can either become occluded, or need “promotion” or “demotion” between levels of the hierarchy. By using predictive link tests and extrapolation, they can compute radiosity interactively in simple scenes.

Smits et al. [122] grouped patches in a scene into clusters, which could interact on a cluster level, rather than the patch level. This allows objects that have little effect on each other to interact at a higher level, which reduces computational costs. They described two approaches to bound the error this clustering technique introduces. Depending on the acceptable approximation error, the $O(n^2)$ radiosity computation reduces to either $O(n \log n)$ or $O(n)$.

Drettakis and Sillion [30] combined clustering with an approach similar to Forsyth et al. During object motion, intersections between the object’s bounding volume and existing links are computed. Their technique expedites radiosity computations, but interactive framerates are limited to fairly simple scenes.

Granier et al. [42] proposed another approach using hierarchical radiosity with clustering for the diffuse pass, and utilizing particle tracing for specular effects. Particles contribute to surfaces based on the hierarchy, which allows acceleration of visibility computations during path tracing. Granier and Drettakis [41] extend this approach, constructing caustics directly on the radiosity mesh or in a “caustic texture,” depending on required accuracy. Furthermore, they include the line-space hierarchy of Drettakis and Sillion, allowing interactive modification of the scene. However, as with most particle tracing systems their approach works best with relatively simple scenes. The number of paths necessary for high quality increases dramatically as scene complexity increases.

2.4 Soft Shadow Techniques

Significant research has focused on creating a unified global illumination technique that renders complete illumination at interactive rates, yet other research has focused on more specific problems. Interactive raytracing-radiosity hybrids have potential, but most current applications cannot afford the expense they entail. More specific techniques, which focus on soft shadows for example, can quickly be applied in applications, as they are simpler than complete solutions.

Since shadows can significantly improve image comprehension, researchers have long examined techniques to incorporate them into existing applications that use only local illumination. Crow [25] proposed an object-space solution to compute simple hard shadows. The extrusions of an object’s silhouettes away from the light bound the shadowed region. Computing *shadow volumes*, these silhouettes and their polygonal extrusions, allows analytic computation of hard shadows for polygonal models. Another early technique introduced by Williams [150] computed shadows using an image-based approach. By storing distances to the objects nearest the light in a *shadow map*, objects further away can be correctly occluded. Because of the simplicity of shadow volumes and shadow maps, these techniques are the most widely used approaches in interactive applications, especially as both techniques are easily adaptable to acceleration on graphics hardware [53, 113]. Woo et al. [151] and Akenine-Möller and Haines [3] have surveyed

early shadow techniques and discussed their relative advantages and disadvantages.

A number of interesting extensions to these basic techniques have been introduced. Reeves et al. [109] introduced *percentage closer filtering*, which helps eliminate shadow map aliasing along shadow boundaries. Percentage closer filtering renders shadows with soft boundaries. However, this blur is proportional to a fixed parameter and does not vary with light size or distance between receiver and occluder. McCool [86] developed a hybrid approach which generates shadow volumes from shadow maps. McCool's approach does not render soft shadows, but its use may become widespread as graphics accelerators become more powerful and can implement the process independent of the CPU.

Shadow mapping and shadow volumes quickly render hard shadows. However, they do not allow generation of soft shadows, except by sampling the light many times and accumulating the result (suggested by Heckbert and Herf [48]). As with most sampling-based integral approximations, this approach requires many samples to avoid artifacts, which in this case manifest as banding. For typical scenes, at least 64 samples per light are necessary for smooth shadows. Even with modern graphics accelerators, rendering a scene an additional 64 times per frame proves prohibitive.

A number of approaches speed exact soft shadow computation. Drettakis and Fiume [29] and Steward and Ghali [132] used backprojection to compute a discontinuity mesh. Using backprojection of objects onto light sources, regions of the scene where light occlusions have similar structure are computed. A discontinuity mesh represents the boundaries of these regions on scene geometry. Using this approach dramatically reduces clipping costs for computing light visibility.

Stark and Riesenfeld [130] reformulated Lambert's formula for computing irradiance. The original formula sums over the edges of a polygon while the reformulation sums over vertices. By tracing vertices onto the image plane, this new formulation can exactly compute accurate shadows for polygonal scenes. The algorithm quickens shadow computations, yet it fails to accelerate the process enough for use in interactive applications.

Although exact shadow computations are possible to quickly compute for simple scenes with polygonal sources and occluders, they slow dramatically as scene complexity increases. Thus, many researchers have investigated approximate approaches for rendering soft shadows. Soler and Sillion [125, 126] computed approximate soft shadows by convolving an image of the light source with a projected image of the occluders. Unfortunately, their approach required lights and occluders to occupy parallel planes,

which rarely happens in real-world situations. As positions of lights and occluders diverge from parallel planes their approximation breaks down, and for very complex geometry the artifacts are quite obvious without error reduction techniques that drastically increase computation time. Additionally, this approximation breaks down as occluders approach receivers, where the shadow should become sharp.

Another image-based method, suggested by Agrawala et al. [1], samples the light, renders the scene for each sample, and warps these images into a *layered depth image*. In some ways this approach is similar to simply sampling the light many times, as scene geometry still must be rendered 64 or more times to compute accurate layered depth images. Agrawala et al. also discussed a number of approaches to speeding up this precomputation, but their results still require minutes of computation for complex scenes. In environments with dynamic geometry or illumination, such precomputation speeds are unacceptable.

An algorithm developed by Heidrich et al. [54] renders approximate soft shadows from a linear light source. At samples along the light, shadow maps are computed. Using image warping techniques, visibility percentages are computed for each point in the shadow maps. This value represents the percentage of the light seen from that location in the scene. This process can be costly for complex scenes, especially when more than two or three samples on the light are used. Additionally, a number of situations exist where artifacts occur and the technique limits scenes to two-dimensional lights.

Ouellette and Fiume [95] proposed projecting occluders onto the light, using an algorithm to find discontinuities along the edges of the light source, and using discontinuity locations to approximately determine the portion of the light occluded. The results are compelling, but projecting all objects onto every light source quickly becomes cost prohibitive, especially since nontriangular sources must be subdivided, with the projection process being repeated on each subdivided, triangular light.

Hart et al. [47] lazily computed visibility information. As a first pass, cast rays determine visible geometry. Shadow rays spawned in a uniform pattern at intersections determine some occluders. Using a flood-fill algorithm, neighboring pixels are checked to determine if the same blockers also occlude nearby regions. A second pass computes illumination for each pixel based on the blockers found during the first pass. This approach can provide significant speedups over Monte Carlo visibility evaluation at each pixel, but it has a number of problems. First, it is not designed for interactivity. Worse,

when objects are subdivided into many small triangles, each triangle casts only a very small shadow, which could easily be missed with only a few shadow rays per pixel. In such a case, a pixel deep in an umbral region may be only partially occluded.

Haines [45] introduced a technique which quickly renders a shadow texture on a plane. This technique approximates umbral regions using a hard shadow, and extends these regions with approximate penumbrae. Parker et al. [99] suggested this approach of extending hard shadows by approximate penumbral regions. Haines' approach generates plausible soft shadows when occluders lie relatively close to the shadowed plane, and is discussed further in Section 3.1.

Brabec and Seidel [12] described a technique for computing soft shadows using an image-space search of a single shadow map. If the shadow map shows a pixel as illuminated, a pixel-by-pixel search conducted in nearby regions of the shadow map determines whether the pixel lies in a penumbral region. Similarly if the shadow map shows a blocker occluding the pixel, a search of nearby shadow map texels determines if the pixel is partially illuminated. The results provide acceptable shadows quickly, but stepping artifacts appear in penumbral regions and artifacts occur near overlapping objects. Additionally pixel-by-pixel searches currently must be performed on the CPU. The illumination computation for each pixel includes such a search, so this process can become costly, especially as the shadow map size increases.

Akenine-Möller and Assarsson [2] extended the shadow volume approach to render soft shadows. Instead of computing a single shadow quadrilateral at each silhouette edge, a *penumbra wedge* that surrounds the penumbral region is computed in addition to the shadow quadrilateral. A per-fragment shader program renders these wedges into a *light buffer*, used during the final illumination pass. The problems with this technique include assuming silhouettes form closed loops with exactly two silhouette edges per vertex, requiring a 16-bit stencil buffer for use as the light buffer, and increased bandwidth requirements for the additional penumbra wedge geometry. An extension to this technique [9] eliminated most of these problems and allowed for colored area lights. However, the bandwidth limitation restricts the complexity of objects casting shadows. Even on state of the art graphics hardware, simple scenes (with a few hundred polygon occluders) render at only a few frames per second.

2.5 Caustic Techniques

Although the problem of rendering caustics has not received as much attention as soft shadow rendering, a number of researchers have proposed techniques for interactively rendering caustics. As with soft shadows, the hybrid raytracing-radiosity approaches can interactively render caustics for very simple objects, but more complex objects require significantly more time.

Watt [147] described a variant of beam tracing [52] called *light beam tracing*. In beam tracing, bundles of rays, or *beams*, are used instead of single rays. Using beams reduces computation time by utilizing coherency information between nearby rays which intersect the same surface. Watt’s light beam tracing shoots beams from the light, instead of individual photons. Each specular polygon in the scene is the base of a pyramidal light beam, with the apex at the light. These light beams can individually be reflected and refracted by specular polygons with a single transformation, rather than on a per-photon basis. This allows much quicker computation of caustics through a single specular interaction. Problems with the beam tracing approach include the limitation to a single specular interaction, which limits the applicability, and the need to highly tessellate curved surfaces in order to achieve realistic results.

Mitchell and Hanrahan [88] introduced a technique for directly computing the caustic intensity from a reflecting implicit surface. Their approach uses results from geometric optics that describe the energy in a spherical wavefront and how the wavefront interacts with reflective and refractive materials. Instead of a ray-surface intersection problem, their approach locates ellipsoid-surface tangencies. The results have few discretization artifacts, but they limit themselves to implicit surfaces and single specular interactions. Finally, their technique requires significant computational resources.

Nishita and Nakamae [92] combined metaball surfaces with *illumination volumes* (essentially light beams refracted by a single surface) using Z-buffers, A-buffers, and shadow volumes to render caustics on underwater curved objects. In addition, they handle underwater scattering effects, giving visible “shafts” of light. Like most previous techniques, this approach allows only single-interaction caustics, namely caustics from a light-water interaction, limiting the applicability to a small subset of real-world caustics. Furthermore, because each illumination volume must be recomputed and rasterized each frame, similar to a shadow volume, the cost prohibits dynamic caustics.

Stam [127] suggested dynamically computing underwater caustics may be unneces-

sary, as an approximation stored in a series of texture maps generates plausible results. Combining this approach with aperiodic texture mapping [128] noticeably reduces the periodicity resulting from a short series of caustic textures.

Diefenbach and Badler [28] utilized graphics hardware to render approximate global illumination effects quickly. They proposed using *light volumes*, analogous to shadow volumes, to bound regions where additional light should be added. These volumes are similar to refracted light beams and can be rasterized using the same stencil method [53] used for shadow volumes. Light volumes can be recursively generated as they intersect second specular surfaces. This approach does not directly render caustics, but when combined with explosion maps [94] to reflect from curved surfaces, caustic generation may be possible. Unfortunately, this approach is very fragile and requires significant fill rate (for multiple recursive shadow and light volumes). Even without caustics, this multi-pass pipeline approach requires multiple seconds per frame.

Wand and Straßer [143] proposed using recent programmability of graphics accelerators to render caustics. Using a pixel shader for every pixel P in the scene, they sample points S on a specular surface, reflect $\overrightarrow{S-P}$ around the normal at S , and index into a cube map of the surrounding environment. By sampling the surface numerous times, they perform Monte Carlo sampling of a single-bounce caustic. With current hardware, they performed three samples per rendering pass. This allows interactive framerates for a few samples per pixel (from 60–500), though caustics often require one or two orders of magnitude more samples for crisp results. However, for simple metallic objects where blurry caustics are acceptable, their approach runs interactively on current graphics accelerators.

2.6 Other Interactive Global Illumination Approaches

While hybrid radiosity-raytracing techniques and specialized approaches for specific effects have materialized, a number of other interesting techniques have been introduced. Greger et al. [44] introduced the irradiance volume which allows dynamic objects to traverse an environment and allows nearby geometry to illuminate them via diffuse interreflection. The environment is sampled on a grid and an approximation to the irradiance function is stored in each cell. Interpolation between samples allows dynamic objects to be illuminated by the scene, however dynamic objects cannot affect illumination of static geometry.

A number of approaches have achieved interactivity via brute force. Raytracing algorithms are *embarrassingly parallel*, meaning they scale linearly as additional CPUs are added to a computation. Parker et al. [96] implemented an interactive raytracer on a multiprocessor SGI Origin. Using 60 CPUs, a combination of good acceleration structures, load balancing, memory bricking, and code optimization allowed interactive framerates for fairly complex scenes. A similar interactive raytracing technique was introduced by Wald et al. [139] which uses clusters of commodity PCs to achieve interactive speeds. The approach of Wald et al. takes advantage of SIMD streaming instructions on modern commodity CPUs, reduces all objects to triangle primitives, and carefully monitors network traffic to maintain interactivity.

Wald et al. [138] extended their work to render scenes with global illumination at interactive rates. Because of a limit on rays per frame, a number of assumptions were made to expedite rendering. Instead of randomly sampling the lights at each pixel, a set number of predetermined light samples are used. In order to eliminate the structured noise resulting from this sampling, the raytracer uses a discontinuity buffer to smooth irradiance over nearby pixels. Caustics are computed using a photon map stored in a grid instead of a kd-tree, for faster creation and lookups. While this improved approach allows interactive global illumination, 5×5 pixel blocks are blurred together by the discontinuity buffer, which causes blurred caustics and noise along object boundaries. By performing an approximate importance sampling, they showed [137] that light samples can be intelligently chosen, even in complex environments with thousands of lights.

Walter et al. [142] introduced the *render cache*, which caches previous illumination computations and reprojects them as a user interacts with the environment. By reusing and reprojecting existing illumination samples, new rays and paths can be concentrated in regions that significantly change between frames. The render cache also allows frames to be generated asynchronously, rather than waiting for all illumination computations at every pixel on screen. The render cache allows interactivity without shooting rays for every pixel (similar to the approach of [10]), but high quality results require a number of frames, and artifacts and blurriness occur in regions of movement and near discontinuities.

Udeshi and Hansen [135] combined hardware acceleration and raytracing to achieve realistic effects like soft shadows, one bounce diffuse interreflections, and specular reflections in dynamic environments. Using a parallel SGI Origin with eight Infinite Reality graphics pipelines, shadows and direct illumination were computed using the graphics hardware,

and raytracing on the CPUs gave accurate specular reflections. They approximated indirect illumination by re-rendering the scene from virtual lights.

A number of recent techniques have explored compressing and storing global lighting using various basis functions. Generally these techniques rely on incident illumination from infinitely distant light sources, so that lighting remains constant over objects in the scene. Ramamoorthi and Hanrahan [106] applied spherical harmonics to environment maps to compress them to nine coefficients for each of the red, green, and blue channels. Rendering requires a simple matrix multiply followed by a dot product to accurately illuminate Lambertian materials with direct light from the environment. Programmable graphics hardware can easily implement this approach, and with third order spherical harmonics per-pixel error remains below three percent. Ramamoorthi and Hanrahan [108] extended their work to allow rendering of more complex, isotropic BRDFs by combining precomputed illumination coefficients with precomputed BRDF coefficients. By assuming a distant viewpoint (in addition to distant illumination), the spherical harmonic functions can be evaluated only once per frame instead of once per pixel, allowing for interactive rendering.

Sloan et al. [120] introduced *precomputed radiance transfer*, which allows interactive integration of incident illumination and precomputed coefficients describing radiance transfer within a single object. This approach allows interreflections, self-shadowing and low frequency caustics. Both the incident illumination and precomputed radiance transfer are represented using spherical harmonic coefficients. Observing that integration of two functions projected into the same spherical harmonic basis simplifies to a simple dot product of coefficient vectors, the illumination integral of Equation 1.9 simplifies to a few multiplies and adds, which they implement using programmable pixel shaders for interactive rendering. The results are impressive for diffuse materials, yet caustics are poorly represented because they require high frequency information eliminated by the projection of the environment map into a spherical harmonic basis. Additionally, in order for nearby objects to contribute to each other's illumination, they must remain stationary relative to each other. Radiance transfer for more complex materials must be represented by a matrix of coefficients rather than a single vector, so non-Lambertian materials significantly slow rendering times. Sloan et al. [121] extended this work to allow a combination of surface microgeometry with precomputed radiance transfer. Sloan et al. [119] compressed the spherical harmonic transfer coefficients using a variety of approaches, allowing for

high quality rendering of specular materials with fewer coefficients. Additionally, they extended the transfer function to permit subsurface scattering effects. Using newer graphics cards with extended functionality, this new approach renders interactively for dynamic illumination and viewpoint.

Ng et al. [90] suggested using a nonlinear wavelet basis instead of a spherical harmonic basis. Because wavelets have local, instead of global, support, they can compactly represent high frequency illumination in addition to low frequency lighting. They projected each row of the transfer matrix into a Harr wavelet basis, quantized the elements to eight bits, and discarded any zero coefficients, allowing for a sparse transfer matrix. As with the approach of Sloan et al., this approach requires static geometry, as recomputing the transfer matrix is expensive.

CHAPTER 3

INTERACTIVE SOFT SHADOWS USING *PENUMBRA MAPS*

Shadows provide cues to important spatial relationships. By changing shadow size, position, or orientation in an image, an object can appear to change size or location [145]. Similarly, soft shadows give contact cues. As an occluder approaches a shadowed object, its soft shadow becomes sharper. When objects touch the shadow is completely hard.

Many recent interactive applications have incorporated real-time shadows, but they generally use shadow volumes [25], shadow maps [150], or related techniques. These methods use point light sources that cast only hard shadows. Since real world lights occupy not a point but some finite area, photorealistic images require soft shadows. Thus, as interactive graphics systems become more realistic, methods for quickly rendering soft shadows are needed.

Shadows consist of two parts, an *umbra* and a *penumbra*. Umbral regions occur where a light is completely occluded from view and penumbrae occur when a light is partially visible (Figure 3.1). Until very recently the only techniques to compute these regions involved either evaluating complex visibility functions [47] or merging hard shadows rendered from various points on the light [48]. Evaluating visibility is slow, and sampling techniques produce banding artifacts unless many samples are used. Other approximations have emerged, but most do not allow dynamically moving objects to shadow arbitrary receivers.

This chapter introduces the *penumbra map* [152], which allows arbitrary polygonal objects to dynamically cast approximate soft shadows onto themselves and other arbitrary objects. A penumbra map augments a standard shadow map with penumbral intensity information. Shadows rendered using this approach (see Figure 3.2) harden when objects touch, avoid banding artifacts inherent in sampling schemes, and are generated interactively using commodity graphics hardware. Additionally, penumbra maps can leverage existing research on shadow maps (e.g. perspective shadow maps [129] or adaptive

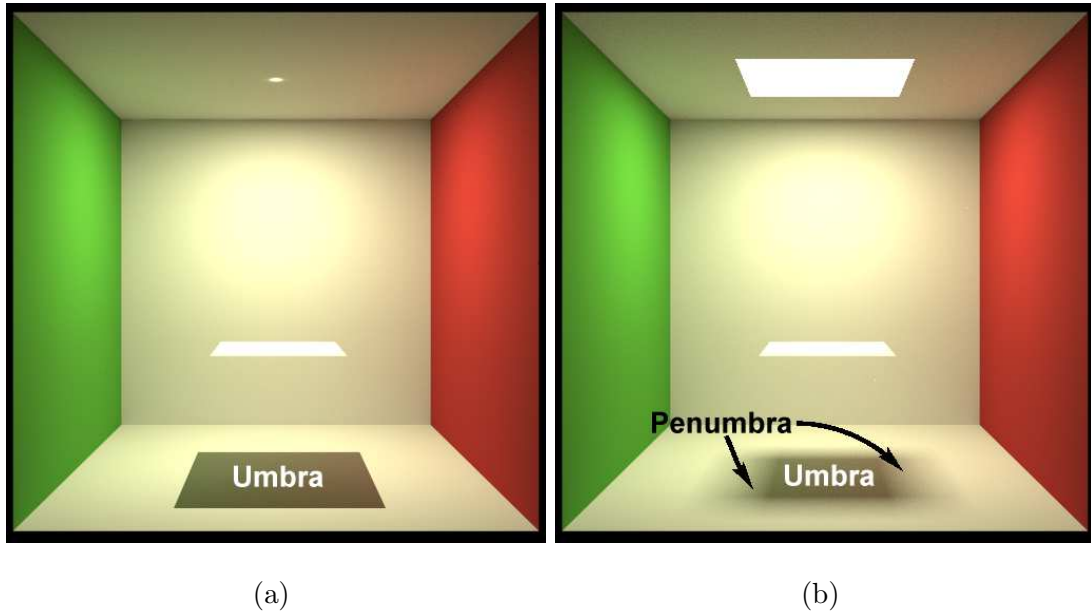


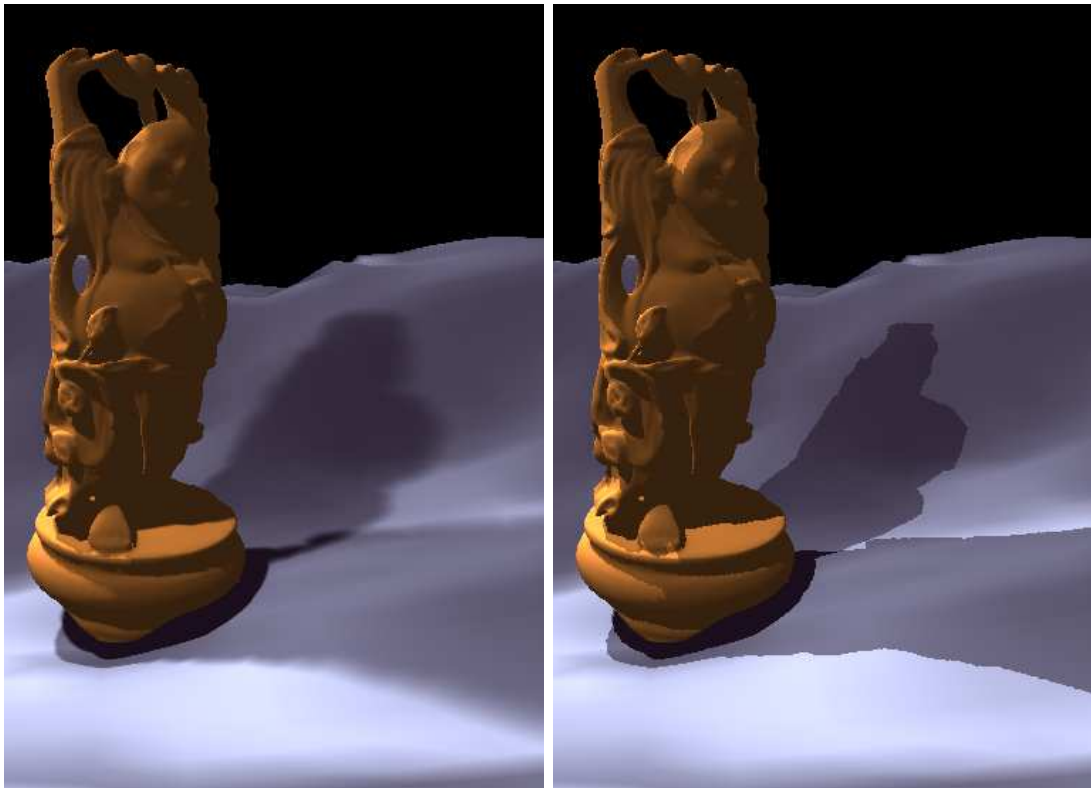
Figure 3.1. The shadow umbra includes regions where the light is completely occluded, and the penumbra occurs in regions where objects only partially occlude the light. Hard shadows (a) have only an umbra, whereas soft shadows (b) have both umbral and penumbral regions.

shadow maps [35] to help reduce shadow aliasing). On the other hand, the penumbra map approach breaks down when the umbra region shrinks significantly or completely disappears. This happens for very large area light sources or when an occluder shadows distant objects.

The next section describes related work on *shadow plateaus*, followed by a discussion of the penumbra map algorithm in Section 3.2. Section 3.3 discusses some implementational specifics and outlines the limitations. Section 3.4 presents the results.

3.1 Shadow Plateaus

Recent work by Haines [45] proposed a technique for generating approximate soft shadows on a ground plane using “plateaus.” Haines’ method creates a texture containing intensity which is used to modulate the local illumination at points on the plane to approximate a shadow. This approach first projects geometry onto the plane from the center of a light, as in Figure 3.3(a), giving a standard hard shadow, and then extends the hard shadow by an approximation to the penumbral regions, similar to the work of Parker et al. [99]. To draw these approximate penumbrae, polygons attached



(a)

(b)

Figure 3.2. Penumbra maps in a scene with multiple lights. With two penumbra maps (a), this scene runs at 21.6 fps for 1024x1024 images. Compare to shadow maps (b) which only render hard shadows.

to the silhouette edges of occluding geometry, similar to the shadow quads used for shadow volumes, are projected into the shadow texture with varying intensity based on distance to the ground plane. First, cones based at the ground plane with apexes at silhouette vertices are rendered (Figure 3.3(b)). Usually these cones are discretized into triangles for quick rendering via acceleration on graphics cards. Finally, the cones are connected by hyperboloid sheets attached to silhouette edges and tangent to adjacent cones (Figure 3.3(c)). When the adjacent cones have differing radii, the connecting sheet is nonplanar. As OpenGL and DirectX introduce artifacts when rasterizing nonplanar quadrilaterals, these sheets are subdivided into smaller triangles.

When rendered into the shadow texture, these cones and sheets have intensities of zero, for fully shadowed, at silhouette edges and one, for fully illuminated, at the ground plane. For locations in between the ground and the silhouette, the intensity is interpolated either linearly or sinusoidally, as proposed Parker et al. [99].

3.2 Penumbra Maps

Shadow plateaus give compelling shadows quickly enough for use with dynamic occluders, but this approach cannot shadow arbitrary surfaces. However, since people are often poor judges of soft shadow shape [144], similar plausible soft shadows should suffice in interactive environments. The penumbra map technique extends Haines' shadow plateau

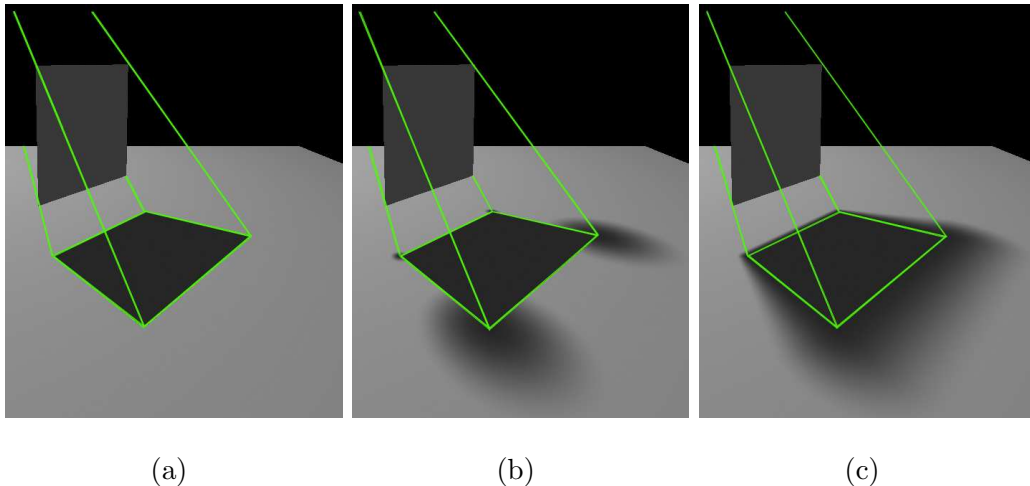


Figure 3.3. Approximate soft shadows using shadow plateaus. The shadow plateau technique generates soft shadows by (a) first rendering a hard shadow, (b) rendering cones at each silhouette vertex, (c) rendering sheets connecting the cones.

work to allow dynamic soft shadows on arbitrarily complex objects.

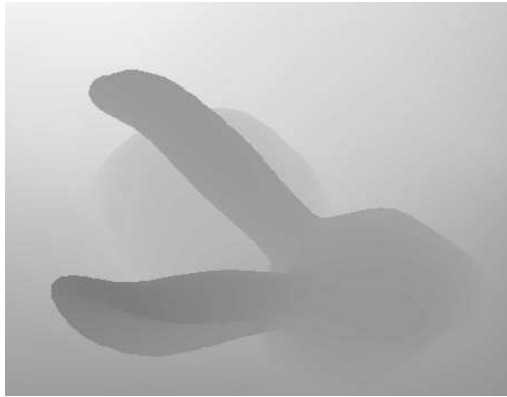
Two observations form the basis for the penumbra map technique. First, a shadow map can easily create the hard shadow to approximate an umbra. Second, if one assumes this hard shadow approximates the umbra, then the entire penumbra is visible from the point on the light used for the hard shadow. This allows the penumbra information to be stored in a single texture called a *penumbra map*. This texture stores the penumbral intensity on the foremost polygons visible from the light, just as a shadow map stores depth information about these surfaces. These observations led to similar, concurrent work by Chan and Durand [16], allowing them to render approximate soft shadows using new geometric primitives called *smoothies*.

Rendering with penumbra maps is a three-pass process. The first pass renders a standard shadow map from the viewpoint of a point light source at the approximate center of the light. The second pass renders the penumbra map. The third pass combines depth information from the shadow map and intensity information from the penumbra map to render the final image.

Let $\mathcal{V} \equiv \{v_1, v_2, \dots\}$ and $\mathcal{E} \equiv \{e_1, e_2, \dots\}$ be the set of silhouette vertices and edges, as seen from the light. Let L_r be the light radius, Z_{v_i} the depth value of vertex v_i from the light, and Z_{far} be the distance to the light's far plane. Then, to generate a penumbra map (such as in Figure 3.4):

- Clear the penumbra map to white.
- Find \mathcal{V} and \mathcal{E} for the current light.
- $\forall v_i \in \mathcal{V}$, draw a cone with tip at v_i and base at the far plane (see Figure 3.5) with a radius at the base of $C_{r_i} = \frac{(Z_{far} - Z_{v_i})L_r}{Z_{v_i}}$. Subdivide each cone into a number of triangles with one vertex at v_i and two on the far plane.
- $\forall e_i \in \mathcal{E}$, draw a sheet connecting adjacent cones. Depending on the cone radii, this quad may be nonplanar. Subdivide extremely nonplanar quads to avoid artifacts.

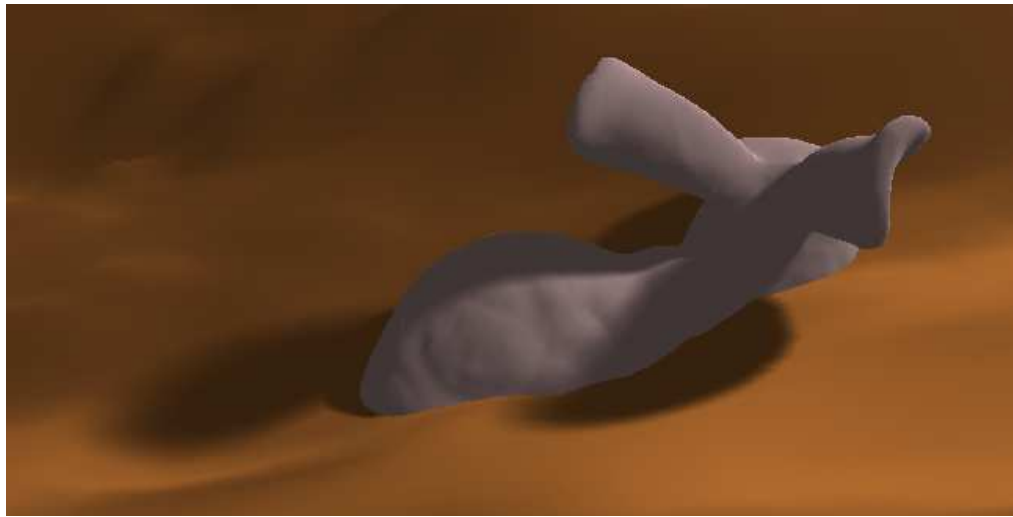
Every pixel in the penumbra map corresponds to a pixel in the shadow map. Each penumbra map pixel stores the shadow intensity at the corresponding surface in the shadow map. A fragment program applied to the penumbra sheets and cones computes this intensity using the simple geometry shown in Figure 3.6. The idea is that by using Z_{v_i} , the depth of the current cone or sheet fragment Z_F , and depth of the corresponding



(a)



(b)



(c)

Figure 3.4. Rendering using penumbra maps. (a) An example shadow map, (b) the corresponding penumbra map, and (c) the final rendered result.

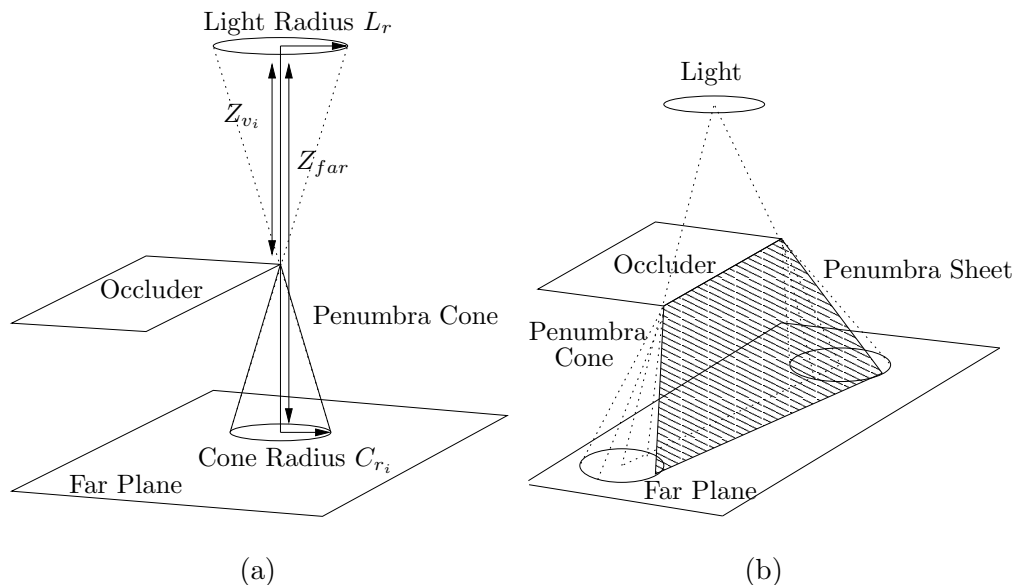


Figure 3.5. Explanation of penumbral sheets and cones. (a) Each cone's tip is located at a vertex v_i with the base located at the far plane. Simple geometry allows computation of the cone radius C_{r_i} . (b) Each sheet connects two adjacent cones.

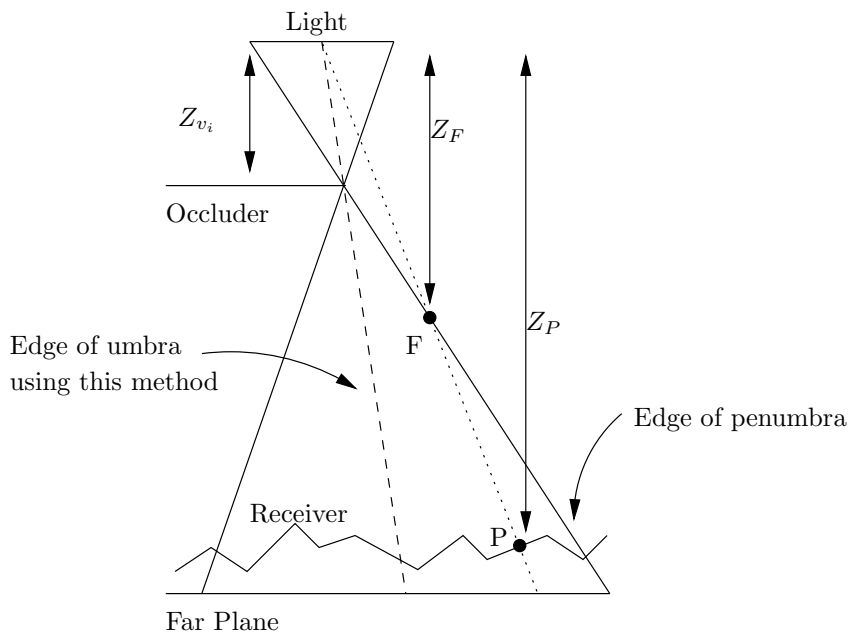


Figure 3.6. Computing per-fragment intensity from cone or sheet geometry. Each fragment F corresponds to some surface location P visible in the shadow map. By using Z_{v_i} , Z_F and Z_P , the intensity I is computed via Equation 3.1.

shadow map pixel Z_P , one can compute the light intensity at point P. Equation 3.1 specifies this computation:

$$I = 1 - \frac{Z_P - Z_F}{Z_P - Z_{v_i}} = \frac{Z_F - Z_{v_i}}{Z_P - Z_{v_i}}. \quad (3.1)$$

The CPU computes Z_{v_i} on a per-vertex basis. For cones Z_{v_i} is constant, and for sheets the graphics card's rasterizer interpolates between the Z_{v_i} values of the two adjacent cones. Z_P can be computed by referencing the shadow map, and Z_F is automatically computed by the rasterizer when processing fragment F .

This process gives a linear intensity gradient through approximate penumbral regions. Parker et al. [99] note that for spherical lights this intensity should vary sinusoidally. They approximate this sinusoidal falloff using the Bernstein interpolant $s = 3\tau^2 - 2\tau^3$. The results presented in Section 3.3 use this approximation, with the same assumption of spherical light sources.

Figure 3.7 contains pseudocode for a fragment program to compute the penumbra map (Appendix A contains the actual vertex and fragment programs). Since both the shadow map, S_{map} , and the penumbra map are rendered with the same viewing matrices, the window coordinates of fragment F can be used to find its corresponding point P in the shadow map. Due to the nonlinearity of z-buffer values, Z_F and Z_P must be converted back to world-space distances (Z'_F and Z'_P) before use. Note that Z'_F can be computed on a per-vertex basis and can be interpolated by the rasterizer to save fragment instructions. Since the penumbra map only requires a single color channel, further savings can be

```

Require: silhouette vertex depth  $Z_{v_i}$  for current cone or sheet, shadow map  $S_{map}$ 
for all fragments  $F$  on the current cone or sheet do
   $F_{coord} = GetWindowCoord( F )$ 
   $Z_P = TextureLookup( S_{map}, F_{coord} )$ 
   $Z_F = F_{coord_z}$ 
  if ( $Z_F > Z_P$ ) DiscardFragment()
   $Z'_P = ConvertToWorldSpace( Z_P )$ 
   $Z'_F = ConvertToWorldSpace( Z_F )$ 
   $I = (Z'_F - Z_{v_i}) / (Z'_P - Z_{v_i})$ 
   $I' = 3I^2 - 2I^3$ 
   $Output_{color} = I'$ 
   $Output_{depth} = I'$ 
end for

```

Figure 3.7. Pseudocode for penumbra map fragment program.

achieved by storing the shadow map and penumbra map in different channels of the same image.

Rendering soft shadows with a penumbra map is simple. For each pixel rendered from the camera's viewpoint, a comparison with the depth in the shadow map determines if the pixel is completely shadowed. If not fully shadowed, a lookup into the penumbra map gives an approximation of the light reaching the surface. Like shadow mapping, penumbra maps work in scenes with multiple light sources. Instead of computing a single shadow map and penumbra map, each light requires one of each.

3.3 Implementation

The prototype application used in this chapter makes a number of implementational choices which affect the results. First, only spherical light sources are used, because people often cannot distinguish between shadows from lights of various shapes. As Haines [45] notes, this algorithm need not be limited to spherical light sources. For example, in the case of a triangular source the cones generated for the penumbra map would have triangular bases.

Second, this prototype detects silhouettes using a brute force algorithm. A more intelligent silhouette extraction technique was not used because the graphics card was the expected bottleneck. Surprisingly, the silhouette code takes 30% of the prototype's render time. Obviously, fast silhouette techniques would be used for future interactive applications.

One detail that complicates implementation is how to deal with overlapping shadows. Given two silhouette edges with overlapping penumbral regions, there are multiple ways of counting their contributions (see Figure 3.8). When one shadow completely contains another only the darkest shadow should be used. If just the penumbrae overlap the shadow contributions should be summed. Often when the object silhouettes intersect, multiplication best approximates the true interaction. Unfortunately, there does not seem to be a straightforward way to determine which of the three methods to use on a per-fragment basis during cone and sheet rasterization. The prototype implementation uses a modified depth test to determine which cone or sheet shades a particular fragment in the penumbra map. As the pseudocode above shows, the penumbra intensity is stored in the depth channel and `glDepthFunc(GL_LESS)` is used to always choose the darkest shadow in a given pixel. This leads to artifacts in the shadows. As in Haines' work,

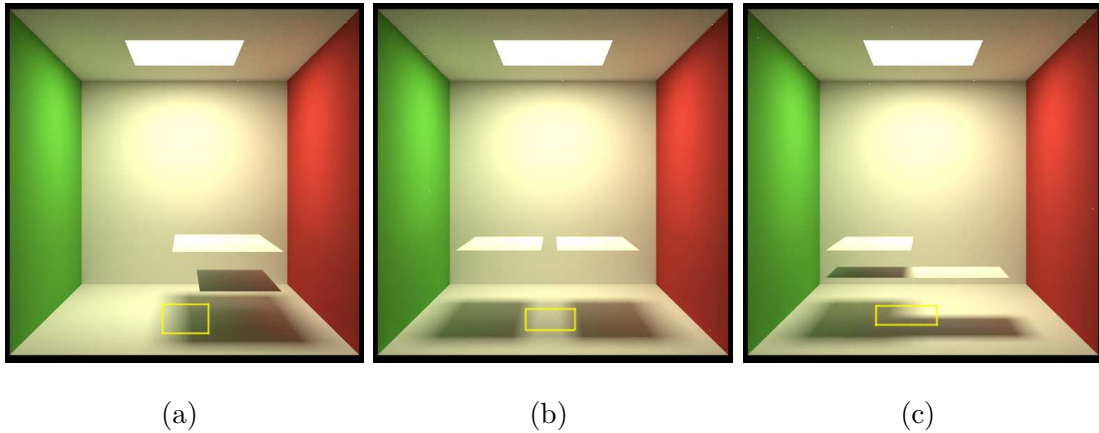


Figure 3.8. These pathtraced images show three different types of interactions between overlapping penumbra. (a) Only the darkest contribution is needed, (b) shadow contributions should be summed, and (c) multiplying the contributions from the two polygons best approximates the result.

these are most noticeable at silhouette concavities. Such artifacts worsen as the size of the penumbra increases.

3.3.1 Discussion of Limitations

This work assumes that object silhouettes remain constant over the area of a light and that the umbra can be approximated by a hard shadow. Akenine-Möller and Assarsson [2] and Haines [45] also use silhouettes computed at a single point on the light. Brabec and Seidel’s [12] technique implicitly makes this assumption by using only a single depth map. Obviously as an area light increases in size, silhouettes vary more over the light so the generated shadows will become less realistic.

Approximating the umbra by a hard shadow proves reasonable in many cases, as most people are poor judges of soft shadow shape [144]. If plausible soft shadows are required in an interactive application, using a hard shadow for the umbra may be sufficient. As a shadow’s umbra size shrinks, such approximation leads to noticeably larger, darker shadows. Shadow umbrae shrink as light size grows and as occluders and receivers move further apart. Thus, penumbra maps work best for relatively small light sources and occlusions between nearby objects.

3.4 Results

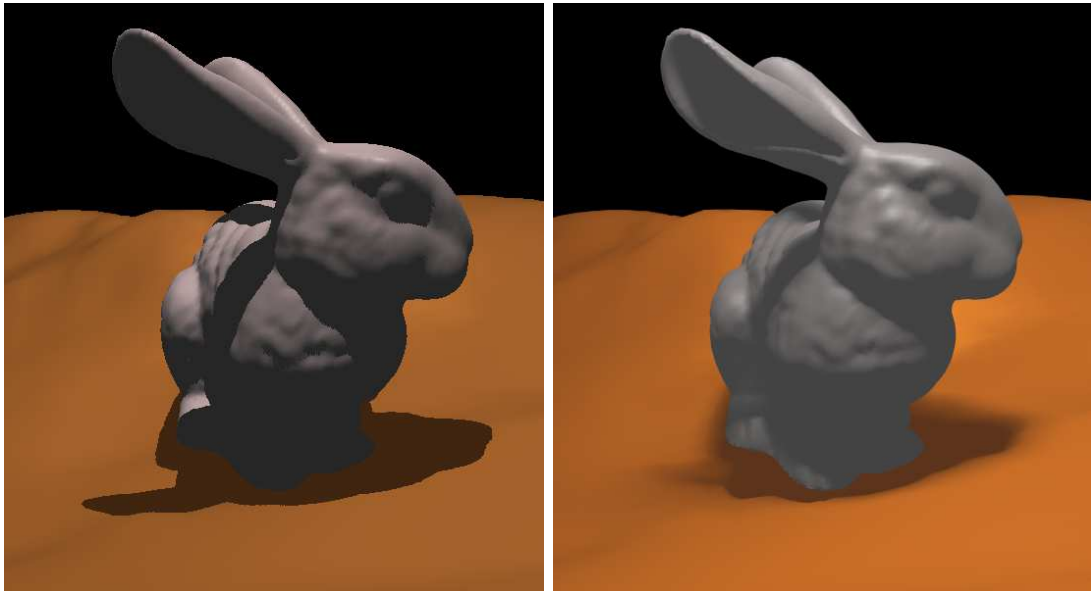
The prototype penumbra map implementation uses OpenGL and was tested on three systems: a 2.0 GHz Pentium 4 PC with an ATI Radeon 9700 PRO graphics card, a 2.66 GHz Pentium 4 PC with an nVidia GeForce 5900 Ultra graphics card, and a 3.2 GHz Pentium 4 PC with a prerelease nVidia GeForce 6800 GT graphics card (with a 300 MHz core clock speed and 500 MHz DDR memory). Vertex and fragment shaders (see Appendix A) utilize the OpenGL `ARB_vertex_program` and `ARB_fragment_program` extensions. Both the shadow and penumbra maps are rendered into p-buffer textures, a type of onboard memory buffer, for direct use without necessitating a read-back through main memory.

All scenes are rendered at 1024 x 1024 with shadow and penumbra maps of the same size. As soft shadows effectively blur detail, simplified models of complex objects such as the bunny, buddha, and dragon can be used to render the shadow and penumbra maps while still retaining equivalent quality shadows. This increases aliasing artifacts, though adding a larger bias can help reduce them. 10,000 polygon models were used to generate shadows for the bunny and the dragon (Figures 3.9 and 3.10). Buddha’s shadow (Figure 3.2) uses 5,000 polygons. Table 3.1 shows framerates for these models using penumbra and shadow maps. Note that for comparison purposes, the hard shadows were timed using a fragment program similar to the one used for penumbra maps. This program computes the Phong lighting and performs the lookup into the shadow map, which is significantly slower than using other capabilities of the hardware designed specifically for those operations.

Thirty percent of the computation time is used for brute force silhouette extraction. Thirty-five percent is spent rendering the penumbra map and the render pass consumes the remaining time. Note that the render pass includes fragment code to perform lighting

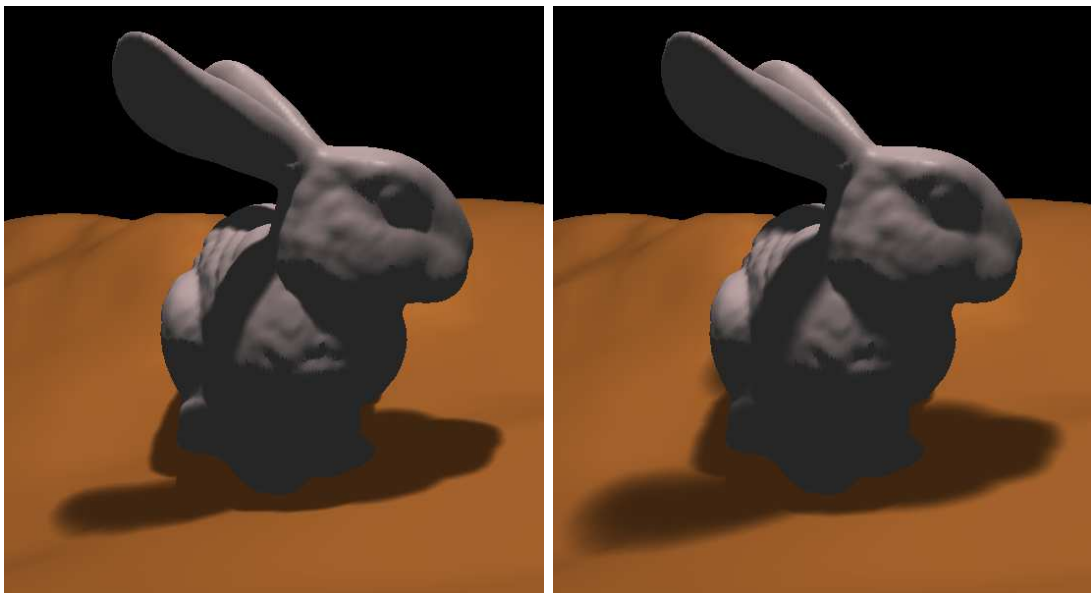
Table 3.1. Framerate comparison between shadow and penumbra maps.

Object	Penumbra Map on a Radeon 9700 PRO	Shadow Map on a Radeon 9700 PRO	Penumbra Map on a GeForce 5800 Ultra	Shadow Map on a GeForce 5800 Ultra	Penumbra Map on a GeForce 6800 GT	Shadow Map on a GeForce 6800 GT
Bunny	18.1	42.0	19.9	30.0	67.9	97.2
Dragon	14.5	48.1	15.0	30.0	44.9	108.2
Buddha, 1 Light	18.1	48.1	15.0	30.0	45.3	109.3
Buddha, 2 Lights	11.0	27.4	6.67	20.0	21.6	68.8



(a)

(b)



(c)

(d)

Figure 3.9. Penumbra map results for the Stanford bunny. Comparison of shadow maps (a), penumbra maps with two different sized lights (c,d), and a pathtraced shadow using the larger light (b). For this data set, a 10,000 polygon model is used to render the shadows onto the full ($\sim 70,000$ polygon) model.

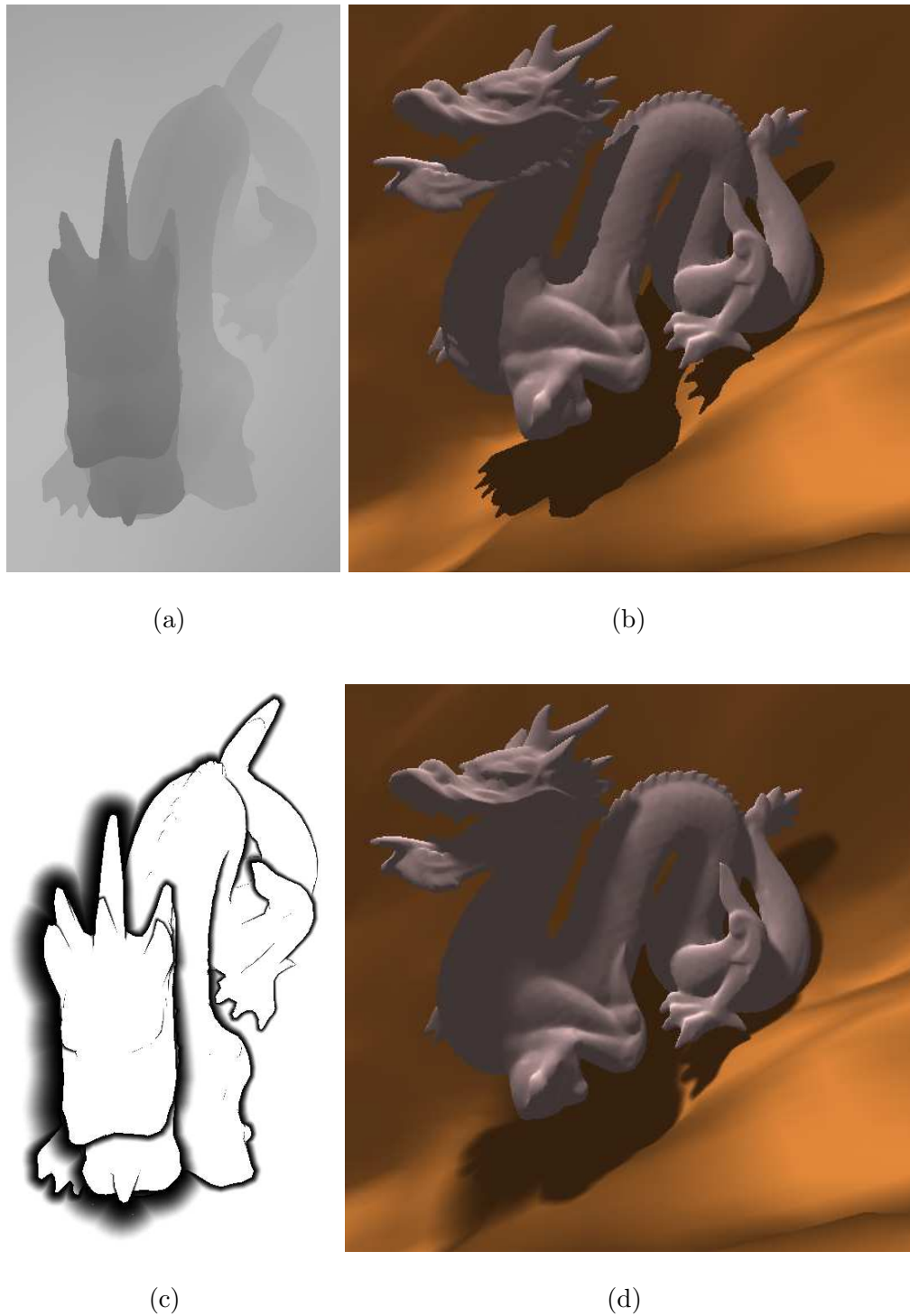


Figure 3.10. Penumbra map results for the dragon model. Using a standard shadow map (a) results in hard shadows (b), add a penumbra map (c) to get soft shadows (d). Using a 10,000 polygon dragon model for shadow generation and a 50,000 polygon model to render, 1024×1024 images render at 44.9 fps.

computations and check light visibility using the shadow map. These operations take 15 of the 22 instructions in the ARB fragment program. To render penumbra maps, the prototype application uses a fragment program with 24 assembler instructions. See Appendix A for these shader programs.

This chapter presented the *penumbra map*, a new technique for rendering approximate soft shadows in real-time. Penumbra maps allow dynamically moving polygonal models to cast soft shadows onto themselves and other complex objects. These results work best for relatively small penumbrae. Penumbra maps provide a simple multipass extension to shadow mapping for easy incorporation into existing shadow map-based systems.

CHAPTER 4

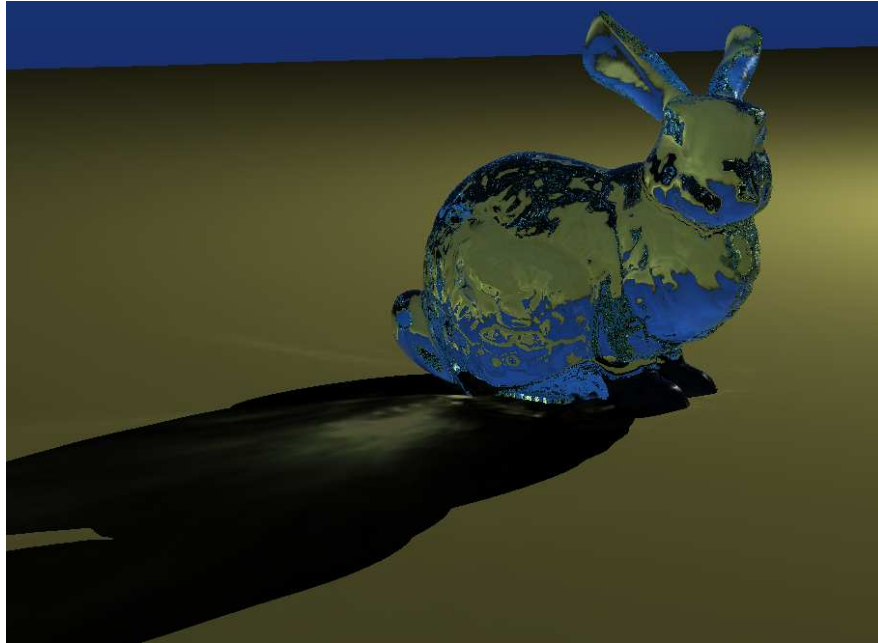
INTERACTIVE RENDERING OF CAUSTICS

Daily life immerses everyone in environments rich in illumination, particularly complicated specular effects such as caustics. These effects are important to capture in computer renderings. Unfortunately rendering complex illumination such as a caustic often incurs a significant computational cost. Since many applications require interactive speeds, costly path tracing algorithms for computing caustics are often infeasible, and hybrid techniques suffer from a common computer graphics problem—poor scaling with scene complexity. Often techniques that run quickly on simple scenes bog down when used on a complex environment.

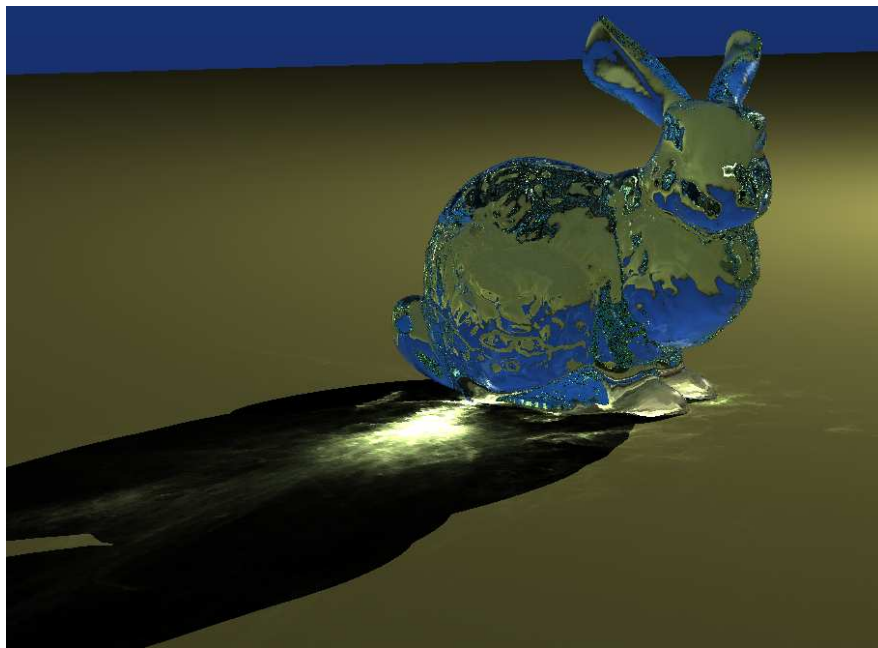
Although global illumination appears to have a significant impact upon how humans view interactions between objects, computing a full global illumination solution is often unnecessary. In fact, global illumination provides humans perceptual cues as to relative object locations, yet accuracy is not always important [56, 71]. Some researchers [111] have looked into simplifying the environment to reduce unnecessary computations, but questions remain as to what level of simplification compromises the perceived quality of global illumination.

This chapter examines the focusing of light caused by reflective and refractive surfaces. This focusing, known as a “caustic,” potentially affects the entire environment, yet in most cases appears in a relatively localized space around a specular object. For example, one might see a caustic from a glass figurine on a table (see Figure 4.1) or the caustic from a mirror on an adjacent wall.

This chapter explores a technique for sampling the caustic near a focusing object. This allows the reduction of caustic rendering to a localized property which can be computed with a simple lookup. This lookup can be performed at interactive framerates, even as objects and lights move. However, sampling takes significant precomputation and memory, and accurate caustics are limited to the sampled region.



(a)



(b)

Figure 4.1. A scene with caustics from a glass bunny. Using a raytracer running on 30 processors, this scene (a) runs at 2.3 fps while allowing movement of either the bunny or the light, compared to (b) 25 seconds for shooting photons for a photon mapped image.

The rest of this chapter is divided as follows. Section 4.1 discusses the behavior of caustics and suggests ways to deal with their complexities. Section 4.2 discusses various ways to sample a caustic and the tradeoffs involved and Section 4.3 discusses some issues involved in rendering a caustic from sampled data. Section 4.4 presents the results. Finally, Section 4.5 discusses conclusions and future work.

4.1 Caustics

This section describes the behavior of caustics and discusses assumptions and simplifications used to interactively render caustics. The goal was to develop a method that locally approximates a caustic, which requires little or no recomputation from frame to frame even as objects and lights move.

4.1.1 Caustic Behavior

Caustics result from focused light due to reflection or refraction off specular surfaces [93]. Some examples of caustics in daily life include sunlight reflected off a watch onto a car ceiling, the cardioid shape at the bottom of a coffee mug (Figure 1.7(a)), and the focusing of light through a magnifying glass (Figure 1.7(c)).

Caustics are common, yet few people understand exactly how they should look. For example, one would expect a glass figure to cast a caustic onto a table, but blurred, slightly offset, or even missing details may go unnoticed.

Flat surfaces, like mirrors, reflect light without focusing it. However any concave reflector focuses light into bright lines or points. Technically, only curved surfaces cause caustics, but this chapter adopts the common graphics usage and refers to *any* specularly reflected or refracted light as a caustic, as both planar and curved specular surfaces lead to important illumination effects.

Consider a transmissive object fixed relative to a lightsource, as in Figure 4.2. The caustic's intensity at point \mathbf{p} changes based upon the position of \mathbf{p} relative to the object and the normal \vec{N}_p of the surface at \mathbf{p} . For fixed light and object positions, the caustic can be considered a five-dimensional function. Allowing the light (or equivalently the object O) to move changes the caustic into a eight-dimensional function, by allowing the vector \vec{L} to vary.

Rendering caustics interactively involves quickly evaluating this eight-dimensional caustic intensity function. Unfortunately, analytical descriptions of an arbitrary object's

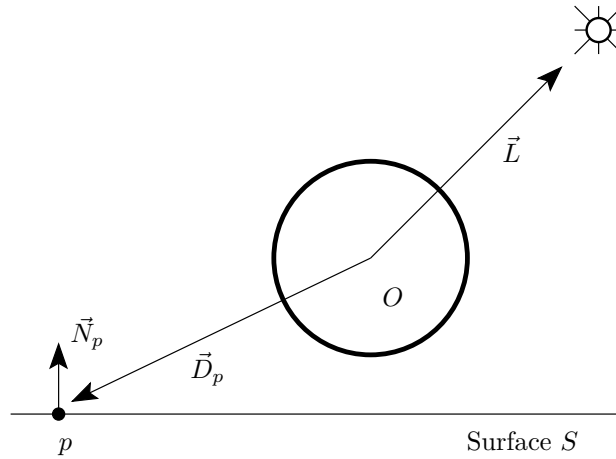


Figure 4.2. The eight dimensions of a caustic. Given the object O at point \mathbf{p} on surface S , the caustic function has three dimensions from \vec{D}_p , three dimensions from \vec{L} , and two dimensions from the orientation \vec{N}_p of the receiving surface relative to \vec{D}_p .

caustic cannot be obtained using current methods, so a numerical approximation to this function is used.

4.1.2 Simplifying the Problem

A number of simple observations allow simplification of the problem:

- The direction of incoming light often has greater impact on the visible caustic than distance to the light.
- Lights located relatively far away generate caustics similar to those of lights located infinitely far away.
- Most objects that focus light are relatively far away from the light. The most prevalent exception, mirrors in light fixtures, can usually be treated as part of the lightsource (e.g., Canned Lightsources [55]).
- The most complex caustic behavior usually occurs in regions near the focusing object.

These observations allow some simplifying assumptions. Combining the first two observations, a directional light source can replace point lights (i.e., ignoring the distance to the light). Using directional light sources reduces the dimensionality of the problem by

one.

Furthermore, limiting caustics to some finite volume around a reflective or refractive surface allows samples to be focused in regions where the caustics contributes significantly to the illumination of other objects. This allows sampling \vec{D}_p over a finite region. Outside this region, extrapolated samples from the outermost samples can approximate the caustic. Alternately, outside the sampling region caustic contributions could be gradually faded. Note that considering the caustic a local object property limits interactively rendered caustics to diffuse surfaces, to avoid specularly reflecting the precomputed caustic.

Finally, assuming a known surface orientation, $\vec{N}_{p_{fixed}}$, reduces the dimensionality by two. Incorporating this known surface orientation into the sampling allows approximation of the caustic for an arbitrary orientation \vec{N}_p by multiplying the precomputed intensity by $\vec{N}_p \cdot \vec{N}_{p_{fixed}}$. This approach was found to work for $\vec{N}_{p_{fixed}} = -\hat{D}_p = -\vec{D}_p / \|\vec{D}_p\|$ at each sample \mathbf{p} . Conceptually, this method treats all caustic light from O as coming from a point light at O 's center and computes the caustic intensity at \mathbf{p} using a cosine falloff based on $\vec{N}_p \cdot -\hat{D}_p$. As discussed above, the local sampling limits rendered caustics to mainly diffuse surfaces, so using a cosine falloff is appropriate.

Using these assumptions a simplified five-dimensional caustic function can be sampled. These five dimensions are x, y, z, ϕ , and θ , where $\vec{D}_p = (x, y, z)$, and ϕ and θ correspond to the direction of \hat{L} .

4.2 Caustic Sampling

This section outlines a number of approaches for sampling and representing the five dimensional caustic function discussed above. Since these sampled caustics are local properties of an object, sampling must be independently performed on each object which focuses light. Sampling of the volume over x, y , and z is discussed separately from the sampling of incoming light directions ϕ and θ .

4.2.1 Sampling the Light

For each caustic object, information about how the caustic changes as the light moves must be stored. Due to the assumption of directional lighting, sampling varying light positions is equivalent to sampling directions (ϕ, θ) over a unit sphere. Each such sample (ϕ_i, θ_i) is referred to as a *light sample* \hat{L}_i .

Sampling ϕ and θ in a fixed, uniform or near-uniform, pattern generally works as well as adaptively sampling. Each linear change in ϕ or θ corresponds to varying nonlinear changes (see Figure 4.3) in the caustic intensity over the volume (x, y, z) . Because incoming light often bounces around the object many times, few incoming directions \hat{L} have a “simpler” caustic behavior than others. Thus, adaptive sampling of the sphere tends to quickly converge to a relatively uniform sampling.

The rest of this chapter uses ϕ and θ sampled on a geodesic. Specifically, we subdivide an icosahedron between three and six times and project the vertices to the unit sphere. Samples can be taken as either the vertices or centers of the subdivided triangles. This provides a nearly uniform sampling over the sphere, but has the advantage that existing samples need not be recomputed for denser samplings (i.e., subdivisions) of the sphere.

4.2.2 Sampling Space

For each light sample \hat{L}_i , some region around object O should be sampled. If the object has a bounding volume of radius r , tests showed a region with radius $\approx 3r$ should be sampled to capture the most important regions of the caustic. However, this varies depending on where focal points of the object lie.

Two different approaches to storing volumetric samples were examined, a uniform grid and a set of concentric shells subdivided as a geodesic (see Figure 4.4). After selecting a representation for the volume, sampling the caustic function uses the following algorithm. For each light sample \hat{L}_i , we shoot photons from the directional lightsource towards the object O . Once a photon specularly bounces, it contributes to all the cells it passes through (the dashed lines in Figure 4.4).

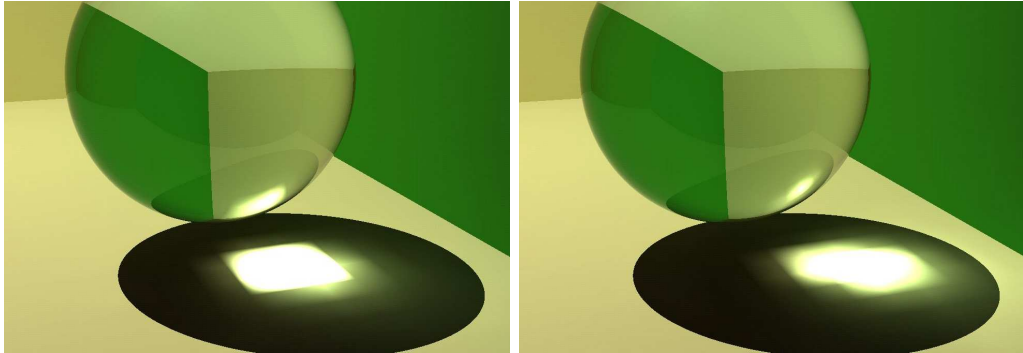


Figure 4.3. Popping between adjacent light samples. Here a minute change in object position results in a nonlinear change to the caustic, as a different light sample is used after movement.

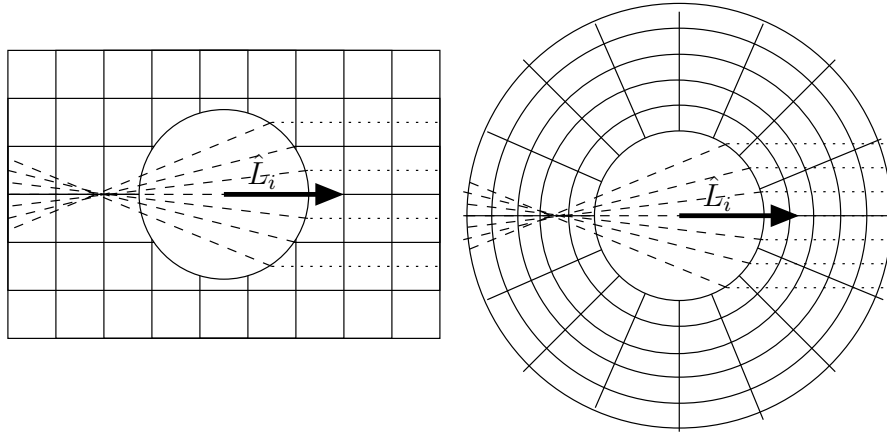


Figure 4.4. Sampling space on either a uniform grid or a set of concentric shells.

A photon’s contribution to a cell is computed as if it hit a surface at the sample point \mathbf{p}_s with surface normal in the direction of $O_{center} - \mathbf{p}_s$. Each sample point \mathbf{p}_s stores only the caustic intensity (i.e., no direct lighting is included), so contributions from nonreflected and nonrefracted photons are ignored. The result is a grid storing approximate irradiance at each cell’s center (similar to the Irradiance Volume [44]), with the caveat that only irradiance due to specularly reflected light is stored.

Storing data on a grid has the advantage of easy implementation and fast lookups. However, a rectangular grid structure does not correspond well to caustic data because intensity data changes in a generally radial fashion. This means much space is wasted storing data which changes slowly and not enough is concentrated in regions where the caustic changes quickly.

Storing data on concentric shells allows nonuniform placement of the shells to densely sample the data radially in regions where the caustic varies significantly. Using this allows a reduction of the sampling frequency in one dimension by up to a factor of five, either reducing memory usage or allowing a finer sampling in other dimensions. To avoid the difficulty of indexing into a geodesic, a table lookup is used.

4.2.3 Data Representation

One of the major problems with sampling a high dimensional function, such as the caustic intensity, is the large storage requirement. Using such data in interactive applications can be difficult if significant portions must remain in memory. A number of methods to represent these data can reduce the memory overhead. Each approach has

its advantages and disadvantages.

A naive implementation stores a complete set of sampled data, both on disk and in memory. Obviously, this requires a machine with lots of memory. For instance, storing all sampled data for the ring images (see Figure 4.5) requires around a gigabyte of memory, with data stored in colors of three bytes each: one byte for each the red, green, and blue channels. The advantage of this technique is easy implementation and fast lookups, leading to faster framerates when the data completely resides in main memory. Since caustics typically have a large dynamic range, we cannot use these bytes to store the usual values in the range $[0, 1]$. The examples shown require intensity values in the $[0, 3]$

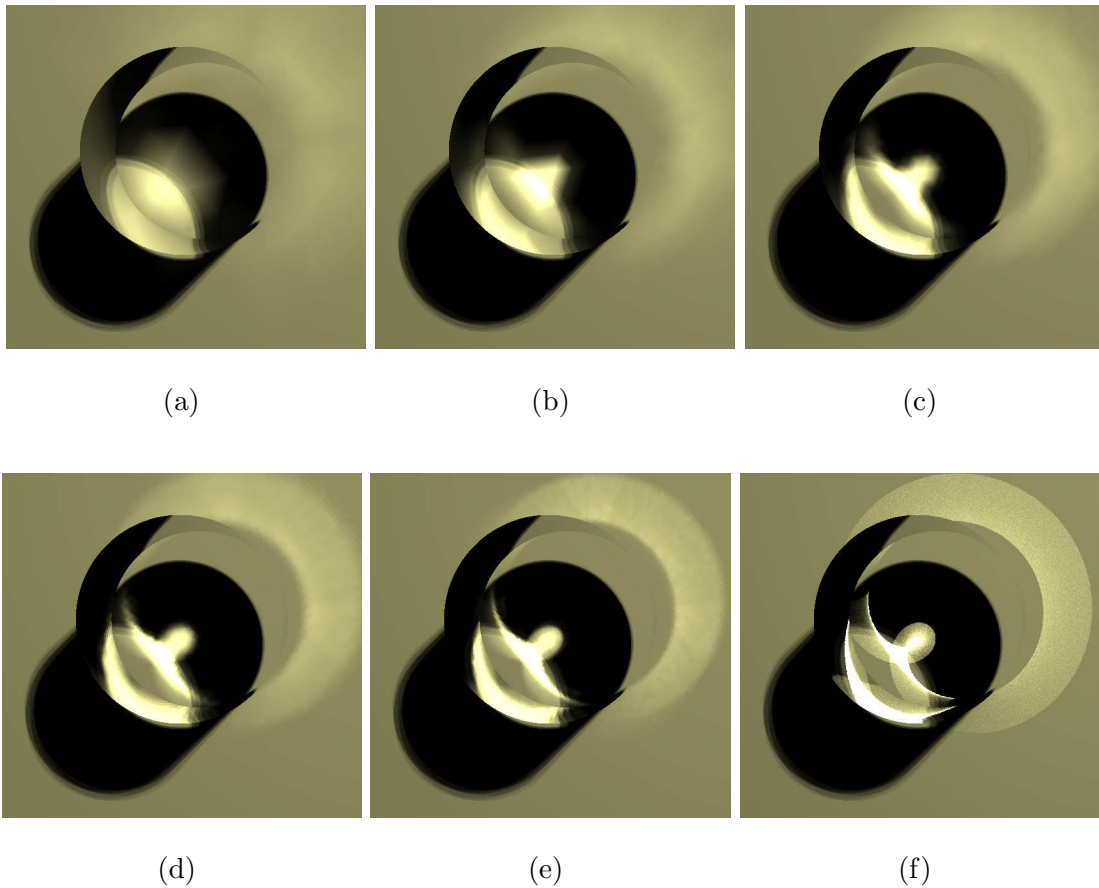


Figure 4.5. Sharper caustics come at the expense of denser sampling. The images shown require (a) 5.7, (b) 22.5, (c) 90.1, (d) 360, and (e) 1440 kilobytes of memory per light sample. The data is stored using the concentric shell representation. Compare to (f) a photon traced solution. Using a multiresolution approach, similar results require (a) 4.8, (b) 12.6, (c) 29.5, (d) 70.4, and (e) 179 kilobytes of memory per light sample.

range. Using 8-bit values in this way obviously reduces precision; however, when using interpolation to get the irradiance at each point, no significant degradation in quality was noticed.

A multiresolution approach helps save memory. Multiresolution techniques that adaptively subdivide the sampled geodesic as needed often reduce memory usage by up to a factor of 10 with equivalent quality results. The tradeoff is that lookups take longer due to the more expensive data traversal routines, leading to moderately reduced framerates. Additionally, multiresolution approaches may not always reduce storage space.

Using spherical harmonics coefficients (see Appendix B) to represent sampled data also allows significant compression. For each cell in the volume, instead of storing a color for each light sample \hat{L}_i , spherical harmonic coefficients approximating the transfer function from the environmental luminaire to a sample point are stored. Alternately, each set of spherical harmonic coefficients can represent the transfer from a light sample to a single concentric shell, though rendering using the first approach is faster and more straightforward.

One main advantage of spherical harmonics is that a large amount of data can be approximated by a few coefficients. The major problem with the representation, however, is that spherical harmonics eliminate most of the high frequency information in a caustic. Such sharp features are believed to be very important for rendering caustics. Higher order spherical harmonics better represent sharp features, but increasing the order of the spherical harmonic approximation increases precomputation, significantly increases the number of coefficients required, and decreases rendering speed.

4.3 Caustic Rendering

After sampling the five-dimensional caustic function, a number of approaches can be used to render the caustic. Results in this chapter use an interactive raytracer to render the scene, because it runs interactively on a large shared-memory machine, easily allowing access to large amounts of memory necessary for complicated caustics. Any renderer that can access the necessary data quickly and perform per-pixel operations could use these sampled data to compute caustic intensity.

4.3.1 Rendering Algorithm

Raytracing the scene proceeds normally until the determination of the color at a diffuse surface. At these surfaces, instead of just looking for direct illumination, the raytracer

performs lookups into the sampled data to determine if they are illuminated by a caustic. This process can be described algorithmically as follows:

1. Determine the direction \hat{L} from the center of the object O to the light. Locate the nearest light sample \hat{L}_i (where $\hat{L} \cdot \hat{L}_i$ is maximal). This volume stores the closest approximation to the caustic from the current light position. This step should be done only once per frame, since it is independent of the intersection point \mathbf{p} .
2. At each intersection point \mathbf{p} , find \mathbf{p} 's location in the volume sampled around O and look up the caustic contribution. Add this result to the direct lighting computed by the renderer.

4.3.2 Issues Rendering Caustic Data

Unfortunately, using a single light sample \hat{L}_i to render the caustic causes temporal coherence issues as objects move. This is due to differences in the caustic from one light sample to the next (see Figure 4.3). The popping can be reduced by combining the caustic from multiple light samples \hat{L}_i , \hat{L}_j , and \hat{L}_k (where $\hat{L} \cdot \hat{L}_i \geq \hat{L} \cdot \hat{L}_j \geq \hat{L} \cdot \hat{L}_k \geq \hat{L} \cdot \hat{L}_m, \forall m \notin \{i, j, k\}$). \hat{L}_i , \hat{L}_j , and \hat{L}_k form the three vertices of a spherical triangle on the unit sphere which includes \hat{L} (see Figure 4.6).

Combining three light samples using barycentric coordinates [15] eliminates popping between caustic samples but introduces a new problem—ghosting (see Figure 4.7). Ghosting happens because object O 's caustic can differ significantly between neighboring light samples, so blending data from \hat{L}_i , \hat{L}_j , and \hat{L}_k results in three separate faint caustics. Unfortunately, the best way to eliminate ghosting is to sample the caustic for more light directions. This significantly increases memory consumption.

Below, an approach which helps reduce ghosting for relatively smooth objects is described. This algorithm replaces step 2 from the rendering algorithm above:

- A. Compute the vector \vec{D}_p from O_{center} to \mathbf{p} .
- B. Find the barycentric coordinates of \hat{L} in the spherical triangle formed by \hat{L}_i , \hat{L}_j , and \hat{L}_k . This gives the relative contributions from each light sample (Figure 4.6).
- C. Compute the angles β_i , β_j , and β_k between \hat{L} and the three nearest sampled light directions \hat{L}_i , \hat{L}_j , and \hat{L}_k .

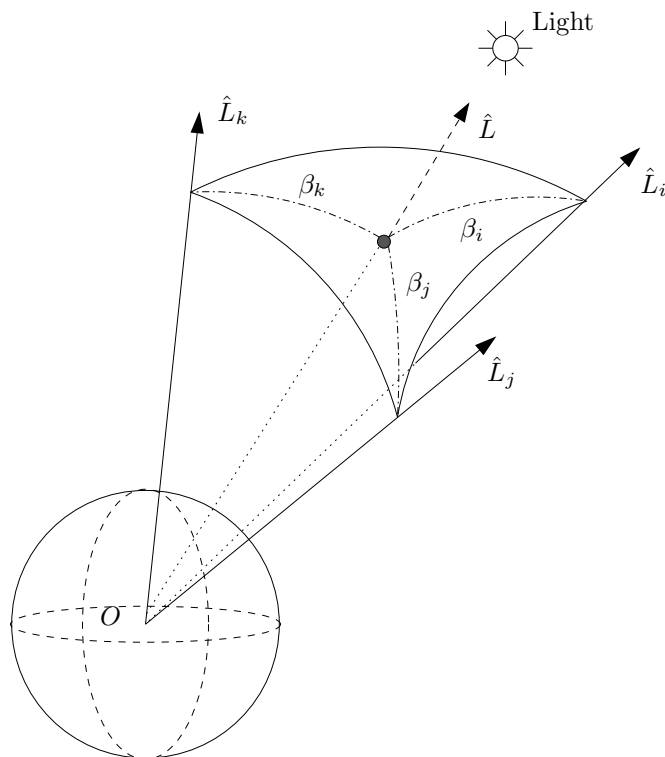


Figure 4.6. \hat{L} intersects the spherical triangle formed by \hat{L}_i , \hat{L}_j , and \hat{L}_k .

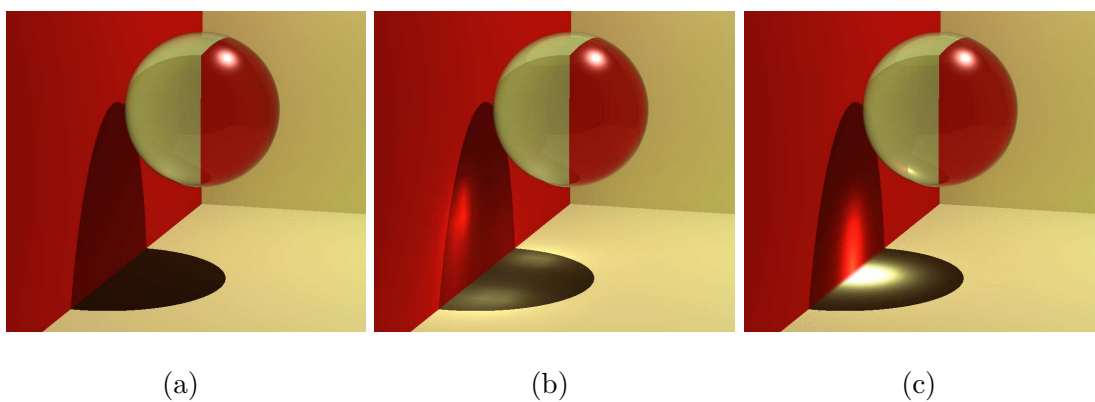


Figure 4.7. Ghosting happens when the caustic changes significantly between neighboring light samples \hat{L}_i , \hat{L}_j , and \hat{L}_k . Images (a) without caustics, (b) with ghost caustics, and (c) a correct caustic.

- D. Calculate rotation axes \vec{R}_i , \vec{R}_j , and \vec{R}_k by taking the cross product between \vec{L} and \vec{L}_i , \vec{L}_j , and \vec{L}_k , respectively.
- E. Rotate vector \vec{D}_p around the axis \vec{R}_i by angle β_i to find a new vector $\vec{D}_{p'_i}$. Similarly find $\vec{D}_{p'_j}$ and $\vec{D}_{p'_k}$ by rotating around \vec{R}_j and \vec{R}_k by angles β_j and β_k (Figure 4.8).
- F. Find the points \mathbf{p}'_i , \mathbf{p}'_j , and \mathbf{p}'_k . Where $\mathbf{p}'_i = O_{center} + \vec{D}_{p'_i}$.
- G. Perform caustic lookups as if \mathbf{p}'_i , \mathbf{p}'_j , and \mathbf{p}'_k were the intersection points (instead of \mathbf{p}). Weight the contributions from these points based on the barycentric coordinates computed in step B.

The process performs an interpolation between samples. Unfortunately, such an interpolation is not generally valid, as it assumes the caustic changes linearly in space for a linear change in light direction. For relatively smooth objects, like the sphere and bunny, such “interpolation” generally allows us to use fewer light samples. For objects such as the cube and prism that have sharp angles, this approach does not significantly reduce ghosting, so a large number of light samples are still required.

When using spherical harmonic coefficients, which essentially filter over the sampled light directions, this complicated rendering process can be avoided. Instead the caustic is computed by integrating the transfer function (stored at the samples as spherical harmonic coefficients) with the incident illumination, as described by Green [43], Sloan

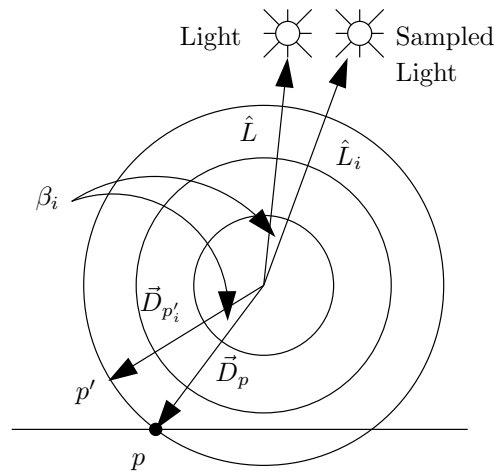


Figure 4.8. Alternative approach to caustic lookups. Find the cell to use in the weighted average by rotating \vec{D}_p around the axis \vec{R}_i (which points into the page at O_{center}) by angle β_i .

et al. [120], and Appendix B. Caustics rendered with spherical harmonics, however, tend to be very blurry.

4.4 Results

This approach was implemented on an interactive parallel raytracer running on an SGI Origin 3800 with thirty-two 400 MHz R12000 processors, a shared memory machine that easily holds the entire scene and caustic datasets in main memory. However, this approach is not limited to such applications. Any renderer that has per-pixel lighting control could implement the technique given enough memory. Existing systems (e.g., [42, 96, 133, 142, 138]) could easily incorporate such precomputed caustics to avoid the cost of reshooting photons each frame.

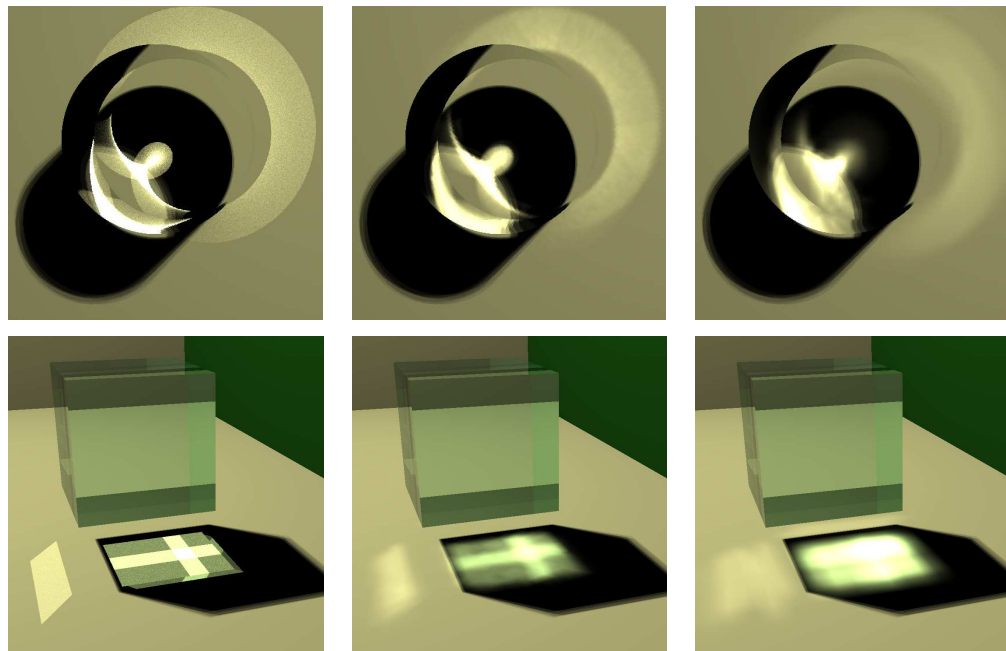
Table 4.1 contains timings for the images generated for Figures 4.1, 4.9, 4.10, and 4.11.

The lookups into the precomputed caustic data incur a 10–45% speed penalty when displaying caustics, depending on the relative costs of the lookups to the raytracing costs of the scene. The cost of the photon shooting preprocess ranges from 1.3 to 25 seconds per light sample, using a single 400 MHz R12000 CPU. Shooting photons for a photon map takes a similar amount of time, though additional overhead is needed to create the required kd-tree. Framerates are reported for a 360×360 window running on thirty 400 MHz R12000 processors.

Figures 4.9 and 4.10 compare a photon map with precomputed caustics using both the grid and concentric shell storage techniques. These comparisons show grids and shells requiring roughly the same amount of memory. The figures also show data compressed using 5th and 15th order spherical harmonics. Using the spherical harmonic representation provides advantages such as the ability to use area lights (see Figure 4.12), high

Table 4.1. Caustic rendering and precomputation times.

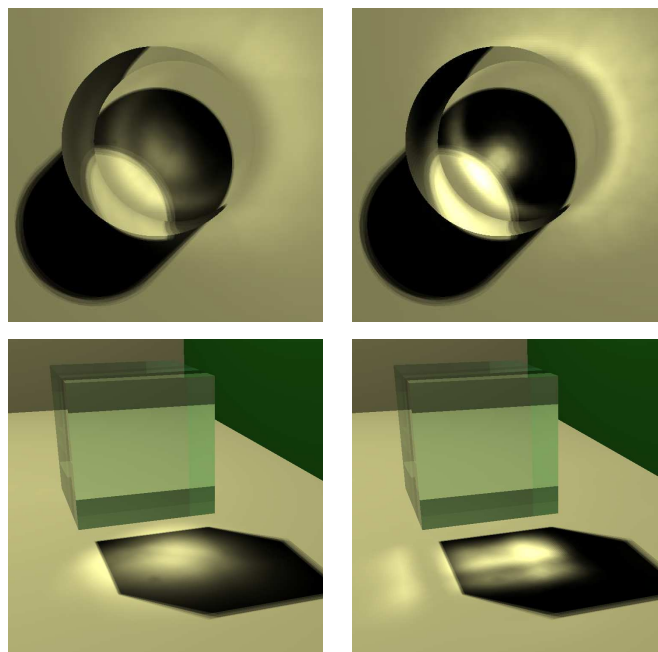
Object	Grid Caustics (fps)	Shell Caustics (fps)	MultiRes Caustics (fps)	No Caustics (fps)	5th Order Spherical Harmonics (fps)	Shoot Photons (per sample) (sec)
Sphere	15.2	17.3	15.0	26.9	8.1	1.7
Cube	12.1	12.6	10.8	20.2	6.1	2.4
Prism	12.7	13.2	11.0	20.3	6.5	2.0
Ring	9.3	9.5	8.8	12.9	5.2	1.3
Building	1.94	2.01	1.90	2.29	1.48	4.5
Bunny	2.16	2.30	2.25	2.55	1.80	25.0



(a)

(b)

(c)



(d)

(e)

Figure 4.9. Caustic rendering techniques on a metal ring and glass cube. Caustics from (a) a photon map, (b) the concentric shell approach, (c) the grid technique, (d) 5th order spherical harmonics, and (e) 15th order spherical harmonics.

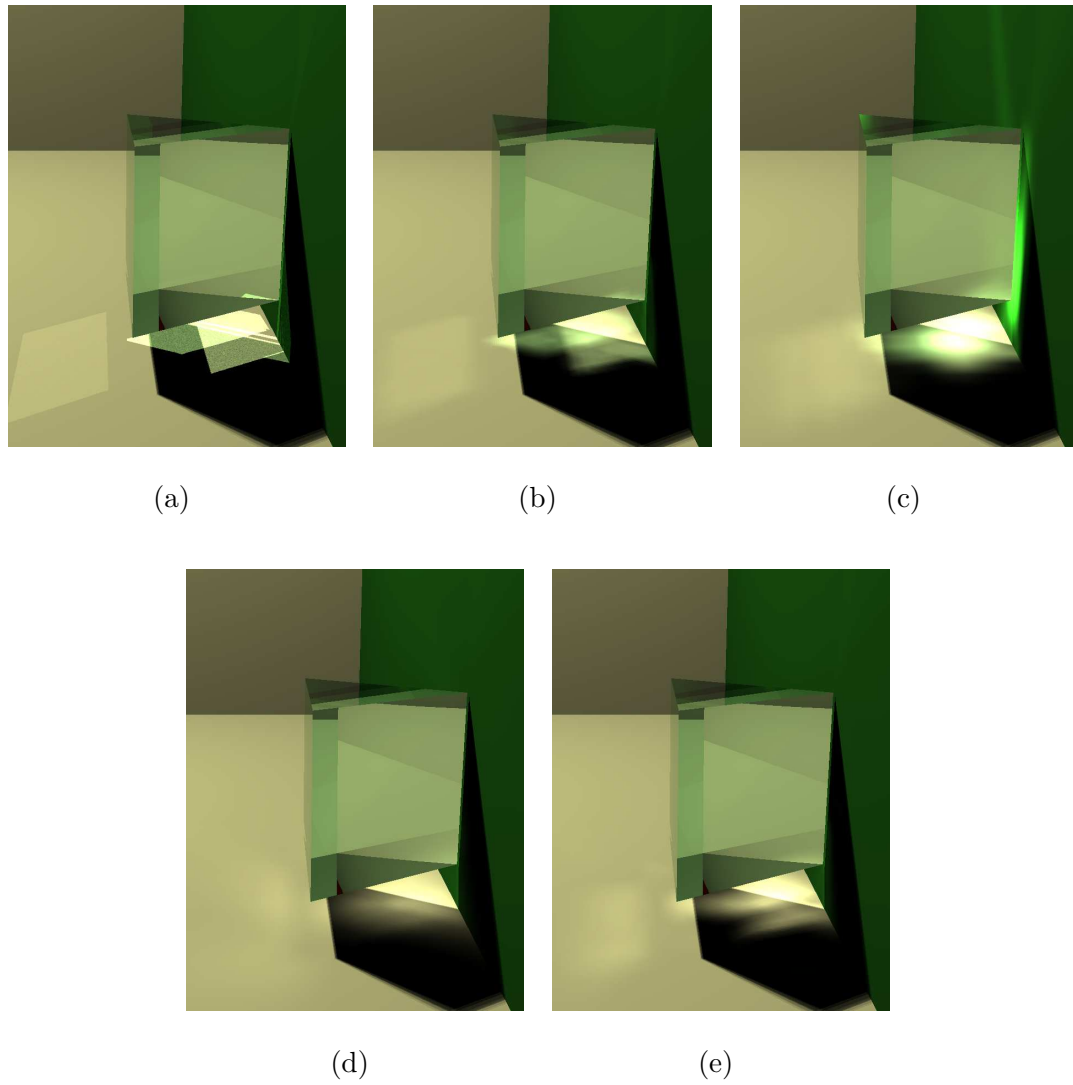


Figure 4.10. Caustic rendering techniques on a glass prism. Caustics from (a) a photon map, (b) the concentric shell approach, (c) the grid technique, (d) 5th order spherical harmonics, and (e) 15th order spherical harmonics.

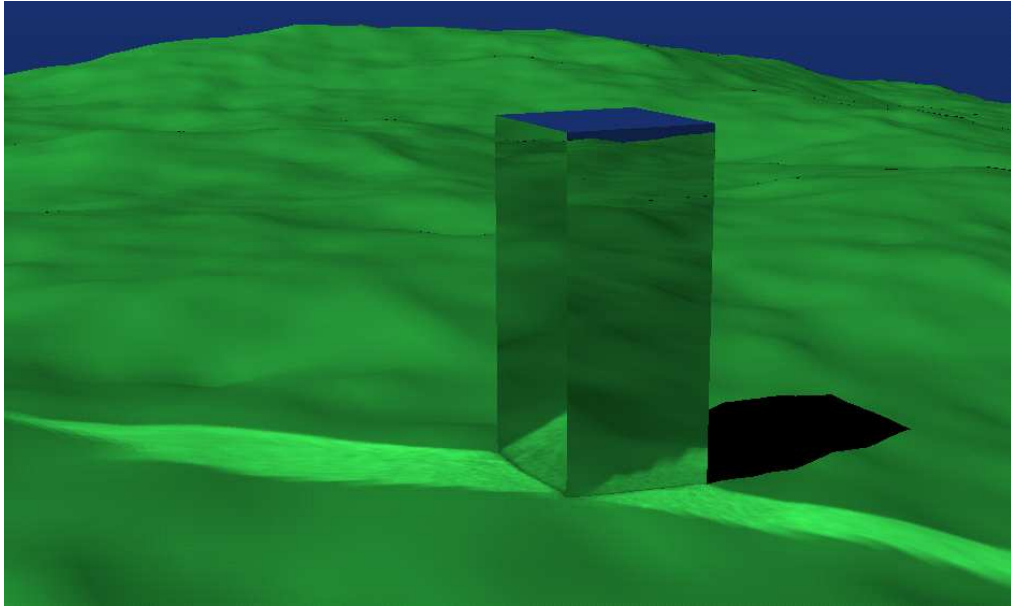


Figure 4.11. Casting caustics on complex objects. This “building” can dynamically cast caustics on surrounding terrain based on the sun’s position.

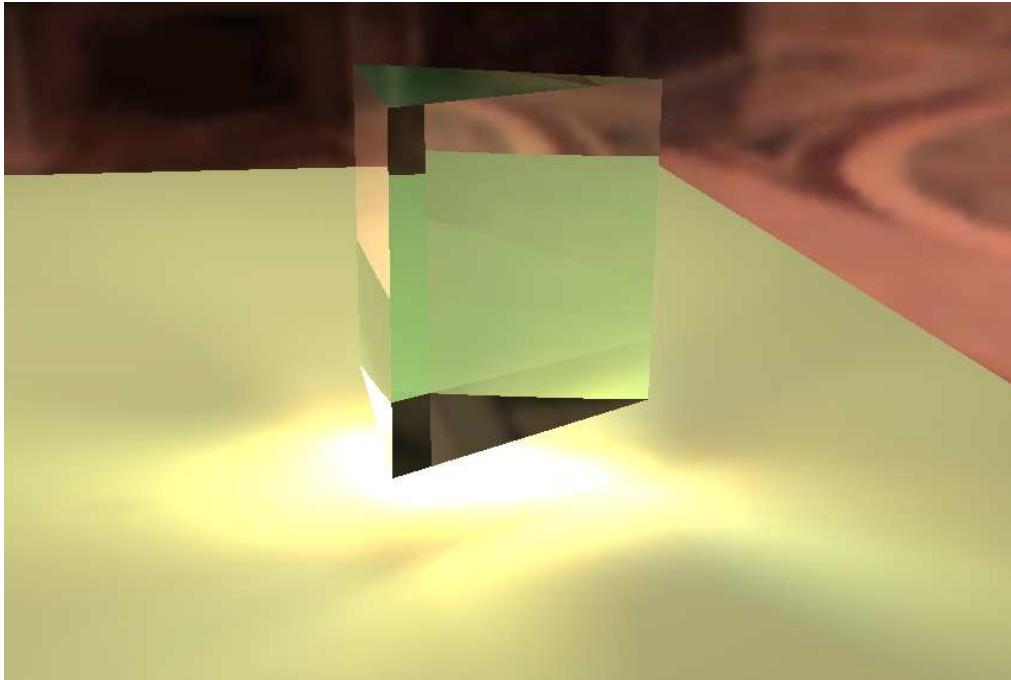


Figure 4.12. The caustic of a prism in St. Peter’s cathedral using 5th order spherical harmonics. Note there are no shadows in this image.

temporal coherence, and low memory consumption. For comparison, these fifth order representations use around 10 MB memory, about as much as the uncompressed data used for Figure 4.5(a). Since the number of coefficients increases quadratically with order, computation costs quickly become the bottleneck. All of these scenes run at less than one frame per second using fifteenth order spherical harmonics.

Figure 4.5 illustrates the effect of sampling density on memory consumption and caustic quality. For a relatively smooth object few light samples are necessary. The bunny (see Figure 4.1) needed only 162 light samples. For objects where the rotational alignment technique from Section 4.3.2 does not work well (like the cube and prism), up to 2500 light samples are necessary. Note that number of light samples does not affect framerate, assuming the data all fit into memory.

Obviously, with symmetric objects one need not sample the entire sphere of incoming light directions. For a sphere, a single light sample suffices. For the metallic ring, between 50 and 100 light samples are sufficient for good temporal coherence. Many common objects have symmetrical properties that could be used to simplify sampling.

4.5 Discussion

This chapter presented a novel technique for rendering approximate caustics interactively by localizing the problem to the vicinity of the focusing object. This approach avoids the recurring cost of photon shooting that other methods require to generate dynamic caustics. Because particle tracing is not necessary between frames, this technique can be applied to other interactive systems that cannot traditionally perform such computations (e.g., hardware based renderers). Additionally, the rendering costs of this method are independent of object complexity. Since caustics are rendered using table lookups, memory becomes the bottleneck, so a number of ways to sample, represent, and compress the data in memory were examined.

Storing a highly sampled caustic function in memory produced the best looking results. Unfortunately, the memory requirements make the technique difficult to use unless object symmetries or other simplifying conditions exist. Multiresolution approaches can significantly reduce memory overhead by storing densely sampled data only where necessary. In exchange lookups become more costly.

Spherical harmonic basis functions generally blur caustics extensively, and the results look unconvincing. However, memory requirements are modest enough to allow imple-

mentation on current graphics hardware. Higher order approximations improve results at the expense of additional coefficients, though this additional expense can quickly expand memory requirements beyond reach of graphics hardware.

Scenes that lend themselves well to this technique include outdoor scenes where the sun effectively acts as a constant directional lightsource. Such a scene requires a single light sample. Leveraging object symmetries also can reduce some of the memory burden. Many common objects have such symmetries, so these sampling techniques may be feasible for such objects.

This work has a number of limitations, including extensive memory requirements for general environments requiring the entire sampled space, poor realignment of neighboring samples, and inability to handle area lights without spherical harmonics. However, by tailoring the caustic representation to the application, these limitations can be overcome. Thus, the results presented in this chapter indicate that viable techniques exist for including specular effects as well as diffuse global illumination in interactive applications.

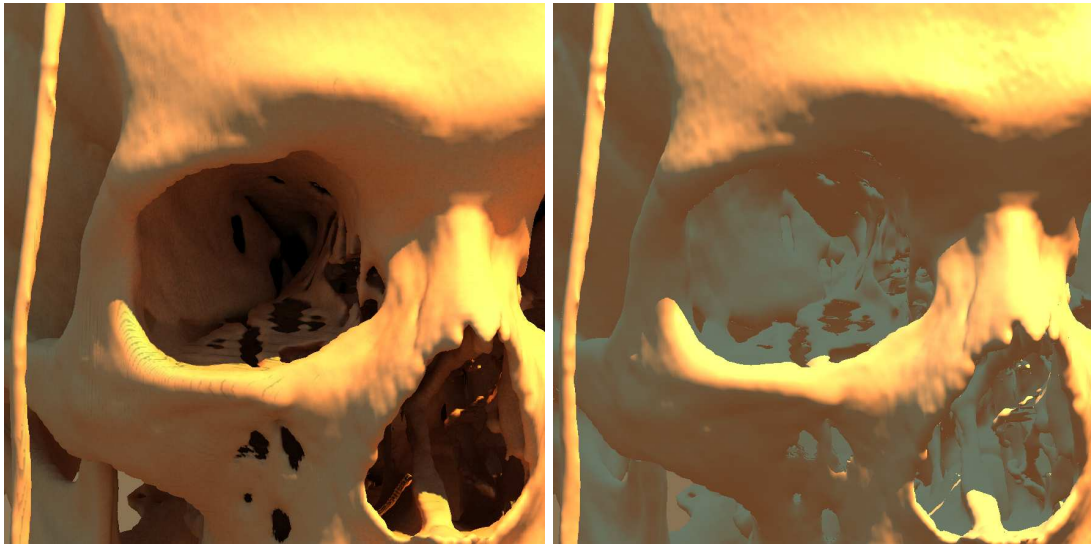
CHAPTER 5

INTERACTIVE RENDERING OF ISOSURFACES WITH GLOBAL ILLUMINATION

Isosurfaces, also known as implicit surfaces or level sets, are widely used in computer graphics and scientific visualization, whether to help model complex objects [112] or to reveal the structure of scalar-valued functions and medical imaging data [69]. Because both computational and acquired datasets tend to be large, only recently has interactive display and manipulation of surfaces with varying isovalues become feasible for full-resolution datasets [97]. In most interactive visualization systems, the rendering of isosurfaces is based on only local illumination models, such as Phong shading, perhaps coupled with simple shadows. For partially lit concave regions, these simple shading models fail to capture the subtle effects of interreflecting light and shadows. These regions are typically dominated by a local ambient term which provides no cues to environmental visibility or reflections from nearby surfaces. Figure 5.1 shows the details brought out by the approach introduced in this chapter, both in shadowed regions and those with high interreflections.

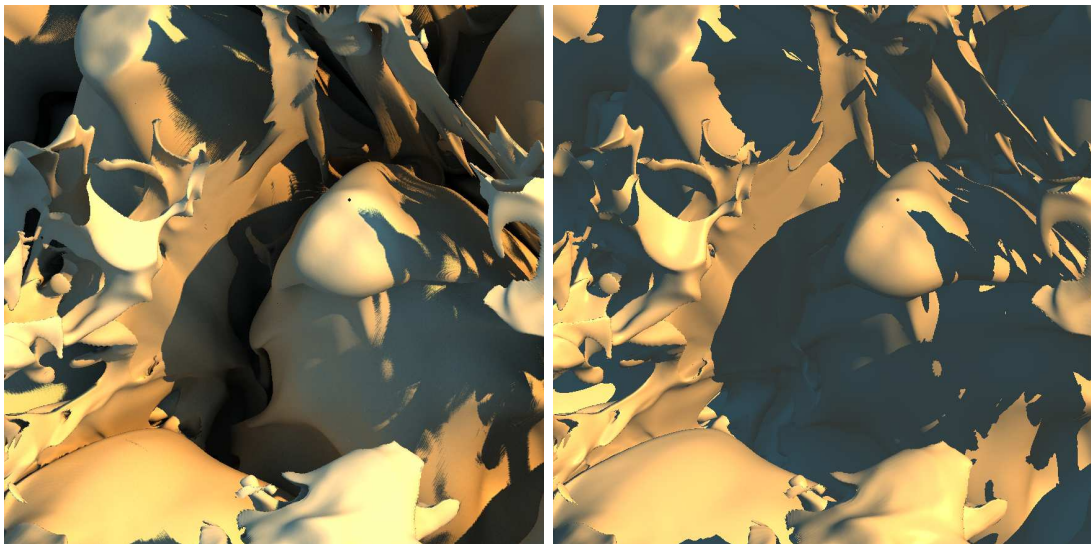
One usually thinks of “direct lighting” as coming from a small light source, but it can also come from extended light sources. In the extreme case the entire sphere of directions is a light source and “shadowing” occurs when not all of the background is visible at a point. This results in darkening for concavities, exploited as *accessibility shading* [87] and *obscurance shading* [155]. More recently, direct lighting from a uniform extended source has been applied to illuminating isosurfaces extracted from volumes to good effect [131].

This chapter extends the class of lighting effects for isosurfaces to include full global illumination from arbitrary light sources. The new method requires an expensive pre-process but does not greatly affect interactive performance, and can even speed it up since shadows can be precomputed and stored. This approach uses a conventional three-dimensional texture to encode volume illumination data. For static illumination and a static volume, a scalar texture encoding irradiance stores the necessary global



(a)

(b)



(c)

(d)

Figure 5.1. Comparison of (a,c) globally illuminated and (b,d) Phong shaded isosurfaces. Note the improvement in regions dominated by indirect lighting, particularly in the eye sockets (a,b) and the concavities in the simulation data (c,d).

illumination for all isosurfaces. For dynamic lights and complex materials, multiple values are used per texel, as in Sloan et al. [120]. In either case, rendering interpolates between neighboring texels to approximate the global illumination on the correct isosurface.

The next section introduces some volume rendering terminology and describes the illumination models for display. Section 5.2 gives an overview of the new illumination technique, and Section 5.3 describes the algorithm in greater detail. Section 5.4 discusses the results.

5.1 Background

Rendering images of isosurfaces can be accomplished by first extracting some surface representation from the underlying data followed by some method of shading the isosurface. Alternatively, visualizing isosurfaces with direct volume rendering requires an appropriate transfer function and a shading model.

In practice, many volume datasets are rectilinearly sampled on a three-dimensional lattice, and can be represented as a function ρ defined at lattice points \mathbf{x}_i . Some interpolation method defines $\rho(\mathbf{x})$ for other points \mathbf{x} not on the lattice. Other datasets are sampled on a tetrahedral lattice with an associated interpolation function. Analytical definitions are also possible for $\rho(\mathbf{x})$, often arising out of mathematical applications. Such analytical representations can easily be sampled on either a rectilinear or tetrahedral lattice.

Given a sampled dataset $\rho(\mathbf{x}_i)$, the marching cubes algorithm [79] extracts explicit polygons approximating an isosurface $I(\rho_{iso})$ with isovalue ρ_{iso} , where $I(\rho_{iso}) = \{\mathbf{x} \mid \rho(\mathbf{x}) = \rho_{iso}\}$. Various improvements make this technique faster and more robust, but these improvements still generate explicit polygonal representations of the surface. Raytracing and volume rendering provide an alternate method of displaying isosurfaces, which need not construct and store a polygonal representation [76, 97]. Once an isosurface has been identified, standard illumination models can be applied to help visualize the data.

Commonly, extracted isosurfaces are shaded using the Phong model [102] and variations using similar ambient, diffuse, and specular components. Such techniques give poor depth and proximity cues, as they rely on purely local information. Illumination techniques for direct volume rendering, such as those surveyed in Max [84], allow translucency and scattering along the viewing ray and shadow rays, but they fail to allow area lights and are not interactive. Sobierajski and Kaufman [124] apply global illumination

to volume datasets, but they shade at runtime, so few effects can be incorporated while maintaining interactivity.

Several techniques have been proposed to interactively shade volumes with global lighting. The Irradiance Volume [44] samples the irradiance contribution from a scene, allowing objects moving around the scene to be shaded by static environment illumination. However, objects placed in the Irradiance Volume cannot interact with themselves, which is important for correct global illumination of isosurfaces. Precomputed radiance transfer techniques [90, 119, 120] can be used to shadow or cast caustics on nearby objects by sampling transfer functions in a volume around the occluder. Unfortunately, these techniques do not allow dynamic changes to object geometry, which is important when exploring the isosurfaces of volume datasets. Kniss et al. [73] describe an interactive volume illumination model that captures shadowing and forward scattering through translucent materials. However, this method does not allow for arbitrary interreflections and thus does not greatly improve isosurface visualization. The *vicinity shading* technique of Stewart [131] encodes direct illumination from a large uniform light in a three-dimensional texture and allows its addition to standard local shading models while interactively changing the displayed surface. However, this method provides an approach for only direct illumination and does not incorporate indirect illumination.

5.2 Overview

A brute-force approach to globally illuminating an isosurface would compute illumination at every point visible from the eye. Figure 5.2 shows how a Monte Carlo path tracing technique would perform this computation. Obviously, performing such computations on a per-pixel basis quickly becomes cost prohibitive, so caching techniques [146] are usually preferable. Many existing techniques cache radiance [10], irradiance [44], or more complex transfer functions [90, 106, 120] to speed illumination computations.

In volume visualization, users commonly change the displayed isovalue, thereby changing the isosurface, to view different structures in the volume. Most illumination caching techniques are object specific, so as the surface changes new illumination samples must be computed. This chapter introduces a technique that stores either irradiance or more complex transfer functions in a three-dimensional texture coupled with the volume. Each texel t corresponds to some point \mathbf{x}_t in the volume. The process is broken into two steps. During the computation step, illumination values can be computed using any

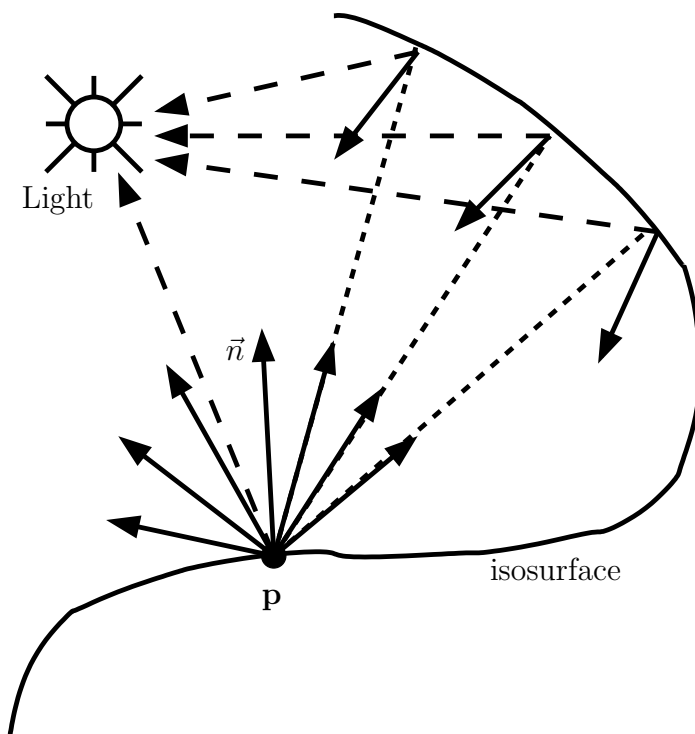


Figure 5.2. Computing the irradiance at point \mathbf{p} involves sending a shadow ray and multiple reflection rays. Reflection rays either hit the background or another part of the isosurface, in which case rays are recursively generated.

standard global illumination technique. For each texel t , extract the isosurface $I(\rho(\mathbf{x}_t))$ running through \mathbf{x}_t . Using this isosurface, compute the global illumination at point \mathbf{x}_t via standard approaches and store the result in texel t . Figure 5.3 shows how this works for four adjacent samples using a Monte Carlo sampling scheme. When rendering, interpolate between cached texels to the correct isosurface, allowing for interactive display of arbitrary isosurfaces.

As with most illumination caching techniques, the rationale behind this approach is that global illumination generally changes slowly for varying spatial location. Here this assumption applies in two ways: illumination should change gradually over a surface and illumination should change gradually with changing isosurfaces.

One situation exists where this approximation obviously breaks down—hard shadows. Hard shadows involve a very visible discontinuity in the direct illumination. As shown in Figure 5.3, each sample in the illumination lattice is potentially computed on a different isosurface. In regions where a shadow discontinuity exists, some samples will be in shadow and others will be illuminated. Using an interpolation scheme to compute the illumination

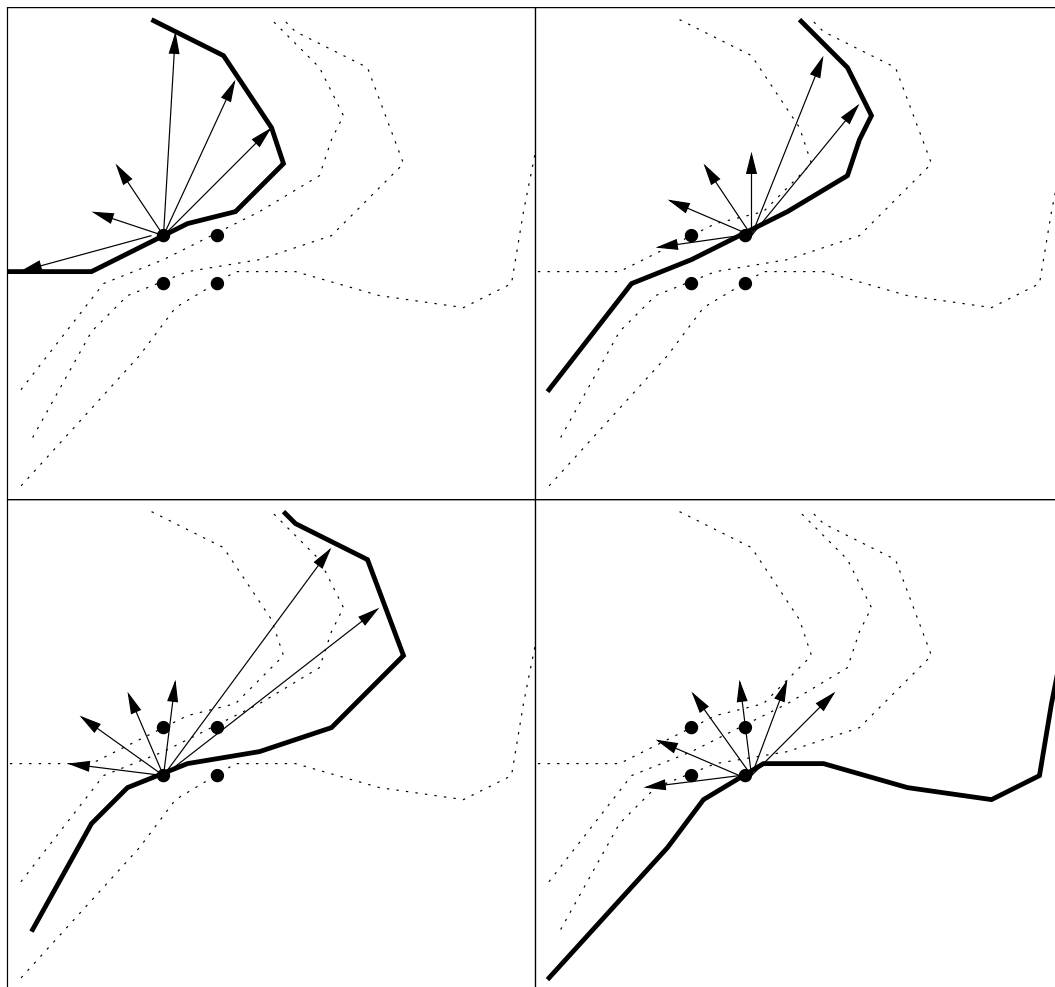


Figure 5.3. The global illumination at each texel t is computed using standard techniques based on the isosurface $I(\rho(\mathbf{x}_t))$ through the sample.

results in a partially shadowed point between samples. Thus for a static isosurface, results near shadow edges will be blurred, similar to the effect achieved with percentage closer filtering [109].

Since dynamically changing the rendered isosurface is desirable, the effect of such changes on shadow boundaries must also be considered. As the displayed isosurface changes, the interpolated illumination value on the surface changes with distance from illumination samples, just as the illumination varies over a single isosurface. Thus, faint shadows may exist when there is no apparent occluder or small occluders may cast no shadow. The effect is that shadows will “fade” in and out as occluders appear and disappear. Examples of these effects can be seen in Figure 5.4. The scene is illuminated

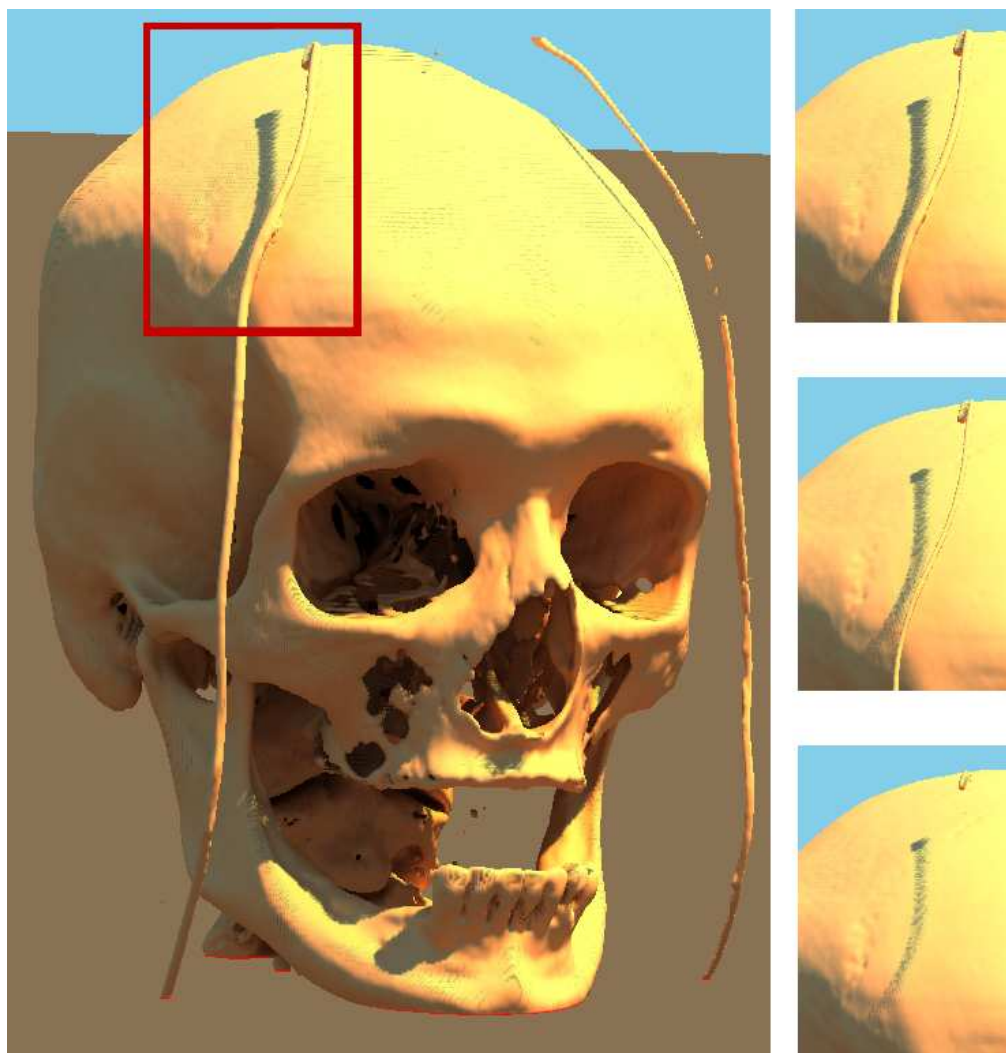


Figure 5.4. The Visible Female’s skull globally illuminated using the new technique. The right images show how the cord’s shadow fades out with increasing isovalues.

by a blue and brown environment with a yellow point light source. The shadows are blurred slightly, and as the isosurface changes the cord fades out before its shadow.

Note that because sharp discontinuities in direct illumination are most visible, hard shadow are a worst-case scenario. For soft shadows or indirect illumination the perceived effects are less pronounced, so this approximation of a smoothly changing illumination function becomes more accurate. Artifacts similar to those in Figure 5.4 may still occur, but they will be less noticeable.

The artifacts that occur with changing isovalues arise from approximating the non-linear global illumination function using simple trilinear interpolation. This approxima-

tion is what causes the “fading” of shadows and the faint banding seen in the results.

This assumption occasionally causes problems, but the proposed technique provides significantly more locality information than local models, especially in concavities and dark shadows where ambient terms either provide little or conflicting information. Additionally, since shadows are included in the representation, they require no additional computation. In fact, this technique renders faster than simple Phong and Lambertian models when including hard shadows.

5.3 Algorithm

This technique has two stages: illumination computation and interactive rendering. A simplistic approach would perform all the computations as a preprocess before rendering. As this can require significant time and not all illumination data may be required, it is possible to lazily perform computations as needed, assuming the display of some uncomputed illumination is acceptable until computations are complete.

5.3.1 Illumination Computation

Each sample in the illumination lattice stores some representation of the global illumination at that point. This illumination is described by the rendering equation (from Section 1.2.3), without the emission term:

$$L(\mathbf{x}_t, \vec{\omega}_{out}) = \int_{\Omega} f_r(\mathbf{x}_t, \vec{\omega}_{out}, \vec{\omega}_{in}) L(\mathbf{x}_t, \vec{\omega}_{in}) \cos \theta_{in} d\vec{\omega}_{in},$$

where \mathbf{x}_t is the location of the illumination texel t with normal \vec{n}_t , $\vec{\omega}_{out}$ is the exitant direction, $\vec{\omega}_{in}$ is the incident direction varying over the hemisphere Ω , and f_r is the BRDF. Note that $\cos \theta_{in}$ is equivalent to $\vec{\omega}_{in} \cdot \vec{n}_t$, which is used in the rest of this chapter.

Depending on an application’s required materials and illumination this equation and the representation stored in the illumination texture can be varied to reduce computation time and storage space. For a simple diffuse surface with fixed lighting, a single irradiance value is sufficient at each lattice point. In this case, the rendering equation can be rewritten as:

$$L(\mathbf{x}_t) = f_r(\mathbf{x}_t) \int_{\Omega} L(\mathbf{x}_t, \vec{\omega}_{in}) (\vec{\omega}_{in} \cdot \vec{n}_t) d\vec{\omega}_{in} = \frac{R(\mathbf{x}_t) E(\mathbf{x}_t)}{\pi}. \quad (5.1)$$

Here the diffuse BRDF has no dependency on $\vec{\omega}_{in}$. It can be removed from the integral and is then equivalent to the surface albedo $R(\mathbf{x}_t)$ divided by π . The remainder of the

integral is the irradiance at point \mathbf{x}_t , $E(\mathbf{x}_t)$. Storing $E(\mathbf{x}_t)$ in a texture allows for easy illumination during rendering, as per Equation 5.1.

The simplest way to compute the irradiance at each sample point \mathbf{x}_t uses naive Monte Carlo pathtracing. Using N random vectors, \vec{v}_j , sampled over the hemisphere Ω , the irradiance is approximated:

$$E(\mathbf{x}_t) = \frac{1}{N} \sum_{j=1}^N L(\mathbf{x}_t, \vec{v}_j). \quad (5.2)$$

Using this equation, compute the irradiance at every point as shown in Figure 5.5.

Explicitly extracting different isosurfaces for each sample is quite costly. To avoid this cost, a raytracer performs intersections with the trilinear surface analytically [98]. Unfortunately, trilinear techniques generate noisy surfaces and normals, which can significantly impact the quality of the computed global illumination (see Figure 5.6). Rather than directly computing normals from the analytical trilinear surface or using a simple finite difference gradient, a smoothed normal defined by a tricubic B-spline kernel applied to the gradient over a $4 \times 4 \times 4$ voxel region gives better results. Smoothing normals and slightly offsetting \mathbf{x}_t in the normal direction during illumination computations significantly reduces this microscopic self-shadowing noise. Note the global illumination artifacts seen in Figure 5.6 using gradient normals occur on both microscopic and macroscopic scales. Noise occurs on the microscopic scale due to aliasing on the trilinear surface. Artifacts occur on the macroscopic scale when the volumetric dataset and the illumination volume have different resolutions. Visible bands occur where voxels from the two volumes align, as can be seen in Figure 5.6(d).

For more complex effects such as dynamic illumination or nondiffuse material BRDFs, a simple irradiance value will not suffice, and a more complex representation of the

```

for all  $\mathbf{x}_t$  in illumination lattice do
  compute isovalue  $\rho(\mathbf{x}_t)$ 
  compute isosurface normal  $\vec{n}_t$ 
  sample hemisphere  $\Omega$  defined by  $\vec{n}_t$ 
  for all samples  $\vec{v}_i \in \Omega$  do
    compute illumination at  $\mathbf{x}_t$  in direction  $\vec{v}_i$  using isosurface with isovalue  $\rho(\mathbf{x}_t)$ 
  end for
  compute irradiance at  $\mathbf{x}_t$  using equation 5.2.
end for

```

Figure 5.5. Pseudocode to compute irradiance at samples in the illumination lattice.

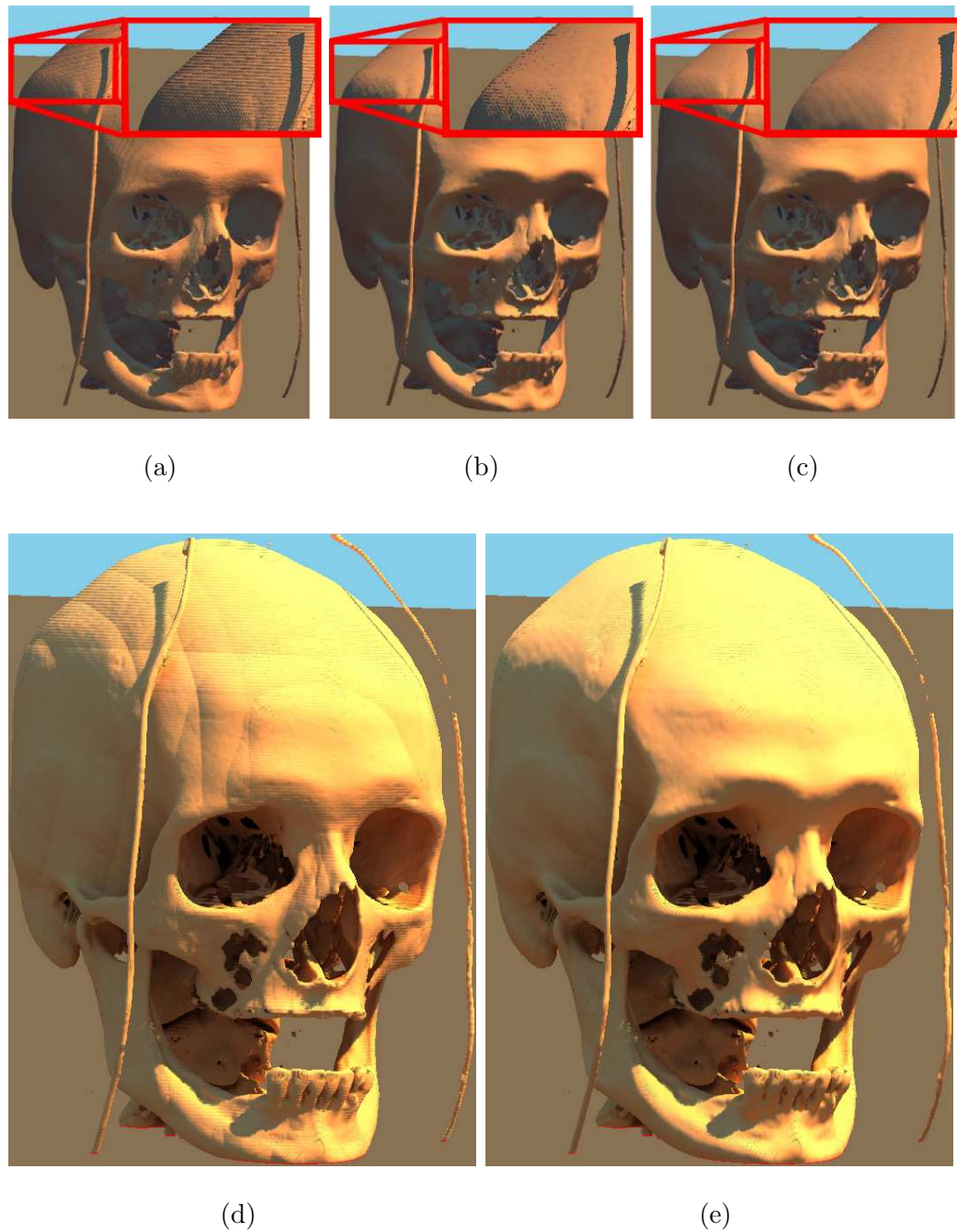


Figure 5.6. An isosurface from the Visible Female’s head extracted using analytical intersection of the trilinear surface. Direct illumination from a point light using (a) gradient normals, (b) tricubic B-spline smoothed normals, and (c) offset surface with smoothed normals. Four bounce global illumination using (d) gradient normals and (e) offset surface with smoothed normals.

illumination must be computed. Choosing to use spherical harmonic (SH) basis functions to store more complex illumination efficiently represents low frequency lighting. As diffuse global illumination tends to vary smoothly over space, such a representation makes sense. Spherical harmonics allow for dynamically changing illumination as well as quick integration during rendering, using a simple dot product or matrix multiply operation.

Assuming a diffuse material, incident illumination from a distant environment $L_\infty(\vec{\omega}_{in})$ invariant over \mathbf{x} , and a visibility function $V(\mathbf{x}_t, \vec{\omega}_{in})$, the rendering equation can be rewritten as:

$$L(\mathbf{x}_t) = f_r(\mathbf{x}_t) \int_{\Omega} \left[L_\infty(\vec{\omega}_{in}) V(\mathbf{x}_t, \vec{\omega}_{in}) (\vec{\omega}_{in} \cdot \vec{n}_t) + L(\mathbf{x}_t^{\vec{\omega}_{in}}) (1 - V(\mathbf{x}_t, \vec{\omega}_{in})) \right] d\vec{\omega}_{in}. \quad (5.3)$$

Note $\mathbf{x}_t^{\vec{\omega}_{in}}$ is the point occluding \mathbf{x}_t in direction $\vec{\omega}_{in}$. As the incident illumination is assumed constant over the volume, it can be factored out of the recursive integrals when using the SH basis, leaving a geometry term whose coefficients can be computed numerically using Monte Carlo techniques. Green [43] clearly explains this process in great detail. Every point in the illumination texture stores SH coefficients of this geometry term.

Similar SH values can be computed and stored at voxels for more complex materials including glossy or transparent effects, as described in Sloan et al. [120, 119]. Additionally other bases, like wavelets, could be used to represent the global illumination in the volume, especially if higher frequency effects are desired.

5.3.2 Interactive Rendering

After computing the illumination samples, rendering is straightforward. At every visible point on the displayed isosurface, first index into the illumination texture to find the eight nearest neighbors. Afterwards, interpolate the coefficients stored in the texture, and use the interpolated coefficients for rendering.

When using an irradiance texture, simply use Equation 5.1 to compute the illumination based on the stored irradiance and the albedo. With the spherical harmonic representation, interpolate the stored spherical harmonic geometry coefficients and perform a vector dot product with the environmental lighting coefficients.

A higher order interpolation [83] scheme over nearby neighbors was expected to generate better smooth illumination over complex isosurfaces. Interestingly, simple trilinear interpolation of stored coefficients proved sufficient. More complex interpolation schemes gave equivalent or even worse results, as shown in Figure 5.7. Methods with larger kernels

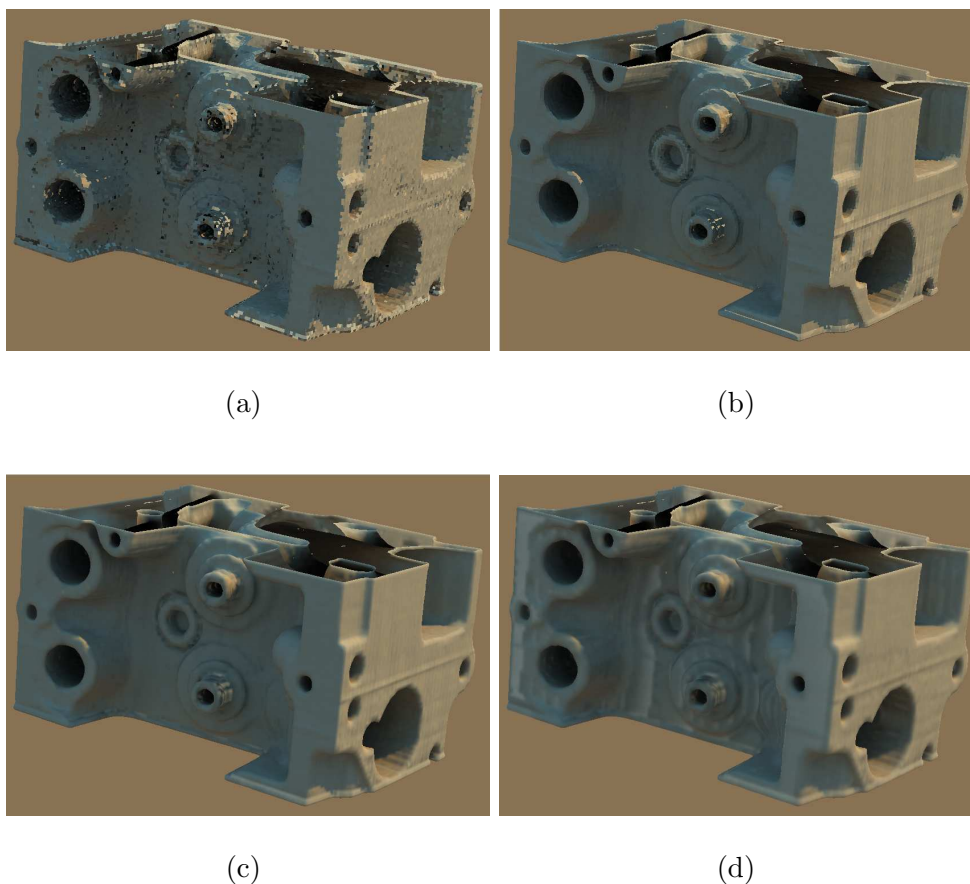


Figure 5.7. Approaches to interpolating between illumination samples. Engine block illuminated using (a) the illumination sample with closest isovalue, (b) the nearest illumination sample, (c) a trilinearly interpolated value, or (d) a value computed with a tricubic B-Spline kernel.

generally gave worse results due to the increased likelihood of interpolating samples from widely different isosurfaces.

5.4 Results

Several different approaches were used to implement this technique. First, a Monte Carlo pathtracer computed the illumination at texels throughout the volume. Utilizing the precomputations in an interactive raytracer allows dynamic changes to the visualized surface and illumination. An extension to the interactive raytracer allowed computation of illumination lazily, avoiding computations for isosurfaces never seen. Finally, importing the illumination texture into an OpenGL visualization program allows interactive

rendering of global illumination on a single PC.

The interactive raytracer runs in parallel on an SGI Origin 3800 with sixty-four 600 MHz R14000 processors. This is a shared memory machine with 32 GB of memory, allowing for easy access to large volume datasets and illumination textures. Large SGIs are uncommon, but users generating and interactively displaying large volume datasets typically have access to similarly powerful machines (or clusters [27]) which could apply this technique. The OpenGL implementation runs on a Dell Precision 450 with 1 GB memory and an Intel Xeon at 2.66 GHz. The graphics card is a GeForce FX 5900 with 256 MB memory. The code utilizes only simple fragment shaders, so older cards should suffice, but the increased graphics card memory facilitates visualizing bigger volumes.

Computing global illumination values for every texel in a volume can be quite expensive, whether computing simple irradiances or sets of spherical harmonic coefficients. Table 5.1 shows illumination computation timings for the volume shown in Figure 5.8. Times are shown for computing the entire texture as well as for the single views shown in Figure 5.8. The prototype uses naive, unoptimized Monte Carlo pathtracing, on thirty 400 MHz R12000 CPUs, for precomputation. More intelligent algorithms would significantly reduce these precomputation times.

For volumes with few interesting surfaces such as the engine block, computing illumination on the fly may be preferential to a long precomputation, as global illumination samples reside near displayed isosurfaces. Samples elsewhere can remain uncomputed. At a 512×512 resolution, computing a single irradiance for each sample takes a few seconds per viewpoint using sixty 600 MHz R14000 CPUs. Densely sampled illumination textures and complex environmental lighting require longer computations, as shown in Table 5.1. In either case lazy computation maintains interactivity, so viewpoint and isovalue can be changed during computation.

Table 5.1. Illumination computation timings for images from Figure 5.8.

	100	625	2500	10000
Sample type	samples	samples	samples	samples
	per voxel	per voxel	per voxel	per voxel
Spherical harmonics (single image)	0.33 min	2.63 min	10.6 min	48.2 min
Spherical harmonics (full texture)	8.47 min	52.8 min	210 min	853 min
Irradiance samples (single image)	0.95 min	5.80 min	23.7 min	98.3 min
Irradiance samples (full texture)	18.2 min	113 min	450 min	1806 min
Pathtraced (single image)	0.73 min	4.51 min	18.0 min	72.1 min

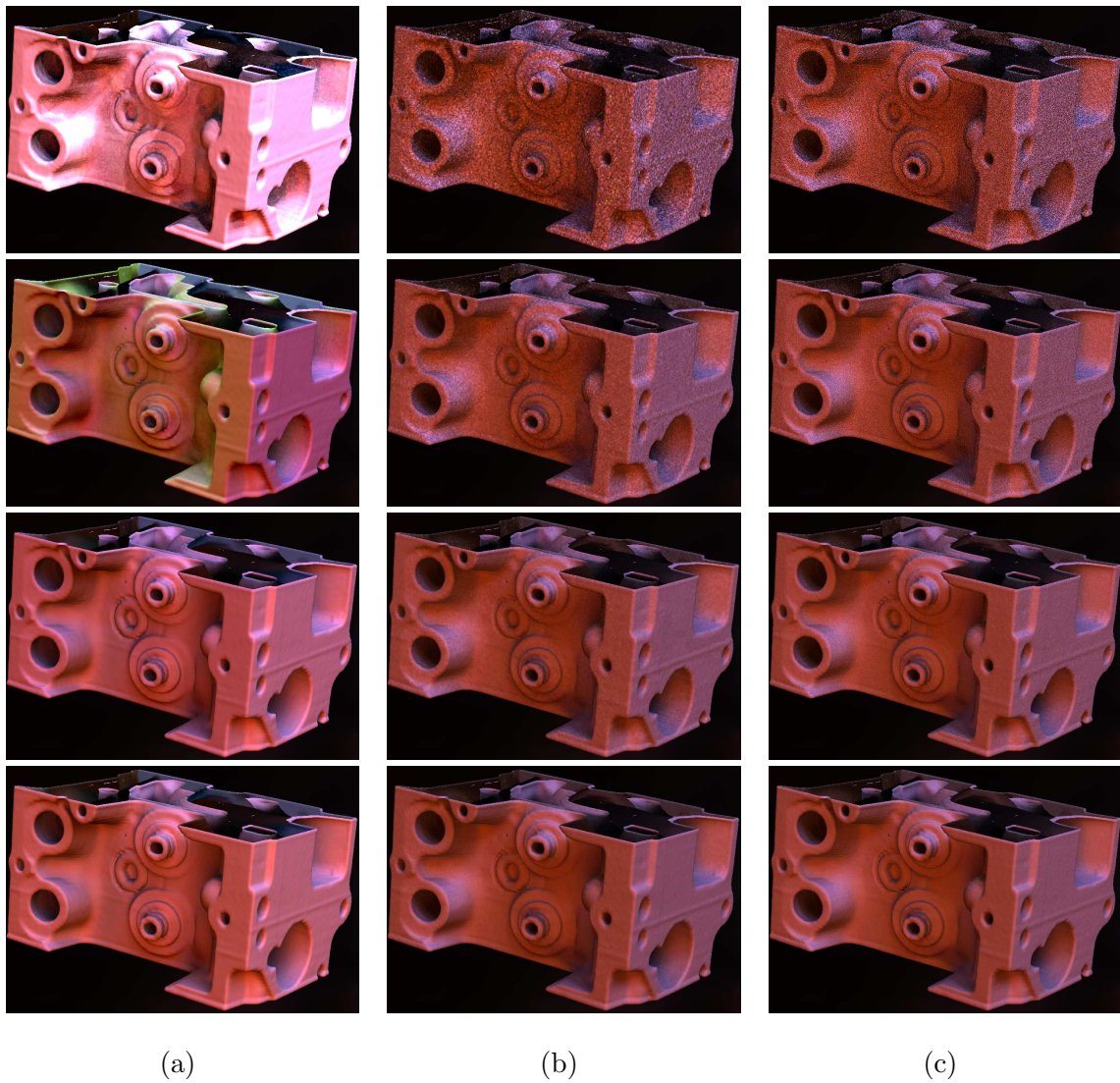


Figure 5.8. The engine block illuminated by the Grace cathedral lightprobe. Spherical harmonic samples (a) converge faster than Monte Carlo irradiance samples (b) or Monte Carlo pathtracing (c) due to the filtered low frequency environment. From top to bottom: 100, 625, 2500, and 10000 samples.

Precomputation is slow, but it need be done only once. Using the resulting illumination is simple and quicker than most lighting models used for visualization. Table 5.2 compares framerates using Phong and Lambertian materials with this technique. Timings use the interactive raytraced implementation on either thirty or sixty 600 MHz R14000 CPUs with image resolutions of 512×512 . Notice that rendering from either spherical harmonic coefficients or a single irradiance sample is faster than simple shading with hard shadows. Yet both these techniques include shadows along with other global illumination effects.

Table 5.2 also shows the memory overhead for this technique. The irradiance sample requires one RGB triplet per voxel, stored as one byte per color channel. Using the same resolution as the volume dataset requires as much as three times more memory as simply storing the volumetric data. The spherical harmonic representation uses no compression, so a fifth order representation uses 25 floating-point coefficients per channel, or two orders of magnitude more memory. Using compression techniques from Sloan et al. [119] would help reduce memory usage.

Simulation data, like the Richtmyer-Meshkov instability dataset shown in Figures 5.9, 5.10, and 5.11, also benefits from global illumination. Often such data are confusing so shadows and diffuse interreflections can give a sense of scale and depth lacking in Phong and Lambertian renderings. Figures 5.9, 5.10, and 5.11 compare the new technique to vicinity shading, Phong, and Lambertian with and without shadows. The Phong and Lambertian images use a varying ambient component based on the surface normal. Figures 5.10 and 5.11 also compare with a local approach that adds distance information using OpenGL-style fog.

Vicinity shading provides better results than Phong or Lambertian models, but incident illumination must be constant over the environment, such as on a cloudy day. Vicinity shading turns out to be a special case of a full global illumination solution. By

Table 5.2. Comparison of framerates and memory consumption for Figure 5.8.

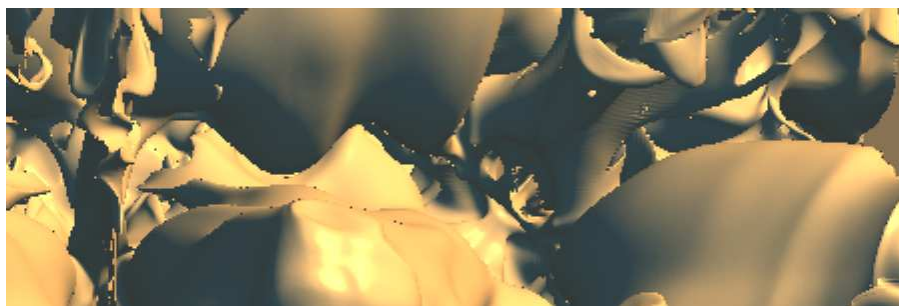
Material Type	Frames per second (on 30 CPUs)	Frames per second (on 60 CPUs)	Extra memory used (in MB)
Diffuse, No Shadows	17.0	33.1	0
Diffuse, With Shadows	8.75	17.3	0
Phong, With Shadows	8.60	17.0	0
Irradiance Samples	15.6	30.5	9.75
Spherical Harmonics	11.7	21.7	975



(a)



(b)



(c)

Figure 5.9. An enlarged portion of the Richtmyer-Meshkov dataset shown in Figure 5.11. These images enlarge a crevice in the upper right corner of images from the right column using (a) the new approach, (b) vicinity shading, and (c) Phong with varying ambient component.

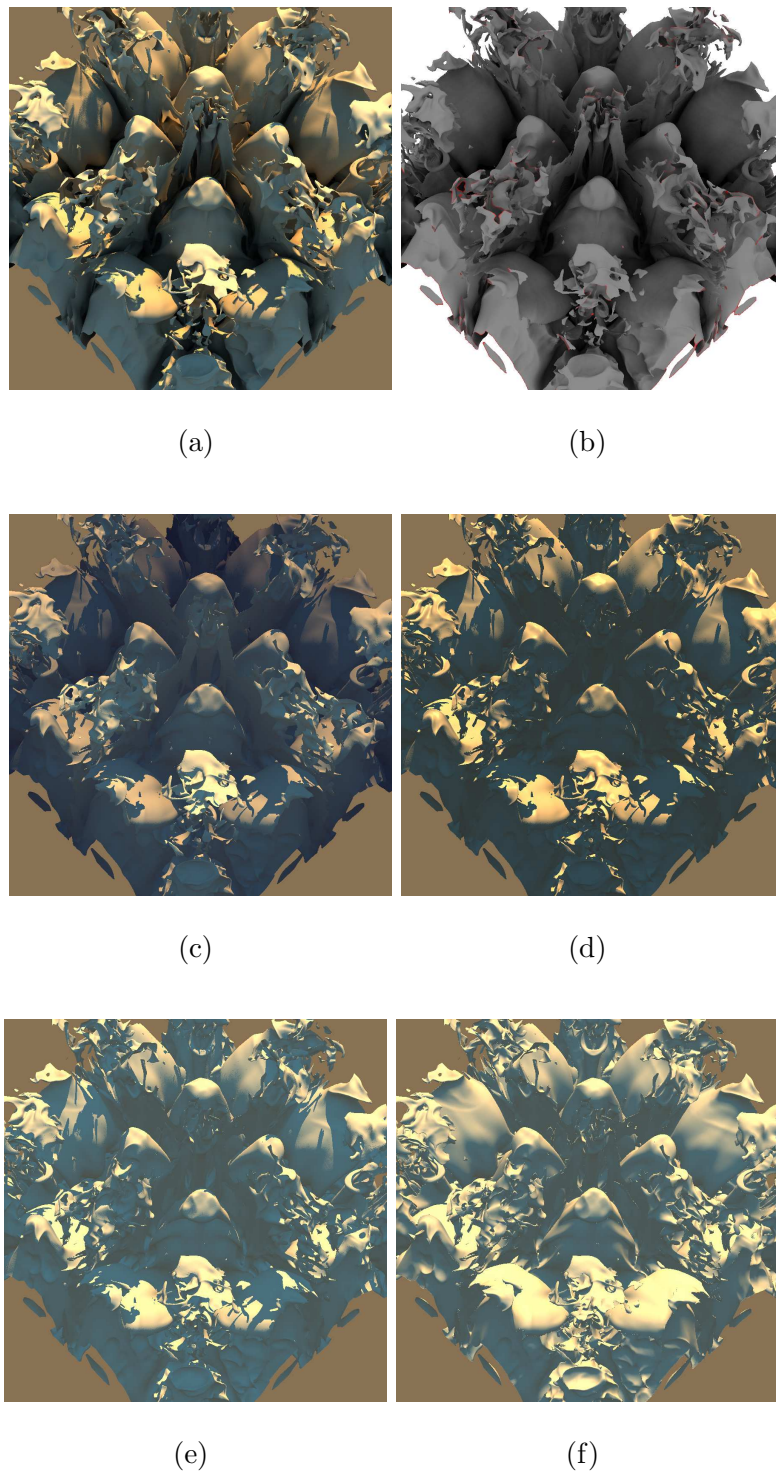


Figure 5.10. A Richtmyer-Meshkov instability simulation under various illumination. A view using (a) the new technique, (b) vicinity shading, (c) Lambertian with fog, (d) Phong with varying ambient, (e) Lambertian with varying ambient, and (f) Lambertian without shadows.

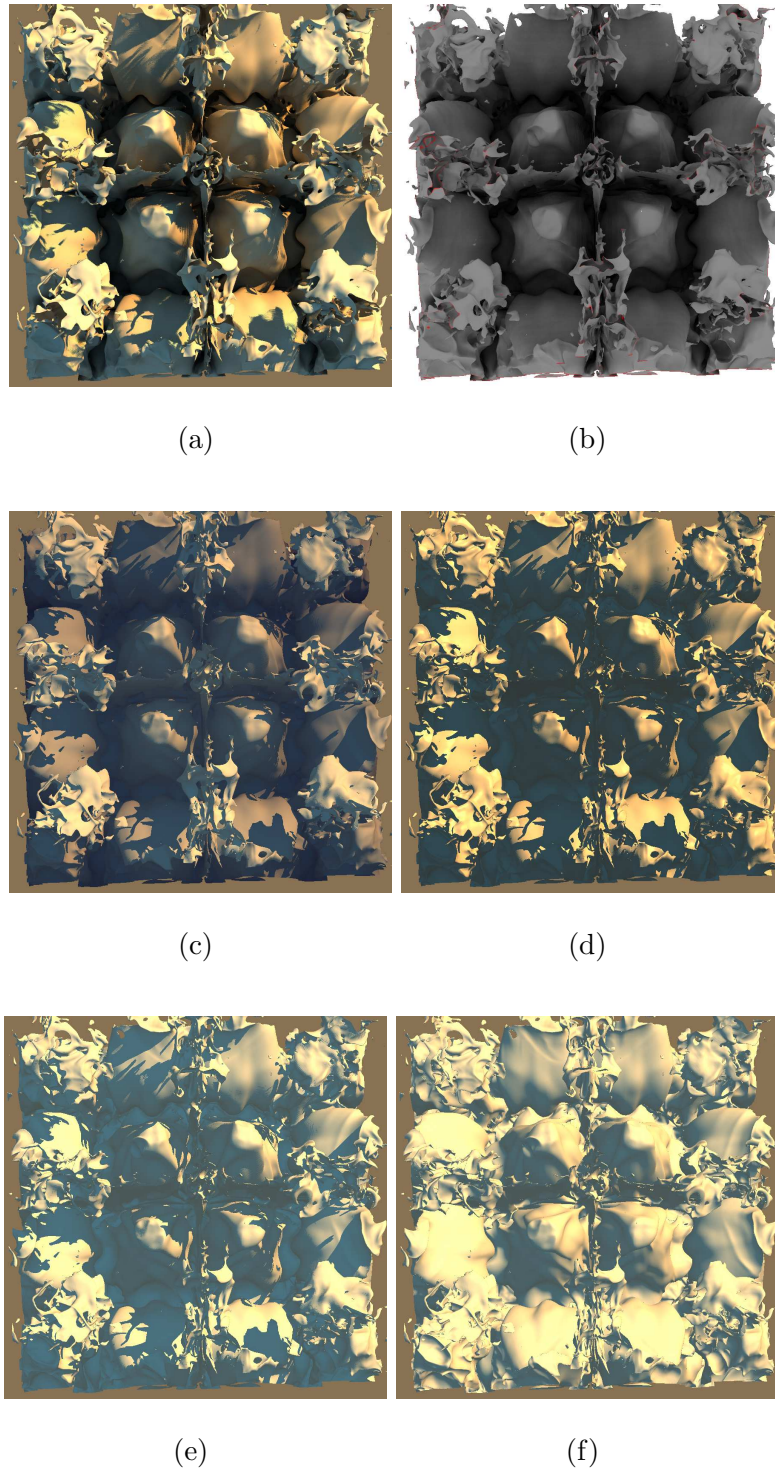


Figure 5.11. Another view of a Richtmyer-Meshkov instability simulation. This different view using (a) the new technique, (b) vicinity shading, (c) Lambertian with fog, (d) Phong with varying ambient, (e) Lambertian with varying ambient, and (f) Lambertian without shadows.

ignoring diffuse bounces and insisting on constant illumination, identical results can be achieved utilizing the illumination texture (as seen in Figure 5.12). Although vicinity shading shades concavities darker than unoccluded regions, recent studies show humans use more than a “darker-means-deeper” perceptual metric to determine shape in an image [75]. By allowing interreflections between surfaces and more complex illumination, the new approach adds additional lighting effects which may help users perceive shape. However, if shadows or other illumination effects inhibit perception for a particular dataset, they can be removed from the illumination computations.

The results comparable favorably to Monte Carlo pathtracing, particularly when using an irradiance texture. As each irradiance texel is computed using pathtracing, the differences seen in Figure 5.13 result from the issues discussed in Sections 5.2 and 5.3. For the spherical harmonic representation, the resulting illumination is smoother and a bit darker. Illumination intensity varies slightly based on the SH sampling of the environment and material transfer functions, and the SH results in Figure 5.8 appear a bit brighter than the pathtraced results. Figure 5.8 compares the convergence of illumination using a fifth order SH basis, single irradiance values, and per-pixel pathtracing. As expected, the SH representation converges significantly faster than pathtracing, and the irradiance texture converges at roughly the same rate, though the noise is blurred by the trilinear interpolation.

One last consideration when using this technique is what resolution illumination

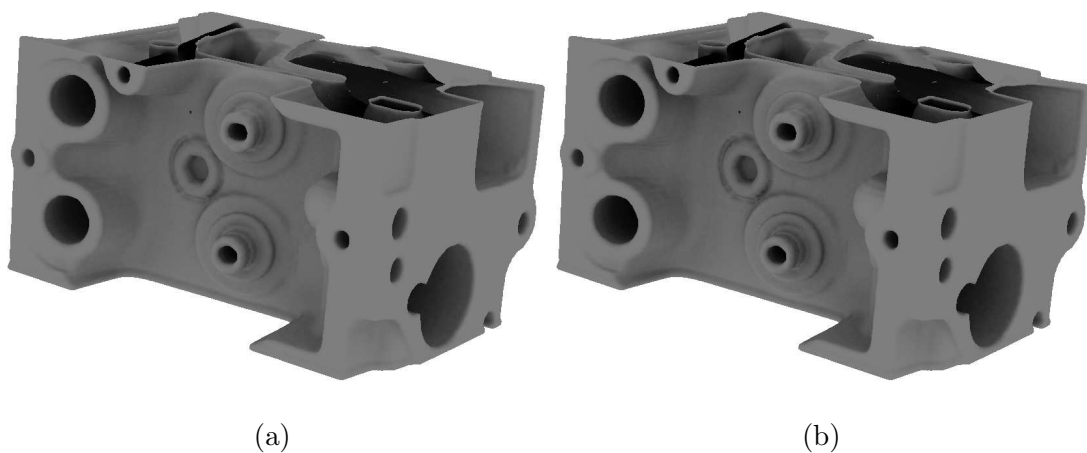


Figure 5.12. Comparison with vicinity shading. Compare (a) the new technique and (b) vicinity shading with 625 samples per voxel.

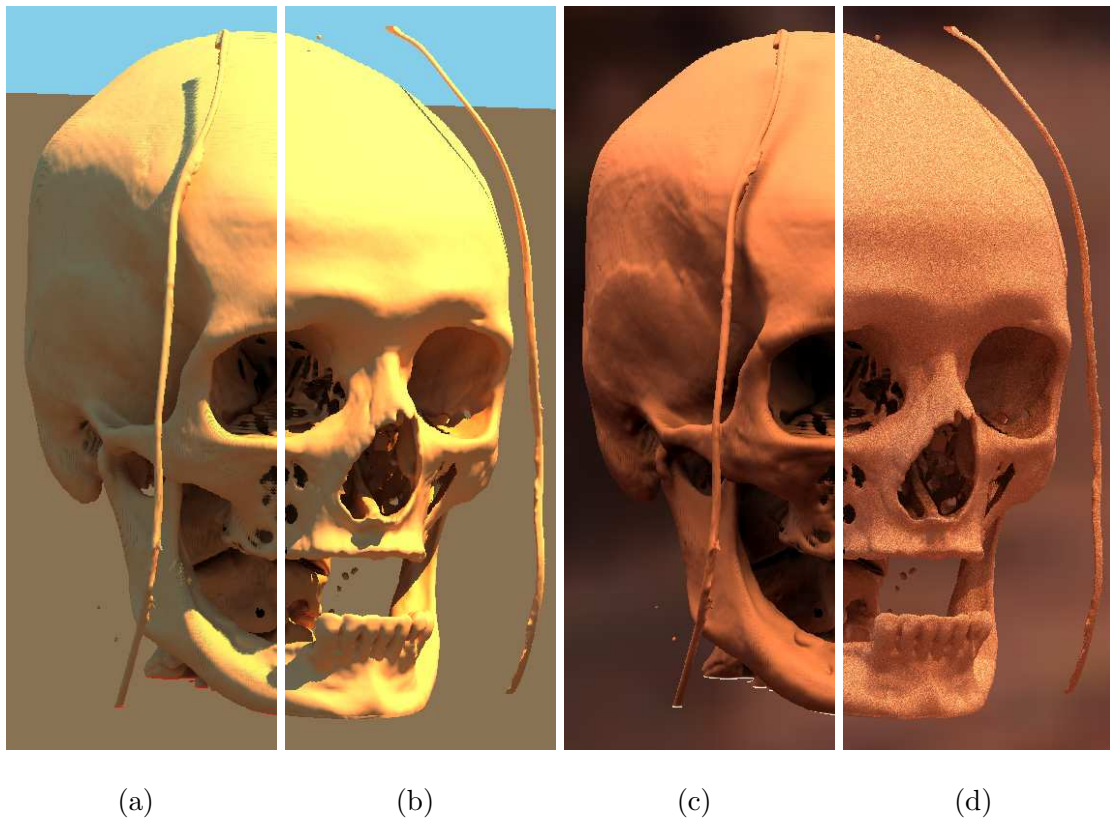
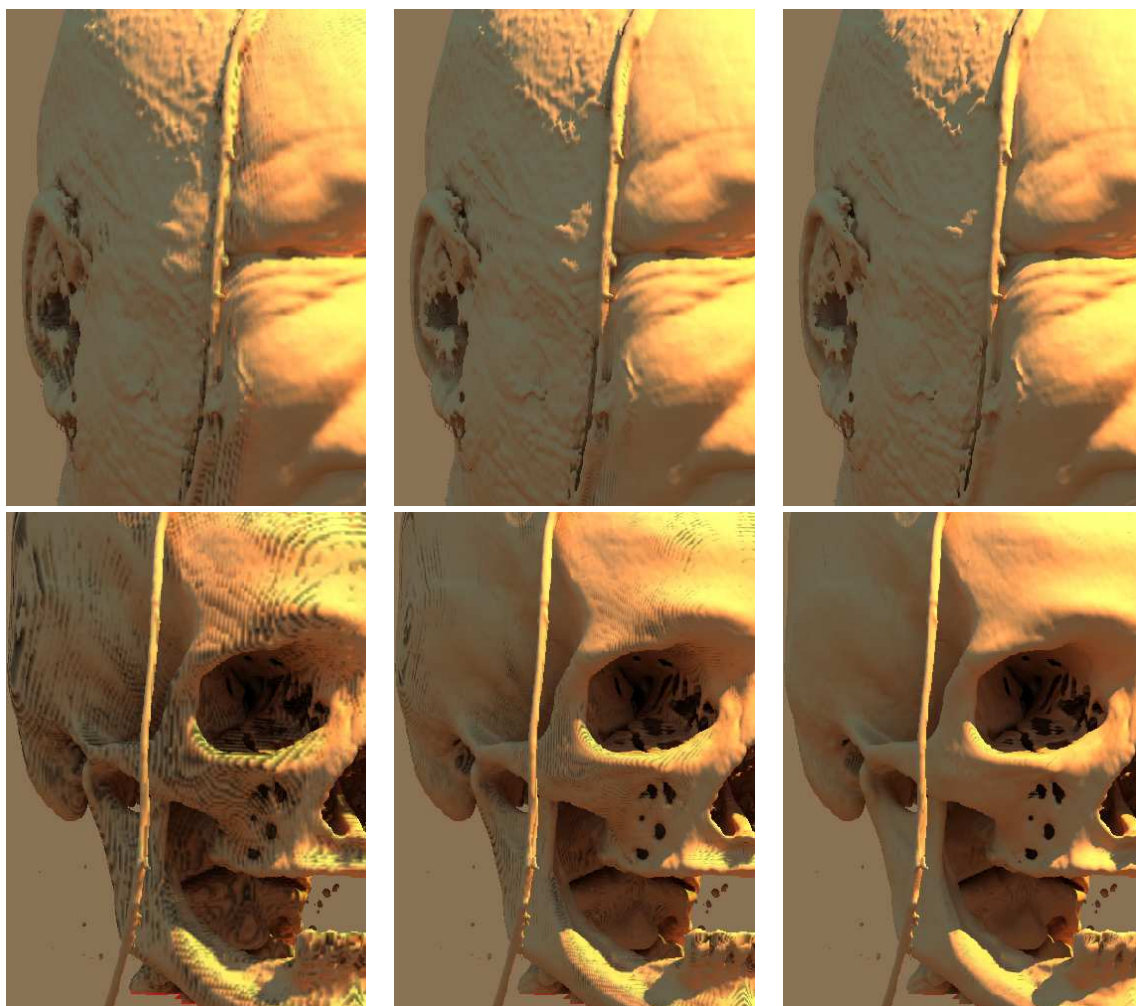


Figure 5.13. The new technique versus Monte Carlo pathtracing with 10000 samples per pixel. At left, compare (a) an irradiance texture to (b) pathtracing in a bicolored environment. At right, compare (c) a fifth order spherical harmonic representation to (d) pathtracing inside a lightprobe of St. Peter's cathedral.

texture gives the best results. Figure 5.14 compares the Visible Female head with three different resolutions. It turns out that using roughly the same resolution for the illumination and the data gave reasonable results for all the test cases. In regions where isosurfaces vary significantly, sampling more finely may be desirable. For instance, illumination texels near the bone isosurface from Figure 5.14 fall on relatively distant isosurfaces giving rise to more banding artifacts. Surfaces like the skin change slowly



(a)

(b)

(c)

Figure 5.14. Effect of different illumination volume resolutions. Illumination texture of (a) $1/8$, (b) 1 , and (c) 8 times the resolution of the head dataset. Due to the high variation in isovalues near the bone isosurface, a denser illumination sampling is needed to avoid banding artifacts.

with changing isovalue, so a less dense illumination texture suffices.

This chapter introduced a method for precomputing and interactively rendering global illumination for surfaces from volume datasets. By storing illumination data in a three-dimensional texture like the underlying volumetric data, interpolation between texels provides plausible global illumination at speeds faster than illumination models commonly used for visualization today. This approach generates high quality global illumination on dynamically changeable surfaces extracted from a volume, running on either GPU based visualization tools or interactive raytracers. Combining the technique with a spherical harmonic representation allows dynamic environmental lighting.

CHAPTER 6

CONCLUSIONS AND FUTURE WORK

In this dissertation, three approaches for approximating global illumination effects with local information have been described. These techniques split out individual global illumination effects to examine individually. This allows applications to incorporate the most important global illumination effects for their environments without including the computational baggage of unimportant effects. The three results presented include the penumbra map for interactively rendering soft shadows described in Chapter 3, the interactive caustic rendering using a simplified five-dimensional caustic described in Chapter 4, and the interactive visualization of isosurfaces under dynamic lighting by interpolating precomputed illumination samples described in Chapter 5.

Penumbra maps augment the standard shadow map approach for rendering hard shadows with information about penumbral intensity on surfaces visible from the center of the light. This technique generates plausible looking penumbrae for moderately complex models at over ten frames per second. Furthermore, implementations using standard shadow maps easily extend to allow penumbra mapping. This approach does not allow complete representation of the penumbra, but studies have shown accurate shape is unnecessary for human perception—a shadow that looks plausible could thus be perceived as real. For the penumbra map, as long as the penumbral regions are small relative to the total shadow size the results look convincing.

Future work might examine adding more information so the full penumbra can be rendered. This might be possible using a vertex program to adjust silhouette edge positions, or by including another corresponding map containing inner penumbral information. Unfortunately when adding another map, additional penumbrae will not reside on the foremost polygons in the shadow map. Additional work may allow implementation of the entire algorithm on a graphics card. Bleeding-edge graphics accelerators recently introduced support for render-to-vertex-array, which should allow silhouette extraction (via McCool’s approach [86]) and generation of cones and sheets entirely onboard, drastically

improving performance.

For rendering caustics, the eight-dimensional caustic function was simplified by examining caustic behavior and eliminating degrees of freedom which contribute little to the rendered result. These simplifications resulted in a five-dimensional function. When sampled locally near reflective and refractive objects, this representation allows interactive rendering of caustics with dynamic geometry and illumination. When rendering using this approach, tradeoffs exist between rendering speed, rendering quality, and memory consumption. Increased rendering speed comes at the cost of reduced quality or higher memory consumption (e.g., by using naive sampling and storage techniques). Tailoring the data representation to specific applications significantly reduces precomputation and memory costs. For instance, outdoor scenes typically require a single light direction, due to illumination from a constant direction.

A number of directions for future work on caustics exist. Additional data representations such as spherical wavelets, principle component analysis, or other basis functions may further compress the sampled caustic or allow higher fidelity reconstruction. A better measure over the five-dimensional caustic space is necessary for accurate interpolation between samples. Until such a measure is found, ad hoc interpolation will continue to cause artifacts for certain object types. Finally, perhaps representations other than spherical harmonics can allow interactive rendering of caustics from area lights without the blurriness inherent with a spherical harmonic representation.

The technique from Chapter 5 provides the first method for interactively rendering dynamic isosurfaces of a volumetric dataset with full global illumination. As users explore a volumetric dataset, they often vary the current isovalue to examine different portions of the volume; this interactive global illumination technique provides valuable global information to such users. A three-dimensional texture stores precomputed irradiance or spherical harmonic transfer functions, allowing rendering of any isosurface of the volume under arbitrary, changing lighting. Again, a tradeoff exists between rendering quality, rendering speed, and memory consumption. Using a single irradiance value at every texel, commodity graphics accelerators can render static global illumination on arbitrary isosurfaces. On the other hand, rendering dynamic lighting and complex material types requires a machine with multiple gigabytes of memory. Moreover, illumination computations can be performed lazily instead of as an expensive preprocess. Lazy computation allows illumination calculations for just the interesting isosurfaces instead of the entire

volume. This proves valuable if only a small subset of the volume need be displayed or if a long precomputation is undesirable.

Interesting future work in this area includes examining if illumination can be stored in a hierarchy instead of a regular grid. As indirect illumination generally varies slowly over local regions in space, hierarchical storage techniques could leverage slow gradations into reduced memory consumption. Compression techniques, both within a sample as well as over neighboring samples, may help reduce memory consumption without affecting rendering quality. Again, principal component analysis may reduce spherical harmonic coefficient storage. Spherical wavelets or other basis functions over the sphere may require fewer coefficients or lead to more practical compressions schemes. Finally, implementation of this technique using commodity graphics hardware is currently limited to small datasets by limited onboard memory. Research into hierarchy and compression schemes may allow more complex illumination textures to fit into graphics memory, allowing higher fidelity global illumination at interactive rates on desktop PCs.

Beyond direct extensions to the methods described in this dissertation, a number of questions remain as to the importance of global illumination. Studies show that shadows provide important information, yet visualization researchers widely claim that shadows and other complex illumination actually detract from perception of complex datasets. In some cases this may prove correct, but conducting user studies to determine when global illumination helps and when it hurts would yield interesting results. Furthermore, it may turn out that some global illumination effects help and some hurt. Or perhaps shadows detract from an image when included individually, but in conjunction with interreflections, which augment shading in shadowed regions, shadows may help. These questions all suggest interesting user studies.

Another open question is how much global illumination can be approximated without affecting perceived realism. By knowing which approximations detract from a user's experience, techniques focused on retaining salient information can be developed.

In summary, this dissertation suggested three different approaches for locally approximating global illumination effects. As interactive applications continue to become more realistic, they will begin demanding nonlocal illumination effects; however, global approaches that utilize the existing framework to accelerate local lighting will be accepted and integrated first, providing an intermediate step on the way to full interactive global illumination.

APPENDIX A

SHADER CODE FOR PENUMBRA MAPS

This appendix provides the vertex and fragment shader programs used in Chapter 3. The code conforms to the `ARB_vertex_program` and `ARB_fragment_program` OpenGL extensions [116] defined by the OpenGL Architecture Review Board. These programs will run on any graphics board that supports these ARB extensions; however, they were designed on and optimized for ATI Radeon 9700 graphics cards, so they run significantly faster on the ATI Radeon line of graphics cards than on corresponding generation graphics cards from nVidia.

A.1 Generating a Penumbra Map

The penumbra map is rendered into a *p-buffer*, which is a buffer in onboard video memory that does not get rendered to the screen. Once rendered, a p-buffer can be used as a texture in a later render pass. Figures A.1 and A.2 show the vertex and fragment

```
!!ARBvp1.0
## Grab the OpenGL state variables the vertex & fragment shaders use.
ATTRIB v24 = vertex.texcoord[0];
ATTRIB v19 = vertex.color;
ATTRIB v16 = vertex.position;
PARAM s259[4] = { state.matrix.mvp };

## Move texcoord[0] & [1] directly to the fragment shader, the
## graphics card will linearly interpolate them for us.
MOV result.texcoord[1], v19;
MOV result.texcoord[0], v24;

## Apply the modelview/projection matrix to the vertex positions.
DP4 result.position.x, s259[0], v16;
DP4 result.position.y, s259[1], v16;
DP4 result.position.z, s259[2], v16;
DP4 result.position.w, s259[3], v16;
END
```

Figure A.1. Vertex program for rendering a penumbra map.

```

!!ARBfp1.0
## Stores {1/pbufferWidth, 1/pbufferHeight, 1, 1}
PARAM u0 = program.local[0];

## The 3 and 2 are used for Bernstein interpolation...
PARAM c0 = {1, 0, 3, 2};
TEMP R0, R1, H0;

## Take window position, convert to [0-1] tex space
MUL R0.xyz, fragment.position, u0;

## Lookup depth in shadow map
TEX R1.y, R0.xyxx, texture[0], 2D;

## Compare  $Z_F, Z_P$ , kill if  $Z_F > Z_P$ 
## (of course, current cards the kill doesn't *actually* do
## anything, so this doesn't really speed things up)
ADD R0.x, R1.y, -R0.z;
CMP H0.x, R0.x, -c0.x, -c0.y;
KIL H0;

## Convert to world space & computation of I
## * Texcoord[0] contains far/near values needed to convert to
## world space. This probably could have been a local param
## instead of passing through the texture coordinate.
## * Texcoord[1] contains  $Z_{V_i}$  and assorted other forms to make
## the conversion & I computation easier (i.e. fewer operations)
MAD R0.x, R1.y, fragment.texcoord[0].x, -fragment.texcoord[0].z;
RCP R0.x, R0.x;
MAD R0.y, -fragment.texcoord[0].y, R0.x, -fragment.texcoord[1].x;
MUL R0.y, fragment.texcoord[1].z, R0.y;
RCP R0.y, R0.y;
ADD R0.x, fragment.texcoord[1].y, -fragment.texcoord[1].x;
MUL R0.y, R0.x, R0.y;
ADD R0.x, R0.y, -c0.y;
CMP H0.x, R0.x, c0.x, c0.y;
CMP R0.y, -H0.x, c0.x, R0.y;

## Compute Bernstein interpolation
MAD R0.x, -c0.w, R0.y, c0.z;
MUL R0.y, R0.y, R0.y;
MUL R0.y, R0.x, R0.y;

## Stores the output color into color.zw and depth.z
## Stores the shadow map into color.x (so we only use 1 texture)
MOV result.color.zw, R0.y;
MOV result.color.x, R1.y;
MOV result.color.y, fragment.texcoord[1].w;
MOV result.depth.z, R0.y;
END

```

Figure A.2. Fragment program for rendering a penumbra map.

programs used for this work. The value of the `vertex.texcoord[0]` input to the shaders is:

$$vertex.texcoord[0] = \begin{pmatrix} l_{far} - l_{near} \\ l_{far} * l_{near} \\ l_{far} \\ l_{near} \end{pmatrix},$$

where l_{far} and l_{near} are the distances to the far and near planes when rendering the shadow map (i.e., the far and near planes from the light's point of view). Note a slightly faster and better approach would be to pass these directly to the fragment program, as they are constant over the polygon and do not need interpolation by the rasterizer. The value of the `vertex.color` shader input is given by:

$$vertex.color = \begin{pmatrix} Z_{V_i} \\ current_z \\ 1.0 \\ proj_z \end{pmatrix},$$

where Z_{V_i} is the distance to the silhouette vertex, $current_z$ is the distance to the current vertex, and $proj_z$ is the projected depth of the silhouette vertex (i.e., $proj_z \in [0, 1]$).

A.2 Rendering with a Penumbra Map

Figures A.3 and A.4 show the vertex and fragment shaders used to render using a penumbra map and a simple Phong shading model for the direct illumination. The vertex program mainly performs Phong lighting computations, except for the transformation of the world-space vertex positions into light space via the `matrix.program[0]` matrix, which contains the $\mathbf{SP}_{light}\mathbf{L}^{-1}\mathbf{V}$ matrix given in Equation 4 from Everitt et al. [34].

Notice in the fragment shader, the texture `texture[0]` contains the shadow map in the red (or x) channel, the penumbra map in the blue and alpha (or z and w) channels, and the $proj_z$ value interpolated during penumbra map creation is stored in the green (or y) channel. $proj_z$ was used in the program as a reality check, to determine if penumbræ were being cast onto the correct surfaces.

```

!!ARBvp1.0
PARAM c6 = { 0, 0, 1, 1 }, c7 = { 75, 0, 0, 0 };
TEMP R0, R1, R2, R3;
ATTRIB v16 = vertex.position, v18 = vertex.normal;
PARAM c0 = program.local[0]; ## The light position
PARAM s631[4] = { state.matrix.modelview[0].invtrans };
PARAM s255[4] = { state.matrix.projection };
PARAM s327[4] = { state.matrix.program[0] };
PARAM s223[4] = { state.matrix.modelview[0] };
## Apply the modelview matrix to the vertex position.
DP4 R0.x, s223[0], v16;
DP4 R0.y, s223[1], v16;
DP4 R0.z, s223[2], v16;
DP4 R0.w, s223[3], v16;
## Convert vertex position into (a) projected light coords
## (for shadow map texture lookup) and (b) projected eye coords
DP4 result.texcoord[0].x, s327[0], R0;
DP4 result.texcoord[0].y, s327[1], R0;
DP4 result.texcoord[0].z, s327[2], R0;
DP4 result.texcoord[0].w, s327[3], R0;
DP4 result.position.x, s255[0], R0;
DP4 result.position.y, s255[1], R0;
DP4 result.position.z, s255[2], R0;
DP4 result.position.w, s255[3], R0;
## Find the normalized light direction.
ADD R1, c0, -R0;
DP3 R0.x, R1, R1;
RSQ R0.x, R0.x;
MUL R3, R0.x, R1;
## Find the transformed surface normal & normalize it.
DP4 R1.x, s631[0], v18;
DP4 R1.y, s631[1], v18;
DP4 R1.z, s631[2], v18;
DP4 R1.w, s631[3], v18;
DP3 R0.x, R1, R1;
RSQ R0.x, R0.x;
MUL R2.xyz, R0.x, R1;
## Perform vertex-level Phong illumination computations.
DP3 R0.x, R3, R2;
MOV result.color.front.primary, R0.x;
ADD R1, R3, c6;
DP3 R0.x, R1, R1;
RSQ R0.x, R0.x;
MUL R0.xyz, R0.x, R1;
DP3 R1, R2, R0;
MOV R0.xy, R1.x;
MOV R0.zw, c7.x;
LIT R0.z, R0;
MOV result.color.front.secondary, R0.z;
END

```

Figure A.3. Vertex program for rendering using a penumbra map.

```

!!ARBfp1.0
PARAM u0 = program.local[0];
PARAM c0 = {1.0, 1.0, 0.0, 0.0};
PARAM c1 = {1.0, 1.0, 1.0, 1.0};
TEMP R0, R1, R3, H0;

## Do the perspective divide on the shadow map coords.
RCP R0.x, fragment.texcoord[0].w;
MUL R0.xyz, fragment.texcoord[0], R0.x;

## Compare current fragment coords with shadow map frustum.
## If outside frustum, then R1.x is non-zero.
CMP H0.xy, R0, c0.x, c0.z;
MOV R1.xy, H0;
ADD R1.zw, R0.xxxxy, -c0.x;
CMP H0.xy, R1.zwww, c0.z, c0.x;
MOV R1.zw, H0.xxxxy;
DP4 R1.x, R1, c1;

## Grab the value in the combined penumbra/shadow map.
## Compare shadow map (R3.x) to fragment's light depth (R0.z).
TEX R3, R0, texture[0], 2D;
ADD R0.x, R0.z, -R3.x;
ADD R0.x, u0.x, -R0; ## Add in shadow map bias.
CMP H0.x, R0.x, c0.x, c0.z; ## Is illuminated?
CMP R0.x, -H0, c0.z, c0.x; ## Convert from a (H) register to an (R)
CMP R0.x, -R1, c0, R0; ## Consider if inside frustum

## Reality check: shadowing correct surface?
## (Probably can be removed/moved to someplace cheaper)
ADD R3.y, fragment.position.z, -R3.y;
ADD R3.y, u0.y, -R3.y;
CMP R3.z, R3.y, R3.z, c1;

## Perform Phong lighting, modulate by light intensity value.
MUL R0.x, R0.x, R3.z;
MUL R1, fragment.color.secondary.x, state.material.front.specular;
MAD R1, fragment.color.primary.x, state.material.front.diffuse, R1;
MAD result.color, R0.x, R1, state.material.front.ambient;
END

```

Figure A.4. Fragment program for rendering using a penumbra map.

APPENDIX B

SPHERICAL HARMONICS

Spherical harmonics provide an orthogonal basis for functions defined on a unit sphere. As global illumination deals with incident and exitant energies over spheres and hemispheres, spherical harmonics are a natural basis for representing these functions. A number of researchers [14, 106, 107, 108, 117, 119, 120] have used spherical harmonic coefficients to store illumination values, though few take time to clearly describe the mathematics supporting the approach or describe implementational details. Hence, actually implementing their techniques requires significant background reading of cryptic mathematics texts.

B.1 Laplace's Equation in Spherical Coordinates

A *harmonic* is a function that satisfies Laplace's equation:

$$\nabla^2 \varphi = 0. \quad (\text{B.1})$$

In spherical coordinates, Laplace's equation becomes:

$$\left[\frac{1}{r^2} \frac{\partial}{\partial r} \left(r^2 \frac{\partial}{\partial r} \right) + \frac{1}{r^2 \sin^2 \theta} \frac{\partial^2}{\partial \phi^2} + \frac{1}{r^2 \sin \theta} \frac{\partial}{\partial \theta} \left(\sin \theta \frac{\partial}{\partial \theta} \right) \right] \varphi = 0. \quad (\text{B.2})$$

By using separation of variables, where $\varphi = R(r)\Phi(\phi)\Theta(\theta)$ and eliminating the $\frac{1}{r^2}$ factor:

$$\Theta(\theta)\Phi(\phi) \frac{\partial}{\partial r} \left(r^2 \frac{\partial R(r)}{\partial r} \right) + \frac{\Theta(\theta)}{\sin^2 \theta} \frac{\partial^2 \Phi(\phi)}{\partial \phi^2} + \frac{\Phi(\phi)}{\sin \theta} \frac{\partial}{\partial \theta} \left(\sin \theta \frac{\partial \Theta(\theta)}{\partial \theta} \right) = 0. \quad (\text{B.3})$$

By dividing through by $\Phi(\phi)\Theta(\theta)$, the r -dependence is reduced to a single term:

$$\frac{\partial}{\partial r} \left(r^2 \frac{\partial R(r)}{\partial r} \right) + \frac{1}{\Phi(\phi) \sin^2 \theta} \frac{\partial^2 \Phi(\phi)}{\partial \phi^2} + \frac{1}{\Theta(\theta) \sin \theta} \frac{\partial}{\partial \theta} \left(\sin \theta \frac{\partial \Theta(\theta)}{\partial \theta} \right) = 0. \quad (\text{B.4})$$

As the r -dependent terms and the r -independent terms are constant relative to each other and sum to zero, equating the r -dependent term to a constant (of the form $l(l+1)$ [5]) gives:

$$\frac{\partial}{\partial r} \left(r^2 \frac{\partial R(r)}{\partial r} \right) = l(l+1). \quad (\text{B.5})$$

Substituting Equation B.5 back into Equation B.4 eliminates the dependency on r , resulting in the *spherical harmonic differential equation*:

$$l(l+1)\Phi(\phi)\Theta(\theta) + \frac{\Theta(\theta)}{\sin^2\theta} \frac{\partial^2\Phi(\phi)}{\partial\phi^2} + \frac{\Phi(\phi)}{\sin\theta} \frac{\partial}{\partial\theta} \left(\sin\theta \frac{\partial\Theta(\theta)}{\partial\theta} \right) = 0. \quad (\text{B.6})$$

The solutions to Equation B.6 are called *spherical harmonics*, and can be computed by continuing the separation of variables. Multiplying by $\frac{\sin^2\theta}{\Phi(\phi)\Theta(\theta)}$ reduces ϕ -dependency to a single term, which again can be equated to a constant (typically called $-m^2$):

$$\frac{1}{\Phi(\phi)} \frac{\partial^2\Phi(\phi)}{\partial\phi^2} = -m^2, \quad (\text{B.7})$$

which has solutions:

$$\Phi(\phi) = Ae^{-im\phi} + Be^{im\phi}. \quad (\text{B.8})$$

Plugging Equation B.7 back into Equation B.6 gives an equation dependent on only θ :

$$l(l+1)\sin^2\theta - m^2 + \frac{\sin\theta}{\Theta(\theta)} \frac{\partial}{\partial\theta} \left(\sin\theta \frac{\partial\Theta(\theta)}{\partial\theta} \right) = 0. \quad (\text{B.9})$$

And by replacing $\cos\theta$ with x , and $\partial\theta$ with $\frac{\partial x}{-\sin\theta}$, Equation B.9 becomes:

$$\frac{\partial}{\partial x} \left[(1-x^2) \frac{\partial\Theta}{\partial x} \right] + \left[l(l+1) - \frac{m^2}{1-x^2} \right] \Theta = 0. \quad (\text{B.10})$$

Equation B.10 is known as the *associate Legendre differential equation*, which has solutions [5, 13]:

$$\Theta(\theta) = P_l^m(\cos\theta), \quad -l \leq m \leq l \text{ for } l, m \in \mathbb{Z}. \quad (\text{B.11})$$

Here $P_l^m(x)$ are the *associated Legendre polynomials*, discussed further in Section B.2. Combining the solutions for $\Phi(\phi)$ and $\Theta(\theta)$ with a normalization factor gives a solution for the angular portion of Laplace's Equation in spherical coordinates. These are the spherical harmonics $Y_l^m(\theta, \phi)$, defined for $\theta \in [0, \pi]$ and $\phi \in [0, 2\pi)$ as:

$$Y_l^m(\theta, \phi) \equiv \sqrt{\frac{2l+1}{4\pi} \frac{(l-m)!}{(l+m)!}} P_l^m(\cos\theta) e^{im\phi}, \quad (\text{B.12})$$

here the normalization constant $\sqrt{\frac{2l+1}{4\pi} \frac{(l-m)!}{(l+m)!}}$ is chosen such that

$$\int_0^{2\pi} \int_0^\pi Y_{l_1}^{m_1}(\theta, \phi) \overline{Y_{l_2}^{m_2}(\theta, \phi)} \sin\theta d\theta d\phi = \delta_{m_1, m_2} \delta_{l_1, l_2}, \quad (\text{B.13})$$

with \bar{z} defined as the complex conjugate of z .

B.2 Legendre Polynomials

Legendre polynomials are the solution to the *Legendre differential equation*, which is a second-order ordinary differential equation of the form:

$$(1-x^2)\frac{\partial^2 y}{\partial x^2} - 2x\frac{\partial y}{\partial x} + l(l+1)y = \frac{\partial}{\partial x} \left[(1-x^2)\frac{\partial y}{\partial x} \right] + l(l+1)y = 0, \quad (\text{B.14})$$

which is a special case of the associated Legendre differential equation given in Equation B.10, where $m = 0$. The solutions to Equations B.10 and B.14 are $P_l^m(x)$ and $P_l(x)$, respectively the associated and unassociated Legendre functions. When $l, m \in \mathbb{Z}$ and $x \in \mathbb{R}$ these functions become polynomial.

Interestingly, these functions have many representations, allowing for significant implementational freedom to choose between speed and accuracy. Legendre polynomials are special cases of hypergeometric functions ${}_pF_q$, such that:

$$P_l(x) = {}_2F_1(-l, l+1; 1; \frac{1}{2}(1-x)) = \sum_{n=0}^{\infty} \frac{(-l)_n (l+1)_n}{n! n!} \left(\frac{1}{2}(1-x)\right)^n, \quad (\text{B.15})$$

where $(a)_b$ is the *rising factorial* defined as $(a)_b = a(a+1)\cdots(a+b-1)$. Note that this sum converges, as $(-l)_n$ spans zero for $n > l$. Alternately, the Rodrigues representation yields a generating function for $P_l(x)$ [148] which expands to:

$$P_l(x) = \frac{1}{2^l} \sum_{k=0}^{\lfloor l/2 \rfloor} \frac{(-1)^k (2l-2k)!}{k!(l-k)!(l-2k)!} x^{l-2k} = \frac{1}{2^l} \sum_{k=0}^{\lfloor l/2 \rfloor} (-1)^k \binom{l}{k} \binom{2l-2k}{l} x^{l-2k}. \quad (\text{B.16})$$

Finally, the Legendre polynomials satisfy the following recurrence relations, with Equation B.18 providing more numerical stability for computational implementations [5]:

$$P_{l+1}(x) = \frac{(2l+1)x}{l+1} P_l(x) - \frac{l}{l+1} P_{l-1}(x) \quad (\text{B.17})$$

$$= 2xP_l(x) - P_{l-1}(x) - \frac{xP_l(x) - P_{l-1}(x)}{l-1}. \quad (\text{B.18})$$

The associated Legendre polynomials can be written in terms of the unassociated polynomials. As long as $l \geq 0$ and $0 \leq m \leq l$:

$$P_l^m(x) = (-1)^m (1-x^2)^{m/2} \frac{\partial^m}{\partial x^m} P_l(x). \quad (\text{B.19})$$

The polynomials with negative m values correspond to the polynomials with positive m via the following identity:

$$P_l^{-m}(x) = (-1)^m \frac{(l-m)!}{(l+m)!} P_l^m(x). \quad (\text{B.20})$$

Equations B.19 and B.20 provide a framework to compute the spherical harmonic basis functions, but this approach is computationally infeasible due to the m th partial derivatives used in Equation B.19. Luckily another representation exists for the associated

Legendre polynomials. Four relations allow easy computation of all associated Legendre polynomials with $m > 0$:

$$P_{l+1}^m(x) = \frac{x(2l+1)}{l-m+1}P_l^m(x) - \frac{l+m}{l-m+1}P_{l-1}^m, \quad (\text{B.21})$$

$$P_l^{m+1}(x) = \frac{2mx}{\sqrt{1-x^2}}P_l^m(x) + [m(m-1) - l(l+1)]P_l^{m-1}, \quad (\text{B.22})$$

$$P_{l+1}^l(x) = x(2l+1)P_l^l(x), \quad (\text{B.23})$$

$$P_l^l(x) = (-1)^l(2l-1)!!(1-x^2)^{\frac{1}{2}}. \quad (\text{B.24})$$

Not all four relations are necessary to compute P_l^m for all m, l , but choosing relations for a particular application can reduce discretization error. Only two equations are necessary to compute all P_l^m , though Green [43] suggests combining Equations B.21, B.23, and B.24 to reduce errors for spherical harmonic based illumination. In Equation B.24, $n!!$ is the *double factorial*, defined for positive integers. For n odd, $n!! = n \cdot (n-2) \cdots 5 \cdot 3 \cdot 1$, and for n even, $n!! = n \cdot (n-2) \cdots 6 \cdot 4 \cdot 2$. Two special cases are defined, which makes computation of $n!!$ easy, as $-1!! \equiv 0!! \equiv 1$.

To find the associated Legendre polynomials with negative m , use the relation:

$$P_l^{-m}(x) = (-1)^m \frac{(l-m)!}{(l+m)!} P_l^m(x). \quad (\text{B.25})$$

Another useful identity, particularly when finding the spherical harmonic normalization factor using Equation B.13, shows how to integrate the product of two associated Legendre polynomials:

$$\int_{-1}^1 P_{l_1}^m(x) P_{l_2}^m(x) dx = \frac{2\delta_{l_1, l_2} (l_1 + m)!}{(2l_1 + 1)(l_1 - m)!} = \frac{2\delta_{l_1, l_2} (l_2 + m)!}{(2l_2 + 1)(l_2 - m)!}. \quad (\text{B.26})$$

B.3 Spherical Harmonics

Spherical harmonics functions $Y_l^m(\theta, \phi)$ are the angular portion of the solution to Laplace's equation in spherical coordinates (Equation B.2). They represent an infinite set of orthogonal functions over the sphere. In fact, any function $f(\theta, \phi)$ over the unit sphere can be represented in terms of the complex spherical harmonic basis:

$$f(\theta, \phi) \equiv \sum_{l=0}^{\infty} \sum_{m=-l}^l A_l^m Y_l^m(\theta, \phi), \quad (\text{B.27})$$

where A_l^m are the spherical harmonic coefficients. The function $f(\theta, \phi)$ can also be written in terms of the real spherical harmonic basis functions:

$$f(\theta, \phi) \equiv \sum_{l=0}^{\infty} \sum_{m=0}^l [C_l^m Y_l^{m^c}(\theta, \phi) + S_l^m Y_l^{m^s}(\theta, \phi)]. \quad (\text{B.28})$$

The representation in Equation B.28 is a *Laplace series*, which is a *generalized Fourier series*. In this sense, spherical harmonics are analogous to the Fourier basis in one dimension. Here $Y_l^{m^c}$ and $Y_l^{m^s}$ are respectively the real and imaginary parts of Y_l^m :

$$Y_l^{m^c} \equiv \sqrt{\frac{2l+1}{4\pi} \frac{(l-m)!}{(l+m)!}} P_l^m(\cos\theta) \cos(m\phi), \quad (\text{B.29})$$

$$Y_l^{m^s} \equiv \sqrt{\frac{2l+1}{4\pi} \frac{(l-m)!}{(l+m)!}} P_l^m(\cos\theta) \sin(m\phi). \quad (\text{B.30})$$

Generally, the single symbol $Y_l^m(x)$ is used in global illumination literature to represent the real spherical harmonic functions instead of a pair of symbols, such as $Y_l^{m^c}(x)$ and $Y_l^{m^s}(x)$. To understand the illumination definition, realize that Equation B.28 could easily be rewritten:

$$f(\theta, \phi) = \sum_{l=0}^{\infty} \left[\sum_{m=0}^l C_l^m Y_l^{m^c}(\theta, \phi) + \sum_{m=-l}^0 S_l^{|m|} Y_l^{|m|^s}(\theta, \phi) \right]. \quad (\text{B.31})$$

Thus, the real form of the spherical harmonics are typically written in cases, such that:

$$Y_l^m(\theta, \phi) = \begin{cases} \sqrt{\frac{2l+1}{2\pi} \frac{(l-m)!}{(l+m)!}} P_l^m(\cos\theta) \cos(m\phi) & \text{if } m > 0 \\ \sqrt{\frac{2l+1}{4\pi}} P_l^0(\cos\theta) & \text{if } m = 0 \\ \sqrt{\frac{2l+1}{2\pi} \frac{(l-|m|)!}{(l+|m|)!}} P_l^m(\cos\theta) \sin(|m|\phi) & \text{if } m < 0 \end{cases}. \quad (\text{B.32})$$

Notice the normalization factor has changed from the case of complex spherical harmonics. Here the normalization factors have once again been chosen to satisfy Equation B.13. In the rest of this chapter, Y_l^m refers to a real spherical harmonic basis function, as defined in Equation B.32.

B.4 Using Spherical Harmonics Bases

By approximating a spherical function using a finite sum of the form:

$$f(\theta, \phi) = \sum_{l=0}^{\infty} \sum_{m=-l}^l C_l^m Y_l^m(\theta, \phi) \approx \sum_{l=0}^{n-1} \sum_{m=-l}^l C_l^m Y_l^m(\theta, \phi),$$

a low frequency function can easily be represented with a few C_l^m coefficients instead of a more complex form, like an environment map. But the real advantage of using a spherical harmonic basis, particularly for lighting computations, is the property that integration of

two functions simplifies to a dot product of their spherical harmonic coefficients C_l^m . In other words, if f has spherical harmonic coefficients a_l^m and g has coefficients b_l^m then:

$$\int_{\theta, \phi} f(\theta, \phi)g(\theta, \phi)d\theta d\phi = \sum_{l=0}^{\infty} \sum_{m=-l}^l a_l^m b_l^m \approx \sum_{l=0}^{n-1} \sum_{m=-l}^l a_l^m b_l^m = \sum_{i=0}^{n^2} a_i b_i. \quad (\text{B.33})$$

Often for ease of use, coefficients are represented with a single dimensional array a_i instead of a two-dimensional array a_l^m . In this case, $i = l(l+1) + m$, and the sum above simplifies to a summation over i . Typically, an n th order spherical harmonic representation is taken to include the bands $l = 0 \dots n-1$ and requires n^2 coefficients. For clarity of notation when using a_i , Y_i will be used for Y_l^m .

Finding the coefficients a_i for function f is called *projecting* f into the spherical harmonic basis. Projection is accomplished by integrating f over the sphere \mathbb{S} with respect to each basis function Y_i :

$$a_i = \int_{s \in \mathbb{S}} f(s)Y_i(s)ds. \quad (\text{B.34})$$

As $f(\theta, \phi)$ often has no closed form solution or is defined on discrete samples (e.g., a texture map), computing this integral numerically proves simpler in practice. Generally, this is done using Monte Carlo integration [89]. By sampling randomly over the domain of a function h , the Monte Carlo method approximates an integral by the sum:

$$\int h(x)dx \approx \frac{1}{N} \sum_{i=1}^N \frac{h(x_i)}{p(x_i)}, \quad (\text{B.35})$$

where N is the number of samples, and $p(x_i)$ is the *probability density function* of the samples x_i . Basically, this approach averages numerous samples over the domain of h to approximate the integral. If nonuniform samples are used, or if the domain has non-unit length, area, volume, etc., the probability density function accounts for the discrepancy. For projecting a function $f(\theta, \phi)$ into spherical harmonic coefficients, using a uniform sampling over the sphere gives $p(x) = \frac{1}{4\pi}$, as the surface area of a unit sphere is 4π . Uniform samples over the surface of a sphere can be generated with two random variables $\xi_1, \xi_2 \in [0, 1]$ by [43]:

$$\begin{aligned} (\theta, \phi) &= \left(2 \arccos(\sqrt{1 - \xi_1}), 2\pi\xi_2 \right) \\ (x, y, z) &= \left(2\sqrt{\xi_1(1 - \xi_1)} \cos(2\pi\xi_2), 2\sqrt{\xi_1(1 - \xi_1)} \sin(2\pi\xi_2), 1 - 2\xi_1 \right). \end{aligned}$$

For uniform samples over the hemisphere $p(x) = \frac{1}{2\pi}$ and the two random variables ξ_1 and ξ_2 map to the hemisphere via [115]:

$$\begin{aligned}(\theta, \phi) &= \left(\arccos(\sqrt{1 - \xi_1}), 2\pi\xi_2 \right) \\(x, y, z) &= \left(\sqrt{\xi_1} \cos(2\pi\xi_2), \sqrt{\xi_1} \sin(2\pi\xi_2), \sqrt{1 - \xi_1} \right).\end{aligned}$$

Consider the two spherical harmonic projected function $f(s)$ and $g(s)$ of order n , where f has known coefficients a_i and g has unknown coefficients b_i . Should the need arise to compute coefficients c_i of the product $h(s) = f(s)g(s)$, a *transfer matrix* \mathbf{F} can be derived such that:

$$c_i = \sum_{j=1}^{n^2} \mathbf{F}_{ij} b_j. \quad (\text{B.36})$$

The elements of this matrix can be computed

$$\mathbf{F}_{ij} = \int_{s \in \mathbb{S}} a(s) Y_i(s) Y_j(s) ds = \sum_{k=0}^{n^2} a_k \int_{s \in \mathbb{S}} Y_i(s) Y_j(s) Y_k(s) ds. \quad (\text{B.37})$$

These elements can be computed beforehand via numerical integration, or analytically:

$$\begin{aligned}\int_0^{2\pi} \int_0^\pi Y_{l_1}^{m_1}(\theta, \phi) Y_{l_2}^{m_2}(\theta, \phi) Y_{l_3}^{m_3}(\theta, \phi) \sin \theta d\theta d\phi \\= \sqrt{\frac{(2l_1 + 1)(2l_2 + 1)(2l_3 + 1)}{4\pi}} \begin{pmatrix} l_1 & l_2 & l_3 \\ 0 & 0 & 0 \end{pmatrix} \begin{pmatrix} l_1 & l_2 & l_3 \\ m_1 & m_2 & m_3 \end{pmatrix},\end{aligned}$$

where $\begin{pmatrix} l_1 & l_2 & l_3 \\ m_1 & m_2 & m_3 \end{pmatrix}$ is a Wigner 3j-symbol [33, 148].

This property is commonly used for nondiffuse BRDFs, where three spherical harmonic functions are used: one for the BRDF, one for the incident illumination, and one for the transfer function describing self-shadowing and interreflections. In this case, changing either the viewpoint or the illumination changes the rendered illumination, so two unknowns exist. For a single unknown, the dot product from Equation B.33 is sufficient, but for two unknowns a transfer matrix is necessary.

Most importantly for interactive global illumination approaches, spherical harmonics are rotationally invariant. This means a rotation before projection or an equivalent rotation after projection give identical results. Since projection requires Monte Carlo integration for most illumination functions, rotation of spherical harmonic coefficients proves significantly faster. Unfortunately, rotation of coefficients is not as simple as the 3×3 rotation matrix on the sphere. Rotation of n th order spherical harmonics

As the number of bands increases, the n th order coefficient rotation matrix $Z_{SH(\alpha)}^n$ expands as expected, with terms of $\cos(\alpha), \cos(2\alpha), \dots, \cos(n\alpha)$ and $\pm \sin(\alpha), \pm \sin(2\alpha), \dots, \pm \sin(n\alpha)$. The rotation around the x -axis by $\pm \frac{\pi}{2}$ can be described using the following matrix:

$$X_{SH(\pm \frac{\pi}{2})} = \begin{bmatrix} 1 & 0 & 0 & 0 & 0 & 0 & 0 & 0 & 0 & \dots \\ 0 & 0 & \mp 1 & 0 & 0 & 0 & 0 & 0 & 0 & \dots \\ 0 & \pm 1 & 0 & 0 & 0 & 0 & 0 & 0 & 0 & \dots \\ 0 & 0 & 0 & 1 & 0 & 0 & 0 & 0 & 0 & \dots \\ 0 & 0 & 0 & 0 & 0 & 0 & 0 & \mp 1 & 0 & \dots \\ 0 & 0 & 0 & 0 & 0 & -1 & 0 & 0 & 0 & \dots \\ 0 & 0 & 0 & 0 & 0 & 0 & -\frac{1}{2} & 0 & -\frac{\sqrt{3}}{2} & \dots \\ 0 & 0 & 0 & 0 & \pm 1 & 0 & 0 & 0 & 0 & \dots \\ 0 & 0 & 0 & 0 & 0 & 0 & -\frac{\sqrt{3}}{2} & 0 & \frac{1}{2} & \dots \\ \vdots & \vdots & \vdots & \vdots & \vdots & \vdots & \vdots & \vdots & \vdots & \ddots \end{bmatrix}.$$

These matrices give a straightforward method for arbitrarily rotating spherical harmonic coefficients; however, ZYZ Euler angle decompositions may not fit well into all applications. Additionally, performing five matrix multiply operations costs significantly more than a single matrix multiplication, even with matrices as sparse as $Z_{SH(\alpha)}$ and $X_{SH(\pm \frac{\pi}{2})}$. These multiplications can be performed symbolically, but the resulting matrix $R_{SH(\alpha, \beta, \gamma)}$ contains some very complex trigonometric equations, which may prove more difficult to store and evaluate than simply multiplying the five axis-aligned rotation matrices.

However, recent research from the computational chemistry community [58, 59] has led to the development of recurrence relations for building general rotation matrices, without relying on Euler angle decompositions. Assuming an ordinary 3×3 rotation matrix R defined as:

$$\mathbf{R} = \begin{bmatrix} R_{xx} & R_{xy} & R_{xz} \\ R_{yx} & R_{yy} & R_{yz} \\ R_{zx} & R_{zy} & R_{zz} \end{bmatrix},$$

let $[R_{s,t}]$ be defined for $-1 \leq s, t \leq 1$ as:

$$[R_{s,t}] = \begin{bmatrix} R_{yy} & R_{yz} & R_{yx} \\ R_{zy} & R_{zz} & R_{zx} \\ R_{xy} & R_{xz} & R_{xx} \end{bmatrix} = \begin{bmatrix} R_{-1,-1} & R_{-1,0} & R_{-1,1} \\ R_{0,-1} & R_{0,0} & R_{0,1} \\ R_{1,-1} & R_{1,0} & R_{1,1} \end{bmatrix}. \quad (\text{B.40})$$

Let $\mathbf{M}^i \equiv \mathbf{R}_{SH}^i$ (from Equation B.38) for notational clarity. Then for an n th order spherical harmonic (i.e., $0 \leq i < n$ and $-i \leq s, t \leq i$):

$$M_{s,t}^i = u_{s,t}^i U_{s,t}^i + v_{s,t}^i V_{s,t}^i + w_{s,t}^i W_{s,t}^i. \quad (\text{B.41})$$

Here s and t are indices ranging over elements of the $(2i+1) \times (2i+1)$ rotation matrix for the i th band of spherical harmonic coefficients. The coefficients u, v, w and functions U, V, W, P appear in Tables B.1, B.2, and B.3 and define the recurrence relation. Note these tables are from the original version of the Ivancic and Ruedenberg paper [58], which contains erroneous equations but correct tables. The errata [59] fix the typos in the relevant equations but introduce new ones into the table (for $V_{s,t}^i$ when $s < 0$). The table in Green [43] contains a different typo for the same entry.

B.6 C++ Code to Compute the Rotation Matrix

This section contains a C++ class which computes the spherical harmonic rotation matrix. The two functions visible to the rest of the program are the constructor

Table B.1. Definitions of numerical coefficients $u_{s,t}^i$, $v_{s,t}^i$, and $w_{s,t}^i$.

Coefficient	for $ t < i$	for $ t = i$
$u_{s,t}^i$:	$\sqrt{\frac{(i+s)(i-s)}{(i+t)(i-t)}}$	$\sqrt{\frac{(i+s)(i-s)}{2i(2i-1)}}$
$v_{s,t}^i$:	$\frac{1}{2} \sqrt{\frac{(1+\delta_{s,0})(i+ s -1)(i+ s)}{(i+t)(i-t)}} (1 - 2\delta_{s,0})$	$\frac{1}{2} \sqrt{\frac{(1+\delta_{s,0})(i+ s -1)(i+ s)}{2i(2i-1)}} (1 - 2\delta_{s,0})$
$w_{s,t}^i$:	$-\frac{1}{2} \sqrt{\frac{(i- s -1)(i- s)}{(i+t)(i-t)}} (1 - \delta_{s,0})$	$-\frac{1}{2} \sqrt{\frac{(i- s -1)(i- s)}{2i(2i-1)}} (1 - \delta_{s,0})$

Table B.2. Definitions of the functions $U_{s,t}^i$, $V_{s,t}^i$, and $W_{s,t}^i$.

Function	for $s = 0$	for $s > 0$	for $s < 0$
$U_{s,t}^i$:	${}_0P_{0,t}^i$	${}_0P_{s,t}^i$	${}_0P_{s,t}^i$
$V_{s,t}^i$:	${}_1P_{1,t}^i + {}_{-1}P_{-1,t}^i$	${}_1P_{s-1,t}^i \sqrt{1+\delta_{s,1}} - {}_{-1}P_{-s+1,t}^i (1-\delta_{s,1})$	${}_1P_{s+1,t}^i (1-\delta_{s,-1}) + {}_{-1}P_{-s+1,t}^i \sqrt{1+\delta_{s,-1}}$
$W_{s,t}^i$:	(N/A, as $w_{0,t}^i = 0$)	${}_1P_{s+1,t}^i + {}_{-1}P_{-s-1,t}^i$	${}_1P_{s-1,t}^i + {}_{-1}P_{-s+1,t}^i$

Table B.3. Definitions of the function ${}_rP_{s,t}^i$.

Function	for $ t < i$	for $t = i$	for $t = -i$
${}_rP_{s,t}^i$:	$R_{r,0}M_{s,t}^{i-1}$	$R_{r,1}M_{s,i-1}^{i-1} - R_{r,-1}M_{s,-i+1}^{i-1}$	$R_{r,1}M_{s,-i+1}^{i-1} + R_{r,-1}M_{s,i-1}^{i-1}$

`SHRotationMatrix()` and the function `applyMatrix()`, which applies the rotation matrix to a vector of spherical harmonic coefficients.

```

// SHRotationMatrix Class Definition File
// -----

// Takes a rotation matrix of the form:
//   ( r[0], r[3], r[6] )
//   ( r[1], r[4], r[7] ),
//   ( r[2], r[5], r[8] )
// and an order. Computes an  $order^2 \times order^2$  matrix.
class SHRotationMatrix {
private:
    int order;
    double inMatrix[9], *outMatrix;

    // Computes the  $order^2 \times order^2$  matrix
    void computeMatrix( void );

    // Compute an 1D index for (col,row) in the matrix
    int matIndex( int col, int row );

    // Computed as described in Table B.1.
    double u_i_st ( int i, int s, int t );
    double v_i_st ( int i, int s, int t );
    double w_i_st ( int i, int s, int t );

    // Computed as described in Table B.2.
    double U_i_st ( int i, int s, int t );
    double V_i_st ( int i, int s, int t );
    double W_i_st ( int i, int s, int t );

    // Computed as described in Table B.3.
    double P_r_i_st ( int r, int i, int s, int t );

    // Index into the input matrix for  $-1 \leq i, j \leq 1$ , as per Eq. B.40
    double R ( int i, int j );

    // Index into band l, element (a,b) of the result ( $-l \leq a, b \leq l$ )
    double M( int l, int a, int b );

public:
    // Constructor. Input: SH order &  $3 \times 3$  transformation matrix
    SHRotationMatrix( int order, double matrix[9] );
    ~SHRotationMatrix();

    // Applies the  $order^2 \times order^2$  matrix to vector 'in'
    void applyMatrix( double *in, double *out );
};

```

Figure B.1. Header file describing the SHRotationMatrix C++ class.

```
// Computes the  $u_{s,t}^i$  coefficient, as per Table B.1
double SHRotationMatrix::u_i_st( int i, int s, int t )
{
    return sqrt( (i+s)*(i-s) / ( abs(t)==i? 2*i*(2*i-1): (i+t)*(i-t) ) );
}
```

Figure B.2. Function definition for SHRotationMatrix::u_i_st().

```
// Computes the  $v_{s,t}^i$  coefficient, as per Table B.1
double SHRotationMatrix::v_i_st( int i, int s, int t )
{
    int delta = ( s==0 ? 1 : 0 );
    double factor = 0.5 * ( 1 - 2*delta );
    double numerator = (1+delta)*(i+abs(s)-1)*(i+abs(s));
    double denominator = (abs(t)==i ? 2*i*(2*i-1) : (i+t)*(i-t));
    return factor * sqrt( numerator / denominator );
}
```

Figure B.3. Function definition for SHRotationMatrix::v_i_st().

```
// Computes the  $w_{s,t}^i$  coefficient, as per Table B.1
double SHRotationMatrix::w_i_st( int i, int s, int t )
{
    int delta = ( s==0 ? 1 : 0 );
    double factor = -0.5 * ( 1 - delta );
    double numerator = (i-abs(s)-1)*(i-abs(s));
    double denominator = (abs(t)==i ? 2*i*(2*i-1) : (i+t)*(i-t));
    return factor * sqrt( numerator / denominator );
}
```

Figure B.4. Function definition for SHRotationMatrix::w_i_st().

```
// Computes the  $U_{s,t}^i$  function, as per Table B.2
double SHRotationMatrix::U_i_st( int i, int s, int t )
{
    return P_r_i_st(0,i,s,t);
}
```

Figure B.5. Function definition for SHRotationMatrix::U_i_st().

```

// Computes the  $V_{s,t}^i$  function, as per Table B.2
double SHRotationMatrix::V_i_st( int i, int s, int t )
{
    int delta = ( abs(s)==1 ? 1 : 0 );
    if ( s == 0 )
        return P_r_i_st(1,i,1,t) + P_r_i_st(-1,i,-1,t);
    if ( s > 0 )
        return
            sqrt(1+delta)*P_r_i_st(1,i,s-1,t) - (1-delta)*P_r_i_st(-1,i,-s+1,t);
    return
        (1-delta)*P_r_i_st(1,i,s+1,t) + sqrt(1+delta)*P_r_i_st(-1,i,-s-1,t);
}

```

Figure B.6. Function definition for SHRotationMatrix::V_i_st().

```

// Computes the  $W_{s,t}^i$  function, as per Table B.2
double SHRotationMatrix::W_i_st( int i, int s, int t )
{
    if ( s==0 ) return 0;
    if ( s > 0 ) return P_r_i_st(1,i,s+1,t) + P_r_i_st(-1,i,-s-1,t);
    return P_r_i_st(1,i,s-1,t) - P_r_i_st(-1,i,-s+1,t);
}

```

Figure B.7. Function definition for SHRotationMatrix::W_i_st().

```

// Computes the  ${}_rP_{s,t}^i$  function, as per Table B.3
double SHRotationMatrix::P_r_i_st( int r, int i, int s, int t )
{
    if ( abs(t) < i ) return R(r,0)*M(i-1,s,t);
    if ( t == i ) return R(r,1)*M(i-1,s,i-1) - R(r,-1)*M(i-1,s,-i+1);
    return R(r,1)*M(i-1,s,-i+1) + R(r,-1)*M(i-1,s,i-1);
}

```

Figure B.8. Function definition for SHRotationMatrix::P_r_i_st().

```

//  $R_{i,j}$  indexes into the input matrix for  $-1 \leq i, j \leq 1$ 
// as per the definition of  $[R_{s,t}]$  (Eq. B.40)
double SHRotationMatrix::R( int i, int j )
{
    int jp = ((j+2) % 3); //  $0 \leq jp < 3$ 
    int ip = ((i+2) % 3); //  $0 \leq ip < 3$ 
    return inMatrix[jp*3+ip]; // index into input matrix
}

```

Figure B.9. Function definition for SHRotationMatrix::R().

```

// Returns an element of the output matrix.
//   l is the band of the matrix to reference  $0 \leq l < order$ 
//   a and b are elements in the band, in the range [-1..1]
double SHRotationMatrix::M( int l, int a, int b )
{
    if (l<=0) return outMatrix[0];

    // Find the center of band l (outMatrix[ctr,ctr])
    int ctr = l*(l+1);
    return outMatrix[ matIndex( ctr + b, ctr + a ) ];
}

```

Figure B.10. Function definition for SHRotationMatrix::M().

```

// Find the index in the  $order^2 \times order^2$  output matrix
//   for a given column and row
int SHRotationMatrix::matIndex( int col, int row )
{
    return col*order*order+row;
}

```

Figure B.11. Function definition for SHRotationMatrix::matIndex().

```

// Setup the rotation matrix of a specified order given the equivalent
//    $3 \times 3$  rotation transformation.
SHRotationMatrix::SHRotationMatrix( int order, double matrix[9] ):
    order(order)
{
    // Copy the input matrix into local storage.
    for (int i=0;i<9;i++)
        inMatrix[i] = matrix[i];

    // allocate memory for SH rotation matrix.
    outMatrix = new double[order*order*order*order];

    // actually compute the matrix.
    computeMatrix();
}

```

Figure B.12. Definition of constructor SHRotationMatrix::SHRotationMatrix().

```

// Assuming we know the input matrix, compute the SH rotation matrix
void SHRotationMatrix::computeMatrix( void )
{
    // initialize the matrix to 0's
    for (int i=0;i<order*order;i++)
        for (int j=0;j<order*order;j++)
            outMatrix[matIndex(i,j)] = 0;

    // 0th band (1x1 matrix) is the identity
    outMatrix[0] = 1;
    if (order < 2) return;

    // 1st band is a permutation of the 3D rotation matrix
    for (int count=0, i=-1; i<=1; i++)
        for (int j=-1; j<=1; j++)
            outMatrix[ matIndex( (i+3)%3+1, (j+3)%3+1 ) ] = inMatrix[count++];

    // 2nd+ bands use a recurrence relation.
    for (int l=2;l<order;l++)
    {
        int ctr = l*(l+1);
        for (int s=-1;s<=1;s++)
            for (int t=-1;t<=1;t++)
                outMatrix[ matIndex( ctr + t, ctr + s ) ] =
                    u_i_st( l, s, t ) * U_i_st( l, s, t ) +
                    v_i_st( l, s, t ) * V_i_st( l, s, t ) +
                    w_i_st( l, s, t ) * W_i_st( l, s, t );
    }
}

```

Figure B.13. Function definition for SHRotationMatrix::computeMatrix().


```

// Applies the computed spherical harmonic rotation matrix
//   in, out should contain order*order elements each.
//   This does not do a full multiplication, rather only
//   the (potentially) non-zero elements are multiplied.
void SHRotationMatrix::applyMatrix( double *in, double *out )
{
    // first band (order 0) is a 1x1 identity rotation matrix
    out[0] = in[0];

    // set up data for multiplying 2nd band (order 1) coefs
    int ord=1;
    int minIdx=1;
    int maxIdx=4;

    // multiply the rest of the matrix
    for (int idx=1; idx<order*order; idx++)
    {
        // multiply coefs from current band
        out[idx]=0;
        for (int j=minIdx;j<maxIdx;j++)
            out[idx] += outMatrix[ matIndex( j, idx ) ] * in[j];

        // increase the band, reset indices.
        if (idx>=maxIdx-1)
        {
            ord++;
            minIdx=maxIdx;
            maxIdx+=2*ord+1;
        }
    }
}

```

Figure B.14. Function definition for SHRotationMatrix::applyMatrix().

REFERENCES

- [1] Maneesh Agrawala, Ravi Ramamoorthi, Alan Heirich, and Laurent Moll. Efficient image-based methods for rendering soft shadows. In *Proceedings of SIGGRAPH*, pages 375–384, 2000.
- [2] Tomas Akenine-Möller and Ulf Assarsson. Approximate soft shadows on arbitrary surfaces using penumbra wedges. In *Proceedings of the Eurographics Rendering Workshop*, pages 309–318, 2002.
- [3] Tomas Akenine-Möller and Eric Haines. *Real-time Rendering*. AK Peters, Massachusetts, second edition, 2002.
- [4] Arthur Appel. The notion of quantitative invisibility and machine rendering of solids. In *Proceedings of the ACM National Conference*, pages 387–393, 1967.
- [5] George B. Arfken and Hans J. Weber. *Mathematical Methods for Physicists*. Academic Press, 4th edition edition, 1995.
- [6] James Arvo. Backward ray tracing. *Developments in Ray Tracing*, pages 259–263, 1986. ACM Siggraph '86 Course Notes.
- [7] James Arvo and David Kirk. Particle transport and image synthesis. In *Proceedings of SIGGRAPH*, pages 63–66, 1990.
- [8] Ian Ashdown. *Radiosity: A Programmer's Perspective*. John Wiley & Sons, Inc., 1995.
- [9] Ulf Assarsson and Tomas Akenine-Möller. A geometry-based soft shadow volume algorithm using graphics hardware. *ACM Transactions on Graphics*, 22(3):511–520, July 2003.
- [10] Kavita Bala, Julie Dorsey, and Seth Teller. Radiance interpolants for accelerated bounded-error ray tracing. *ACM Transactions on Graphics*, 18(3):100–130, August 1999.
- [11] James F. Blinn. Models of light reflection for computer synthesized pictures. In *Proceedings of SIGGRAPH*, pages 192–198, 1977.
- [12] Stefan Brabec and Hans-Peter Seidel. Single sample soft shadows using depth maps. In *Proceedings of Graphics Interface*, pages 219–228, 2002.
- [13] Willian E. Byerly. *An Elementary Treatise on Fourier's Series and Spherical, Cylindrical, and Ellipsoidal Harmonics, with Applications to Problems in Mathematical Physics*. Ginn and Company, 1893.

- [14] Brian Cabral, Nelson Max, and Rebecca Springmeyer. Bidirectional reflection functions from surface bump maps. In *Proceedings of SIGGRAPH*, pages 273–281, 1987.
- [15] Brian Cabral, Marc Olano, and Philip Nemeec. Reflection space image based rendering. In *Proceedings of SIGGRAPH*, pages 165–170, 1999.
- [16] Eric Chan and Fredo Durand. Rendering fake soft shadows with smoothies. In *Proceedings of the Eurographics Symposium on Rendering*, pages 208–218, 2003.
- [17] Subrahmanyan Chandrasekhar. *Radiative Transfer*. Oxford University Press, 1950.
- [18] Min Chen and James Arvo. Theory and application of specular path perturbation. *ACM Transactions on Graphics*, 19(4):246–278, October 2000.
- [19] Shenchang Eric Chen. Incremental radiosity: An extension of progressive radiosity to an interactive image synthesis system. In *Proceedings of SIGGRAPH*, pages 135–144, 1990.
- [20] Shenchang Eric Chen, Holly Rushmeier, Gavin Miller, and Douglass Turner. A progressive multi-pass method for global illumination. In *Proceedings of SIGGRAPH*, pages 165–174, 1991.
- [21] Michael Cohen, Shenchang Eric Chen, John Wallace, and Donald Greenburg. A progressive refinement approach to fast radiosity image generation. In *Proceedings of SIGGRAPH*, pages 75–84, 1988.
- [22] Michael Cohen and Donald Greenburg. The hemi-cube: A radiosity solution for complex environments. In *Proceedings of SIGGRAPH*, pages 31–40, 1985.
- [23] Robert Cook, Thomas Porter, and Loren Carpenter. Distributed ray tracing. In *Proceedings of SIGGRAPH*, pages 137–145, 1984.
- [24] Robert L. Cook and Kenneth E. Torrance. A reflectance model for computer graphics. In *Proceedings of SIGGRAPH*, pages 307–316, 1981.
- [25] Franklin Crow. Shadow algorithms for computer graphics. In *Proceedings of SIGGRAPH*, pages 242–248, 1977.
- [26] Paul E. Debevec and Jitendra Malik. Recovering high dynamic range radiance maps from photographs. In *Proceedings of SIGGRAPH*, pages 369–378, 1997.
- [27] David E Demarle, Steven Parker, Mark Hartner, Christiaan Gribble, and Charles Hansen. Distributed interactive ray tracing for large volume visualization. In *Proceedings of the IEEE Symposium on Parallel and Large-Data Visualization and Graphics*, pages 87–94, 2003.
- [28] Paul Diefenbach and Norman Badler. Multi-pass pipeline rendering: Realism for dynamic environments. In *Proceedings of the Symposium on Interactive 3D Graphics*, pages 59–70, 1997.
- [29] George Drettakis and Eugene Fiume. A fast shadow algorithm for area light sources

- using backprojection. In *Proceedings of SIGGRAPH*, pages 223–230, 1994.
- [30] George Drettakis and François X. Sillion. Interactive update of global illumination using a line-space hierarchy. In *Proceedings of SIGGRAPH*, pages 57–64, 1997.
- [31] Philip Dutre and Yves Willems. Importance-driven monte carlo light tracing. In *Proceedings of the Eurographics Rendering Workshop*, pages 188–197, 1994.
- [32] Philip Dutre and Yves Willems. Potential-driven monte carlo particle tracing for diffuse environments with adaptive probability functions. In *Proceedings of the Eurographics Rendering Workshop*, pages 306–315, 1995.
- [33] A. R. Edmonds. *Angular Momentum in Quantum Mechanics*. Princeton University Press, 1957.
- [34] Cass Everitt, Ashu Rege, and Cem Cabenoya. Hardware shadow mapping. Technical report, nVidia, http://developer.nvidia.com/object/hwshadowmap_paper.html, 2001.
- [35] Randima Fernando, Sebastian Fernandez, Kavita Bala, and Donald Greenberg. Adaptive shadow maps. In *Proceedings of SIGGRAPH*, pages 387–390, 2001.
- [36] David Forsyth, Chien Yang, and Kim Teo. Efficient radiosity in dynamic environments. In *Proceedings of the Eurographics Rendering Workshop*, pages 313–323, 1994.
- [37] David George, Francois Sillion, and Donald Greenberg. Radiosity redistribution for dynamic environments. *IEEE Computer Graphics & Applications*, 10(4):26–34, July 1990.
- [38] Cindy Goral, Kenneth Torrance, Donald Greenberg, and Bennett Battaile. Modelling the interaction of light between diffuse surfaces. In *Proceedings of SIGGRAPH*, pages 213–222, 1984.
- [39] Steven Gortler, Peter Schroder, Michael Cohen, and Pat Hanrahan. Wavelet radiosity. In *Proceedings of SIGGRAPH*, pages 221–230, 1993.
- [40] Henri Gouraud. Continuous shading of curved surfaces. *IEEE Transactions on Computers*, 20(6):623, June 1971.
- [41] Xavier Granier and George Drettakis. Incremental updates for rapid glossy global illumination. *Computer Graphics Forum*, 20(3):268–277, 2001.
- [42] Xavier Granier, George Drettakis, and Bruce Walter. Fast global illumination including specular effects. In *Proceedings of the Eurographics Rendering Workshop*, pages 47–59, 2000.
- [43] Robin Green. Spherical harmonic lighting: The gritty details. In *Archives of the Game Developers Conference*, March 2003.
- [44] Gene Greger, Peter Shirley, Philip Hubbard, and Donald Greenberg. The irradiance volume. *IEEE Computer Graphics & Applications*, 18(2):32–43, March–April 1998.

- [45] Eric Haines. Soft planar shadows using plateaus. *Journal of Graphics Tools*, 6(1):19–27, 2001.
- [46] Pat Hanrahan, David Salzman, and Larry Aupperle. A rapid hierarchical radiosity algorithm. In *Proceedings of SIGGRAPH*, pages 197–206, 1991.
- [47] David Hart, Philip Dutre, and Donald Greenberg. Direct illumination with lazy visibility evaluation. In *Proceedings of SIGGRAPH*, pages 147–154, 1999.
- [48] Paul Heckbert and Michael Herf. Simulating soft shadows with graphics hardware. Technical Report CMU-CS-97-104, Carnegie Mellon University, January 1997.
- [49] Paul S. Heckbert. Adaptive radiosity textures for bidirectional ray tracing. In *Proceedings of SIGGRAPH*, pages 145–154, 1990.
- [50] Paul S. Heckbert. Discontinuity meshing for radiosity. In *Proceedings of the Eurographics Rendering Workshop*, pages 203–216, 1992.
- [51] Paul S. Heckbert. *Simulating Global Illumination Using Adaptive Meshing*. PhD thesis, UC Berkeley, California, June 1999.
- [52] Paul S. Heckbert and Pat Hanrahan. Beam tracing polygonal objects. In *Proceedings of SIGGRAPH*, pages 119–127, 1984.
- [53] Tim Heidmann. Real shadows, real time. *Iris Universe*, (18):23–31, November 1991.
- [54] Wolfgang Heidrich, Stefan Brabec, and Hans-Peter Seidel. Soft shadow maps for linear lights. In *Proceedings of the Eurographics Rendering Workshop*, pages 269–280, 2000.
- [55] Wolfgang Heidrich, Jan Kautz, Philipp Slusallek, and Hans-Peter Seidel. Canned lightsources. In *Proceedings of the Eurographics Rendering Workshop*, pages 293–300, 1998.
- [56] Helen Hu, Amy Gooch, William Thompson, Brian Smits, J. Rieser, and Peter Shirley. Visual cues for imminent object contact in realistic virtual environments. In *Proceedings of Visualization*, pages 127–136, 2000.
- [57] David Immel, Michael Cohen, and Donald Greenberg. A radiosity method for non-diffuse environments. In *Proceedings of SIGGRAPH*, pages 133–142, 1986.
- [58] Joseph Ivanic and Klaus Ruedenberg. Rotation matrices for real spherical harmonics, direct determination by recursion. *Journal of Physical Chemistry A*, 100(15):6342–6347, 1996.
- [59] Joseph Ivanic and Klaus Ruedenberg. Additions and corrections: Rotation matrices for real spherical harmonics. *Journal of Physical Chemistry A*, 102(45):9099–9100, 1998.
- [60] Kei Iwasaki, Yoshinori Dobashi, and Tomoyuki Nishita. A fast rendering method for refractive and reflective caustics due to water surfaces. *Computer Graphics*

Forum, 22, 2003.

- [61] Henrik Wann Jensen. Importance driven path tracing using the photon map. In *Proceedings of the Eurographics Rendering Workshop*, pages 326–335, 1995.
- [62] Henrik Wann Jensen. Rendering caustics on non-lambertian surfaces. In *Proceedings of Graphics Interface*, pages 116–121, 1996.
- [63] Henrik Wann Jensen and Niels Jørgen Christensen. Efficiently rendering shadows using the photon map. In *Proceedings of Compugraphics*, December 1995.
- [64] Henrik Wann Jensen and Niels Jørgen Christensen. Photon maps in bidirectional monte carlo ray tracing of complex objects. *Computers & Graphics*, 19(2):215–224, March 1995.
- [65] Henrik Wann Jensen and Per H. Christensen. Efficient simulation of light transport in scenes with participating media using photon maps. In *Proceedings of SIGGRAPH*, pages 311–320, 1998.
- [66] Henrik Wann Jensen, Stephen R. Marschner, Marc Levoy, and Pat Hanrahan. A practical model for subsurface light transport. In *Proceedings of SIGGRAPH*, pages 511–518, 2001.
- [67] James Kajiya. The rendering equation. In *Proceedings of SIGGRAPH*, pages 143–150, 1986.
- [68] James Kajiya and Brian Von Herzen. Ray tracing volume densities. In *Proceedings of SIGGRAPH*, pages 165–174, 1984.
- [69] Arie E. Kaufman. Volume visualization in medicine. In *Handbook of Medical Imaging*, pages 713–730. Academic Press, 2000.
- [70] Alexander Keller. Instant radiosity. In *Proceedings of SIGGRAPH*, pages 49–54, 1997.
- [71] Daniel Kersten, David C. Knill, Pascal Mamassian, and Isabelle Bulthoff. Illusory motion from shadows. *Nature*, 279(6560):31, 1996.
- [72] Daniel Kersten, Pascal Mamassian, and David C. Knill. Moving cast shadows induce apparent motion in depth. *Perception*, 26(2):171–192, 1997.
- [73] Joe Kniss, Simon Premoze, Charles Hansen, Peter Shirley, and Allan McPherson. A model for volume lighting and modeling. *IEEE Transactions on Visualization and Computer Graphics*, 9(2):150–162, April 2003.
- [74] Eric Lafortune and Yves Willems. Bi-directional path tracing. In *Proceedings of Compugraphics*, pages 145–153, 1993.
- [75] Michael S. Langer and Heinrich H. Bühlhoff. Depth discrimination from shading under diffuse lighting. *Perception*, 29:649–660, 2000.
- [76] Barthold Lichtenbelt, Randy Crane, and Shaz Naqvi. *Introduction to Volume*

Rendering. Prentice Hall, 1st edition, 1998.

- [77] Dani Lischinski, Filippo Tampieri, and Donald Greenberg. Discontinuity meshing for accurate radiosity. *IEEE Computer Graphics & Applications*, 12(6):25–39, November 1992.
- [78] Dani Lischinski, Filippo Tampieri, and Donald Greenberg. Combining hierarchical radiosity and discontinuity meshing. In *Proceedings of SIGGRAPH*, pages 199–208, 1993.
- [79] William E. Lorensen and Harvey E. Cline. Marching cubes: A high resolution 3d surface construction algorithm. In *Proceedings of SIGGRAPH*, pages 163–169, 1987.
- [80] Philippe Loutrel. A solution to the hidden-line problem for computer-drawn polyhedra. *IEEE Transactions on Computers*, C-19(3):205–213, March 1970.
- [81] Cindee Madison, Daniel Kersten, William Thompson, Peter Shirley, and Brian Smits. The use of subtle illumination cues for human judgement of spatial layout. Technical Report Technical Report UUCS-99-001, University of Utah, January 1999.
- [82] Thomas Malley. A shading method for computer generated images. Master’s thesis, Computer Science Department, University of Utah, June 1988.
- [83] Stephen R. Marschner and Richard J. Lobb. An evaluation of reconstruction filter for volume rendering. In *Proceedings of Visualization*, pages 100–107, October 1994.
- [84] Nelson Max. Optical models for direct volume rendering. *IEEE Transactions on Visualization and Computer Graphics*, 1(2):99–108, 1995.
- [85] Gregory M. Maxwell, Michael J. Bailey, and Victor W. Goldschmidt. Calculations of the radiation configuration factor using ray casting. *Computer-Aided Design*, 18(7):371–379, September 1986.
- [86] Michael McCool. Shadow volume reconstruction from depth maps. *ACM Transactions on Graphics*, 19(1):1–26, January 2000.
- [87] Gavin Miller. Efficient algorithms for local and global accessibility shading. In *Proceedings of SIGGRAPH*, pages 319–326, 1994.
- [88] Don Mitchell and Pat Hanrahan. Illumination from curved reflectors. In *Proceedings of SIGGRAPH*, pages 283–291, 1992.
- [89] National Bureau of Standards. Monte carlo method. In A. S. Housholder, editor, *Applied Mathematics Series 12*, 1951.
- [90] Ren Ng, Ravi Ramamoorthi, and Pat Hanrahan. All-frequency shadows using non-linear wavelet lighting approximation. *ACM Transactions on Graphics*, 22(3):376–381, 2003.
- [91] Fred E. Nicodemus, Joseph C. Richmond, Jack J. Hsia, Irving W. Ginsberg, and

- Thomas Limperis. *Geometrical considerations and nomenclature for reflectance*. Monograph 160. National Bureau of Standards, October 1977.
- [92] Tomoyuki Nishita and Eihachiro Nakamae. Method of displaying optical effects within water using accumulation buffer. In *Proceedings of SIGGRAPH*, pages 373–381, 1994.
- [93] J. F. Nye. *Natural Focusing and Fine Structure of Light*. Institute of Physics Publishing, Bristol, 1999.
- [94] Eyal Ofek and Ari Rappoport. Interactive reflections on curved objects. In *Proceedings of SIGGRAPH*, pages 333–342, 1999.
- [95] Marc Ouellette and Eugene Fiume. Approximating the location of integrand discontinuities for penumbral illumination with linear light sources. In *Proceedings of the Eurographics Rendering Workshop*, pages 213–224, 1999.
- [96] Steven Parker, William Martin, Peter-Pike Sloan, Peter Shirley, Brian Smits, and Charles Hansen. Interactive ray tracing. In *Proceedings of the ACM Symposium on Interactive 3D Graphics*, pages 119–126, 1999.
- [97] Steven Parker, Michael Parker, Yarden Livnat, Peter-Pike Sloan, Charles Hansen, and Peter Shirley. Interactive ray tracing for volume visualization. *IEEE Transactions on Visualization and Computer Graphics*, 5(3):287–296, July 1999.
- [98] Steven Parker, Peter Shirley, Yarden Livnat, Charles Hansen, and Peter-Pike Sloan. Interactive ray tracing for isosurface rendering. In *Proceedings of Visualization*, pages 233–238, October 1998.
- [99] Steven Parker, Peter Shirley, and Brian Smits. Single sample soft shadows. Technical Report Technical Report UUCS-98-019, University of Utah, October 1998.
- [100] C. Alejandro Parraga, Tom Troscianko, and David J. Tolhurst. The human visual system is optimised for processing the spatial information in natural visual images. *Current Biology*, 10(1):35–38, January 2000.
- [101] Sumanta Pattanaik and Sudhir Mudur. Adjoint equations and random walks for illumination computation. *ACM Transactions on Graphics*, 14(1):77–102, January 1995.
- [102] Bui-Thong Phong. Illumination for computer generated images. *Communications of the ACM*, 18:311–317, 1975.
- [103] John F. Pile. *Color in interior design*. McGraw-Hill, New York, 1997.
- [104] John F. Pile. *Interior design*. Harry N. Abrams, Inc., New York, 3rd. edition, 2003.
- [105] Timothy Purcell, Craig Donner, Mike Cammarano, Henrik Wann Jensen, and Pat Hanrahan. Photon mapping on programmable graphics hardware. In *Proceedings of the SIGGRAPH/Eurographics Conference on Graphics Hardware*, pages 41–50, 2003.

- [106] Ravi Ramamoorthi and Pat Hanrahan. An efficient representation for irradiance environment maps. In *Proceedings of SIGGRAPH*, pages 497–500, 2001.
- [107] Ravi Ramamoorthi and Pat Hanrahan. A signal-processing framework for inverse rendering. In *Proceedings of SIGGRAPH*, pages 117–128, 2001.
- [108] Ravi Ramamoorthi and Pat Hanrahan. Frequency space environment map rendering. In *Proceedings of SIGGRAPH*, pages 517–526, 2002.
- [109] William Reeves, David Salesin, and Robert Cook. Rendering antialiased shadows with depth maps. In *Proceedings of SIGGRAPH*, pages 283–291, 1987.
- [110] Erik Reinhard, Peter Shirley, and Tom Troscianko. Natural image statistics for computer graphics. Technical Report UUCS-01-002, University of Utah, March 2001.
- [111] Holly Rushmeier, Charles Patterson, and Aravindan Veerasamy. Geometric simplification for indirect illumination calculations. In *Proceedings of Graphics Interface*, pages 227–236, 1993.
- [112] Will Schroeder, Ken Martin, and William Lorensen. *The Visualization Toolkit: An Object-Oriented Approach to 3D Graphics*. Prentice Hall, 3rd edition, 2003.
- [113] Mark Segal, Carl Korobkin, Rolf van Widenfelt, Jim Foran, and Paul Haeberli. Fast shadows and lighting effects using texture mapping. In *Proceedings of SIGGRAPH*, pages 249–252, 1992.
- [114] Peter Shirley. A ray tracing method for illumination calculation in diffuse-specular scenes. In *Proceedings of Graphics Interface*, pages 205–212, 1990.
- [115] Peter Shirley. *Fundamentals of Computer Graphics*. AK Peters, 2002.
- [116] Silicon Graphics, Inc. OpenGL ARB Extension Registry. <http://oss.sgi.com/projects/ogl-sample/registry/>.
- [117] Francois Sillion, James Arvo, Stephen Westin, and Donald Greenberg. A global illumination solution for general reflectance distributions. In *Proceedings of SIGGRAPH*, pages 187–196, 1991.
- [118] Francois Sillion and Claude Puech. A general two-pass method integrating specular and diffuse reflection. In *Proceedings of SIGGRAPH*, pages 335–344, 1989.
- [119] Peter-Pike Sloan, Jesse Hall, John Hart, and John Snyder. Clustered principal components for precomputed radiance transfer. *ACM Transactions on Graphics*, 22(3):382–391, 2003.
- [120] Peter-Pike Sloan, Jan Kautz, and John Snyder. Precomputed radiance transfer for real-time rendering in dynamic, low-frequency lighting environments. *ACM Transactions on Graphics*, 21(3):527–536, 2002.
- [121] Peter-Pike Sloan, Xingou Liu, Heung-Yeung Shum, and John Snyder. Bi-scale radiance transfer. *ACM Transactions on Graphics*, 22(3):370–375, 2003.

- [122] Brian Smits, James Arvo, and Donald Greenberg. A clustering algorithm for radiosity in complex environments. In *Proceedings of SIGGRAPH*, pages 435–442, 1994.
- [123] Brian Smits, James Arvo, and David Salesin. An importance-driven radiosity algorithm. In *Proceedings of SIGGRAPH*, pages 273–282, 1992.
- [124] Lisa M. Sobierajski and Arie E. Kaufman. Volumetric ray tracing. In *Proceedings of the Symposium on Volume Visualization*, pages 11–18. ACM Press, 1994.
- [125] Cyril Soler and Francois Sillion. Automatic calculation of soft shadow textures for fast, high quality radiosity. In *Proceedings of the Eurographics Rendering Workshop*, pages 199–210, 1998.
- [126] Cyril Soler and Francois Sillion. Fast calculation of soft shadow texture using convolution. In *Proceedings of SIGGRAPH*, pages 321–332, 1998.
- [127] Jos Stam. Random caustics: Natural textures and wave theory revisited. In *SIGGRAPH Visual Proceedings*, page 150. ACM Press, 1996.
- [128] Jos Stam. Aperiodic texture mapping. Technical Report Research Report R046, ERCIM, January 1997.
- [129] Marc Stamminger and George Drettakis. Perspective shadow maps. In *Proceedings of SIGGRAPH*, pages 557–562, 2002.
- [130] Michael Stark and Richard Riesenfeld. Exact illumination in polygonal environments using vertex tracing. In *Proceedings of the Eurographics Rendering Workshop*, pages 149–160, 2000.
- [131] A. James Stewart. Vicinity shading for enhanced perception of volumetric data. In *Proceedings of Visualization*, pages 355–362, 2003.
- [132] A. James Stewart and Sherif Ghali. Fast computation of shadow boundaries using spatial coherence and backprojection. In *Proceedings of SIGGRAPH*, pages 231–238, 1994.
- [133] Parag Tole, Fabio Pellacini, Bruce Walter, and Donald Greenberg. Interactive global illumination in dynamic scenes. In *Proceedings of SIGGRAPH*, pages 537–546, 2002.
- [134] Roy Troutman and Nelson L. Max. Radiosity algorithms using higher order finite element methods. In *Proceedings of SIGGRAPH*, pages 209–212, 1993.
- [135] Tushar Udeshi and Charles Hansen. Towards interactive, photorealistic rendering of indoor scenes: A hybrid approach. In *Proceedings of the Eurographics Rendering Workshop*, pages 63–76, 1999.
- [136] Eric Veach and Leonidas J Guibas. Metropolis light transport. In *Proceedings of SIGGRAPH*, pages 65–76, 1997.
- [137] Ingo Wald, Carsten Benthin, and Philipp Slusallek. Interactive global illumination

- in complex highly occluded environments. In *Proceedings of the Eurographics Symposium on Rendering*, pages 74–81, 2003.
- [138] Ingo Wald, Thomas Kollig, Carsten Benthin, Alexander Keller, and Philipp Slusallek. Interactive global illumination using fast ray tracing. In *Proceedings of the Eurographics Rendering Workshop*, pages 15–24, 2002.
- [139] Ingo Wald, Philipp Slusallek, Carsten Benthin, and Markus Wagner. Interactive rendering with coherent ray tracing. *Computer Graphics Forum*, 20(3):153–164, 2001.
- [140] John Wallace, Michael Cohen, and Donald Greenberg. A two-pass solution to the rendering equation: A synthesis of ray tracing and radiosity methods. In *Proceedings of SIGGRAPH*, pages 311–320, 1987.
- [141] John Wallace, Kells Elmquist, and Eric Haines. A ray tracing algorithm for progressive radiosity. In *Proceedings of SIGGRAPH*, pages 335–344, 1989.
- [142] Bruce Walter, George Drettakis, and Steven Parker. Interactive rendering using the render cache. In *Proceedings of the Eurographics Rendering Workshop*, pages 19–30, June 1999.
- [143] Michael Wand and Wolfgang Straßer. Real-time caustics. *Computer Graphics Forum*, 22(3):611–620, 2003.
- [144] Leonard Wanger. The effect of shadow quality on the perception of spatial relationships in computer generated imagery. In *Proceedings of the Symposium on Interactive 3D Graphics*, pages 39–42, 1992.
- [145] Leonard Wanger, James Ferwerda, and Donald Greenberg. Perceiving spatial relationships in computer-generated images. *IEEE Computer Graphics & Applications*, 12(3):44–58, May 1992.
- [146] Gregory J. Ward, Francis M. Rubinstein, and Robert D. Clear. A ray tracing solution for diffuse interreflection. In *Proceedings of SIGGRAPH*, pages 85–92, 1988.
- [147] Mark Watt. Light-water interaction using backward beam tracing. In *Proceedings of SIGGRAPH*, pages 377–385, 1990.
- [148] Eric W. Weisstein. *CRC Concise Encyclopedia of Mathematics*. CRC Press, 1999.
- [149] Turner Whitted. An improved illumination model for shaded display. *Communications of the ACM*, 23(6):343–349, June 1980.
- [150] Lance Williams. Casting curved shadows on curved surfaces. In *Proceedings of SIGGRAPH*, pages 270–274, 1978.
- [151] Andrew Woo, Pierre Poulin, and Alain Fournier. A survey of shadow algorithms. *IEEE Computer Graphics & Applications*, 10(6):13–32, November 1990.
- [152] Chris Wyman and Charles Hansen. Penumbra maps: Approximate soft shadows

- in real-time. In *Proceedings of the Eurographics Symposium on Rendering*, pages 202–207, 2003.
- [153] Chris Wyman, Charles Hansen, and Peter Shirley. Interactive raytraced caustics. Technical Report Technical Report UUCS-03-009, University of Utah, April 2003.
- [154] Harold R. Zatz. Galerkin radiosity: A higher order solution method for global illumination. In *Proceedings of SIGGRAPH*, pages 213–220, August 1993.
- [155] Sergej Zhukov, Andrej Iones, and Grigorij Kronin. An ambient light illumination model. In *Proceedings of the Eurographics Rendering Workshop*, pages 45–56, 1998.